**Title**
TWO-NUCLEON TRANSFER REACTIONS INDUCED BY POLARIZED PROTONS



**Author**
Macdonald, John Alan.

**Publication Date**
1973-10-01

LBL-2320

# TWO-NUCLEON TRANSFER REACTIONS INDUCED BY POLARIZED PROTONS

John Alan Macdonald
(Ph. D. Thesis)

October 1973

Prepared for the U. S. Atomic Energy Commission
under Contract W-7405-ENG-48



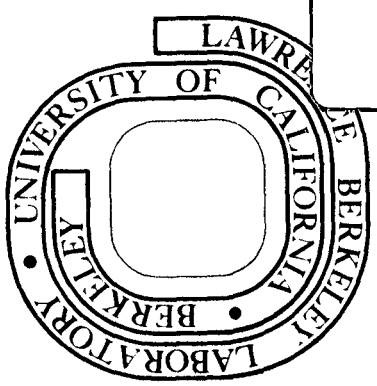


LBL-2320

## DISCLAIMER

TWO-NUCLEON TRANSFER REACTIONS INDUCED BY POLARIZED PROTONS

Contents

# TWO-NUCLEON TRANSFER REACTIONS INDUCED BY POLARIZED PROTONS

John Alan Macdonald

Department of Chemistry and
Lawrence Berkeley Laboratory
University of California
Berkeley, California 94720

October 1973

## ABSTRACT

$(\vec{p},t)$ and $(\vec{p}, {}^3He)$ reactions have been induced by polarized protons of 43.8 MeV on $^{16}O$, $^{15}N$, $^{9}Be$, and $^{7}Li$, and of 49.6 MeV on $^{13}C$ targets. The $^{208}Pb(\vec{p},t)$ transitions at $E_{\vec{p}}$ = 40 MeV to four final states in $^{206}Pb$ have also been observed. Relative differential cross sections and analyzing powers have been measured for over fifty transitions, of which thirty-six have been compared with zero-range DWBA calculations with a spin-orbit potential in the proton channel, and employing wave functions of Cohen and Kurath and of True and Ford. Although generally good results for the differential cross section predictions were obtained, attempts to fit the analyzing powers met with mixed results. In general $(\vec{p},t)$ results were fit better than $(\vec{p}, {}^3He)$, ground state transitions better than those to excited states, and transitions to analog states better than more complex transitions. These conclusions were not altered by including the effects of spin dependence in the two-body interaction or of spin-orbit coupling in the exit channel. It seems doubtful that the discrepancies can be overcome entirely by finite range calculations, though they should be tried, as should attempts to evaluate the importance of second order effects.

# I. INTRODUCTION

In the decade or so during which direct two-nucleon pickup reactions have been extensively studied, the (p,t) and (p, $^3$He) reactions in particular have become well established as valuable spectroscopic tools (e.g., Cer 64a, Fle 68a, Fle 68b, Cer 66). Theoretical interpretation of experimental cross sections utilizing the distorted wave Born approximation (DWBA) and incorporating shell-model wave functions (Gle 63, Gle 65, Tow 69) has led to the characterization of many nuclear energy levels.

In spite of the extensive success enjoyed by the zero-range DWBA in describing many (p,t) and (p, $^3$He) differential cross sections at forward angles ($\theta \leqslant 60°$) (e.g., Fle 71, Smi 70), some evidence exists of inadequacies in this simple theoretical approach. For example, previous reports (Fle 68a) describe several major inconsistencies in comparing the ratio of (p,t) to (p, $^3$He) cross sections to certain mirror states with limits imposed by the theory, as well as the observation of a strong angular momentum forbidden transition in the 1p-shell. In view of these problems, it is of interest to make further comparisons with the simple theory by measuring analyzing powers (defined on page 30), which are observed via the left/right asymmetry in the differential cross sections for these reactions initiated by polarized protons.

Measurements of polarization phenomena in nuclear reactions have yielded a number of important results in the past. Early experiments were restricted in versatility and precision because of the necessity of using a double scattering technique. In this method, a partially

polarized beam was obtained by scattering an unpolarized beam on a primary target; the secondary scattered beam was collimated and then allowed to impinge on a second target containing the nuclei of interest. The problems of very low intensity and poor energy resolution were immense and limited these investigations to high cross section processes, such as elastic scattering. Nevertheless, data obtained in this way, together with cross section measurements, lead, for example, to improved descriptions of nucleon-nucleus scattering including spin-orbit effects in the optical model (e.g., Fri 67). Barschall (Bar 67) and Rosen (Ros 67) have given good introductory descriptions of this experimental technique, and some of the results.

The bulk of presently available high precision polarization information has been obtained using accelerator facilities equipped with polarizing ion sources. With such apparatus it has been possible to extend the scope of study to lower cross section reactions such as single nucleon stripping $(\vec{d},p)$, in which spectroscopic information can be derived from the strong J-dependence of the analyzing power. Haeberli (Hae 71) and Glashausser (Gla 74) have summarized this and other work.

The investigation of two-nucleon transfer reactions with polarized protons has been restricted by the large negative Q-values often encountered which put them beyond the reach of a significant fraction of accelerators equipped to do such studies. However, a number of sources of protons of adequate energy are available and some results for $(\vec{p},t)$ on $^{12}C$, $^{16}O$, $^{28}Si$, and $^{176}Yb$, and for $^{16}O(\vec{p}, {}^{3}He)$ have been reported by others (Nel 70a, Nel 70b, Igo 73).

At the outset of this work, the hope was that for relatively simple $(\vec{p},t)$ transitions, for which good DWBA fits for the cross sections have been obtained, the analyzing powers too would be well described since both quantities are related to the transition amplitude in simple ways. It then might be possible for one to obtain further insight into the more complex $(\vec{p}, {}^3He)$ transitions and resolve some of the problems encountered in the unpolarized work. For example, it has been suggested that interference between coherently summed amplitudes might account for the abnormally low cross sections of certain $(p, {}^3He)$ transitions compared with their mirror (p,t) transitions (Fle 68a). Such interference effects might show up in the appropriate analyzing power data which are particularly sensitive to the spin-orbit coupling in the entrance and exit channels (Fle 68a, Tow 69).

It soon became evident, however, from some early results on $^{16}O$ and $^{15}N$ targets at 43.8 MeV (Har 70b), that the situation was more complex than had been expected. It turned out that the analyzing power was not necessarily characteristic, in any obvious sense, of the transferred quantum numbers even for simple transitions, while the situation for the even more puzzling complex transitions was totally unclear.

An additional direction of this work became, therefore, to obtain a fairly broad sample of analyzing power data in anticipation of future theoretical developments. This study has been confined primarily to transitions between 1p-shell nuclei including the results on $^{16}O$ and $^{15}N$ above, $^{13}C$ at 49.6 MeV, and $^{7}Li$ and $^{9}Be$ at 43.7 MeV. Some results on a $^{208}Pb$ target have also been included for reasons to be discussed in Chapter IV.

## II. THE EXPERIMENTS

If a polarized ion source is used to produce a beam of good quality and intensity, the measurement of analyzing powers for relatively low cross section reactions becomes not only feasible but also comparatively straightforward. Those techniques of detection and identification of outgoing reaction products can be utilized which have been well developed in unpolarized experiments. Any added complexity over the latter is manifested primarily in the number of measurements which are necessary, and in the amount of data handling and analysis to be done.

### A. The Source

The key, then, to these experiments has been the availability of the polarized ion source at the Lawrence Berkeley Laboratory 88-inch cyclotron. Two excellent general reviews of polarized ion sources and beams have been written by Haeberli (Hae 67, Hae 74).

The source for the 88-inch cyclotron (Luc 69, Cla 69) is of the atomic beam type, mounted above the cyclotron vault, so that beam is injected axially (vertically) through a hole in the upper main magnet pole and then inflected electrostatically into the horizontal median plane of the cyclotron. Both polarized protons and deuterons can be prepared. A cross sectional schematic diagram of the source is shown in Fig. 1. The remainder of the axial injection system (not shown) consists of three electrostatic triplet lenses in tandem which focus the beam to the cyclotron center, a buncher, which optimizes the injection of ions to be in phase with the cyclotron dee voltage, and the electrostatic inflector which is mounted through a hole in the lower main magnet pole

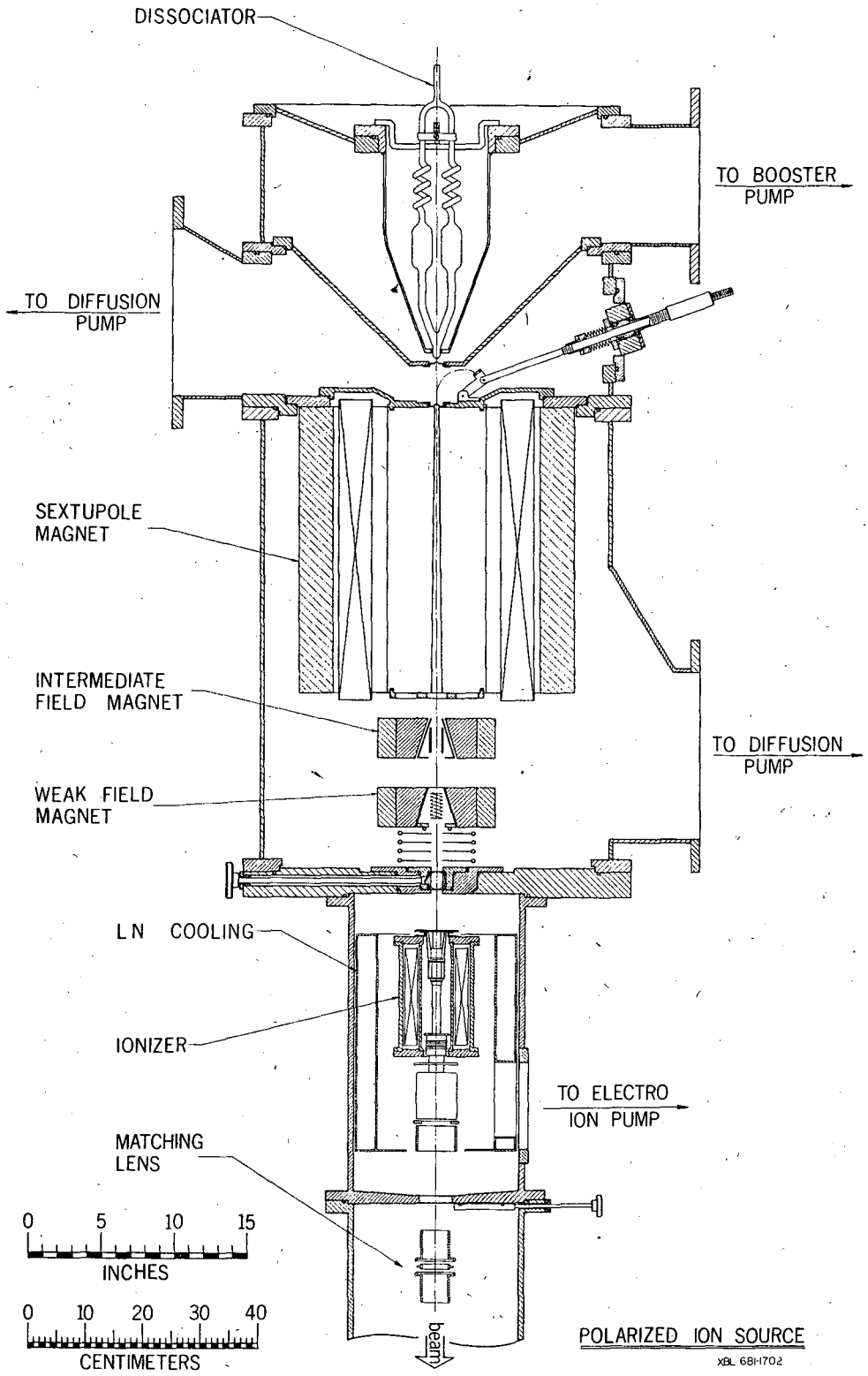


Fig. 1. Schematic diagram of the polarized ion source.

of the cyclotron in place of the normal internal ion source. In addition there is a system of electrostatic bending plates, collimators, current pick-ups, and air-driven removable Faraday cups which are also used in tuning maximum beam from the source to the cyclotron.

The production of polarized protons at the center of the cyclotron to be accelerated can be summarized as follows:

(1) Preparation of an atomic H beam from $H_2$ gas.

(2) Magnetic separation of the atomic substates.

(3) Induction of radiofrequency transitions between atomic substates in a weak magnetic field to achieve the required population distribution.

(4) Simultaneous ionization and final orientation of the polarized protons in a strong magnetic field.

(5) Electrostatic acceleration and focusing of the beam to the center of the cyclotron, where it is inflected 90° into the median plane.

With reference to Fig. 1, the operation of the source described more fully is as follows. $H_2$ gas is fed through a self regulating flow-controlling valve, at a pressure of $\sim$ 2 Torr and flow rate of $\sim$ 100 atm cc $min^{-1}$, into the dissociator where a 1.5 KW self excited oscillator induces the reaction

$$H_2 \xrightarrow{h\nu} 2H\cdot \qquad \nu \sim 20 \text{ MHz} \quad .$$

Atomic hydrogen is expanded through an orifice in the quartz dissociator tube into a second chamber maintained at a pressure of $\sim 10^{-2}$ Torr by a high volume blower pump backed by a mechanical pump. The atomic beam is

then passed through a second orifice into a pressure of $\sim 10^{-4}$ Torr pumped by two 10 inch diffusion pumps (D.P.'s). These two pressure differentials and orifice establish a fairly well collimated atomic beam, which is then passed through a third orifice into the sextupole magnet chamber at a pressure of $\sim 2 \times 10^{-6}$ Torr pumped by another D.P.

The sextupole magnetic field ($\sim$ 10k Gauss) effects a Stern-Gerlach separation of atomic substates by acting on the magnetic moment of the electron. Figure 2 shows the 1S energy level diagram for the hydrogen atom as a function of magnetic field, in which I, J, and F = I + J are the proton, electron, and atomic spins, respectively, and the subscripted m's are their respective spin projections. Atoms in states 1 and 2 for which $m_J = +1/2$, increase in energy, as shown, with increasing magnetic field and are therefore attracted to a region of minimum field which is along the axis of the sextupole and are therefore focused. By the same token, atoms with $m_J = -1/2$ are attracted to the strong field at the poles, are defocused, and pumped away. Emerging from the sextupole, then, is an atomic beam of pure $m_J = +1/2$.

The sextupole exerts a radial force on the atom which is linear with the radial distance, r, from the axis.[1] Since the beam enters the sextupole with finite divergence and radial extent, radial oscillations can be set up in the focused beam. However, since the magnetic aperture is tapered to increasing diameter at the exit, the restoring force on the atoms is reduced and the oscillations are damped, giving an atomic beam of good quality and radial stability entering the next source stage.

Upon leaving the sextupole, the atomic beam passes through the intermediate field magnet which is not used for protons (only for

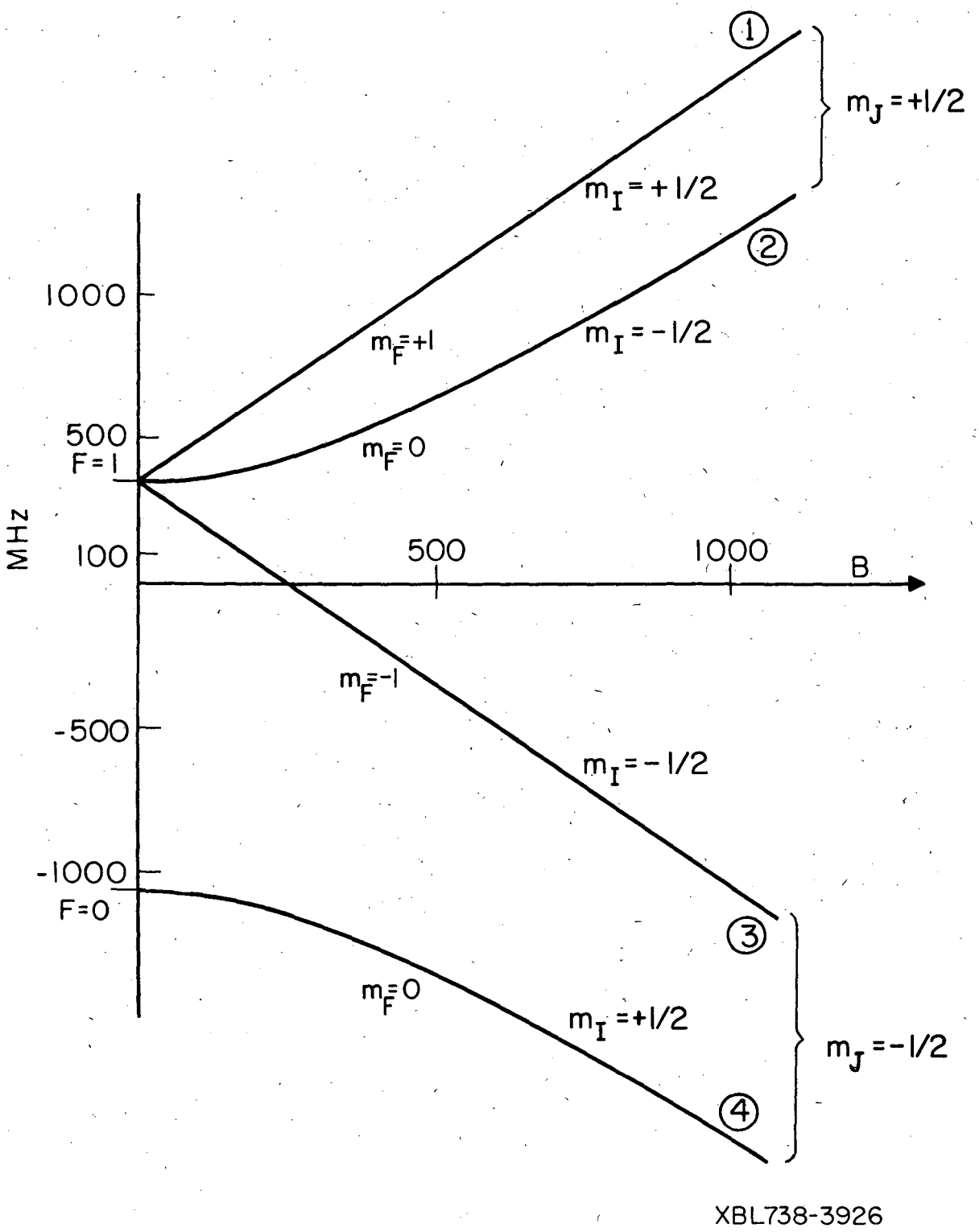


Fig. 2. Rabi diagram for the 1s state of hydrogen. The magnetic field B (abscissa) is in Gauss. The atomic quantum number F, is defined as $\vec{F} = \vec{J} + \vec{I}$ where J and I are the electron and proton spins, respectively.

deuterons) and enters the weak field magnet whose field lines are perpendicular to the beam axis. The change in the magnetic field is adiabatic; that is, the change is slow and smooth so that the atoms' spin vectors can follow the field lines. In the weak field, ($\sim$ 5 G.) F is a good quantum number, and states 1 and 2, and 2 and 3 are equally separated in energy. Transitions between states 1 and 3 (the latter being empty after the sextupole) are induced by an oscillating electric field of $\sim$ 7.5 MHz which is parallel to the beam axis. The beam leaving the transition region then is all in states 2 and 3 and has $m_I = -1/2$.

The transition $1 \rightarrow 3$ is not reversible since the population of 3 is initially zero and, because the pole faces of the weak field magnet are tapered, the exact resonance conditions are met only over a very short distance. Therefore, these conditions exist for a very short time for each atom, and the efficiency of the transition is 99.5 ± 0.5% (Gla 69).

Since state 2 is a mixed state of opposite proton and electron spins, the proton has no preferred direction in zero magnetic field. The polarization of the protons is defined as $p = N^+ - N^-/N^+ + N^-$, where $N^i$ is the number of protons for which the sign of $m_I$ is "i". The polarization in state 2 therefore depends strongly on the external magnetic field, being zero in zero field and -1 in strong field. However, state 3 is a pure state of polarization -1, independent of external field. Hence, in a strong field, a maximum beam polarization of -1 is possible.

Therefore, the atomic beam enters a strong solenoid whose field ($\sim$ 1500 G.) is parallel or anti-parallel to the beam direction, depending on the current direction in the solenoid. The final direction of the beam polarization is determined by the direction of the solenoid field.

It is also in this field that the atoms are ionized by electron impact. No depolarization occurs during ionization since the duration of the impact is short relative to the Larmor precision period.

This source is capable, in principle, of $\sim$ 100% polarization; in practice, the Berkeley facility achieves $|p_y| \sim$ 75-85%.[2] Two main factors prevent realization of the theoretical limit. The first is the presence of an unpolarized hydrogen background in the residual vacuum of the ionizer originating primarily from water and pump oil. This factor is minimized by the use of liquid nitrogen traps and good pumps. The second factor is depolarization arising from scattering of polarized protons with the residual gas, which can also be minimized by careful ionizer design and good pumps. The ionizer at Berkeley operates at a normal pressure of $10^{-7}$ Torr maintained by an electro-ion pump.

After ionization the polarized beam is accelerated through several kV (depending on the final energy to be extracted from the cyclotron). The accelerated beam is then focused to the center of the cyclotron where it is deflected 90° by an electrostatic mirror whose field is inclined at 45° to the beam direction. The mirror is at approximately the same potential as the accelerating voltage.

## B. Experimental Layout

The experimental apparatus for these experiments included the source, the cyclotron, the beam transport system and the scattering chamber and polarimeter in the experimental cave. The associated electronics were located remote from the apparatus in the counting room. With the exception of the polarized ion source discussed in part A of this chapter,

the experimental apparatus differed little from that used for conventional unpolarized experiments and will be described rather briefly. Figure 3 is a schematic diagram of the equipment.

The cyclotron and its operation have been described elsewhere (Con 66). The center region of the machine has been modified (Luc 69) to accept ions from the inflector which is on axis rather than from the normal ion source which is located (when used) off center. The modifications consist mainly of inserts fixed to the dee and dummy-dee which precisely control the rf field lines for the first few turns in the machine to establish the spiral accelerating beam orbit centered on the machine axis, to avoid loss of the beam due to vertical oscillations, and to insure that the beam initially clears the inflector on its first turn.

The extracted beam, after having been acted upon by X and Y collimators (not shown) and the first quadrupole doublet, was deflected 20° by the switching magnet into the Cave 5A beam line. Collimators located just inside Cave 5 at a radial focus provided for some beam energy analysis, although the small deflection angle at the switching magnet yielded only minimal energy dispersion. Final focusing of the beam at the center of the 36-inch scattering chamber was achieved using a second quadrupole doublet in Cave 5. Additional collimators located in the chamber in front of the target provided final clean-up of the beam and, being electrically isolated, were used as current pickups to monitor beam centering during the experiment. Beam centering could also be determined in a split Faraday cup at the end of the beam line which fed two current meters connected to a single integrating electrometer. A small steering magnet

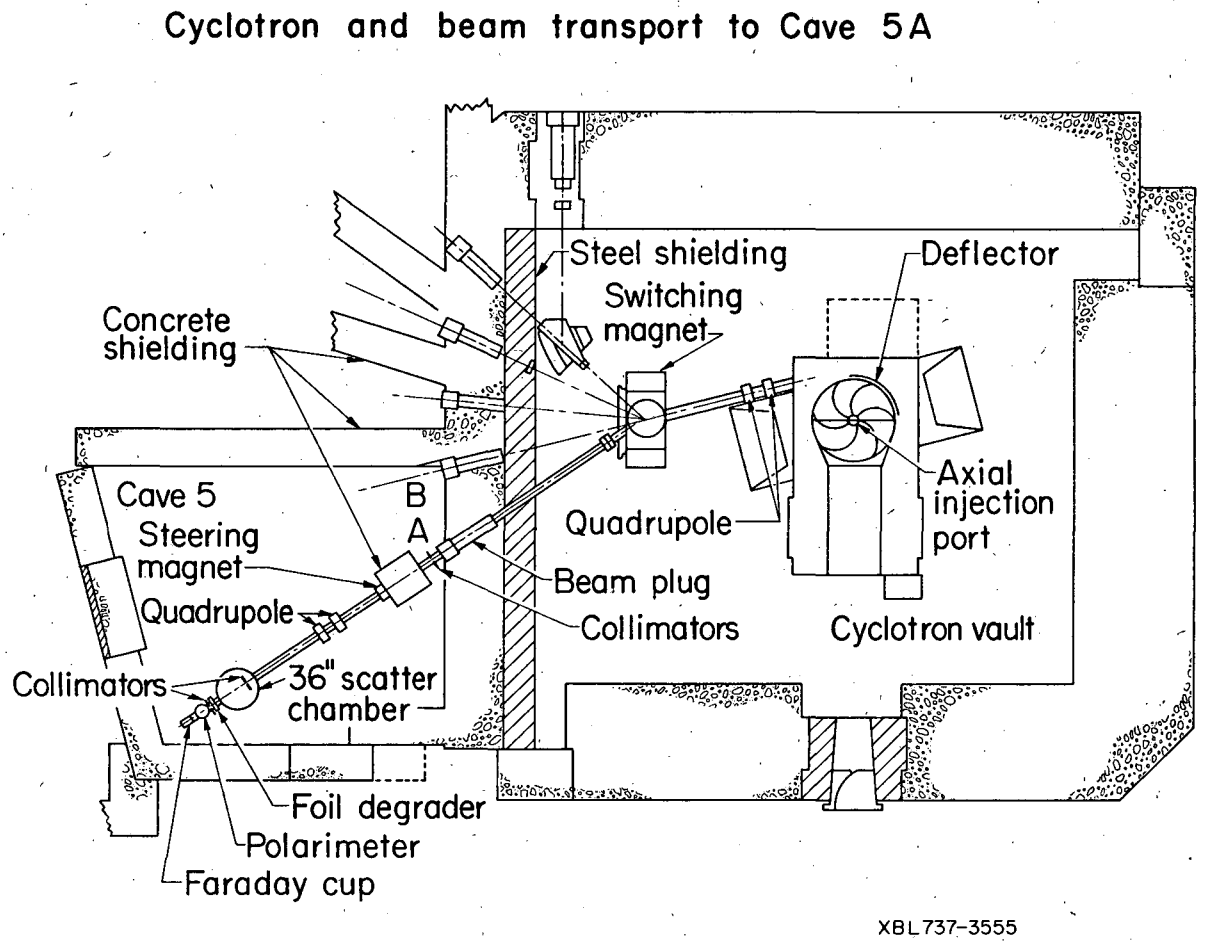


Fig. 3. Schematic layout of the cyclotron and Cave 5A experimental area.

$\sim$ 4 m upstream from the scattering chamber was used to maintain beam centering.

The scattering chamber itself is 36 inches (91.44 cm) in diameter and contains two motor-driven wedge-shaped platforms upon which the detector telescopes were mounted and which pivot about the center of the chamber. The detector angles could be set remotely using television monitors viewing angle scales which moved with each detector platform. Two fixed counters in the lid of the chamber at $\theta = \pm 8^{\circ}$, and $10^{\circ}$ above the reaction plane were used as monitors, to observe the target condition and to obtain a normalization for cross section measurements. Both gas and solid targets were mounted in a motor-driven frame whose position could be remotely controlled and monitored.

Located between the scattering chamber and the Faraday cup were the foil degrader wheel assembly and the polarimeter. The former was used to degrade the 49.6 MeV proton beam to 39.8 MeV since the polarimeter was not calibrated at the higher energy. The polarimeter was a smaller and simpler scattering chamber containing a gas target cell with 5 $\mu$m Havar foil windows holding $^4$He at $\sim$ 1 atm pressure. Beam leaving the scattering chamber target was recollimated before entering the polarimeter. Elastic scattering of the incident protons on $^4$He could be measured by two counter telescopes located symmetrically about the beam axis at a back angle observing maximum analyzing power for p-$\alpha$ scattering ($\sim 130^{\circ}$). Beam polarization was calculated from the known analyzing power of $^4$He for protons (Bac 72), and the measured asymmetry in the polarimeter.

## C. Targets

The motor-driven target mount in the scattering chamber could be fitted with either of two target assemblies: One was a simpler ladder type of target foil holder with five positions, one of which was reserved for the scintillator plate used in tuning the beam optics. The second assembly comprised a two-position ladder and a cylindrical gas cell with 5 μm Havar foil windows. The gas cell was connected to an external gas handling system capable of recovering valuable gas samples from the target cell. This system, as used in a different chamber has been described in detail elsewhere (Har 70a). Gas pressure was monitored in a differential pressure gauge. Gas temperature was measured by a thermocouple fixed to the target cell.

The $^{16}O$, $^{15}N$, and $^{13}C$ experiments were done with gas targets using $^{16}O_2$, $^{15}N_2$ enriched to 99%, and $^{13}CH_4$ enriched to 93%. Typical target gas pressures were 200 Torr. The $^{9}Be$, $^{7}Li$, and $^{208}Pb$ experiments utilized self supporting evaporated foils which were 650 $\mu g/cm^2$, 500 $\mu g/cm^2$, and 2 $mg/cm^2$ thick, respectively.

## D. Detectors and Electronics

Outgoing reaction products were detected by semiconductor counters made at the Lawrence Berkeley Laboratory detector lab. With the exception of the two monitor counters in the scattering chamber which were single thick detectors, all detector systems were double, consisting of a thin phosphorus diffused silicon transmission $\Delta E$ counter and a thick Li-drifted silicon E detector (Gou 65). The particular thicknesses of detectors used for each experiment depended on the Q-value of the reactions and

the ranges of the particles of interest. Each detector fed a charge sensitive preamplifier located in the experimental cave whose output was in turn fed to a linear amplifier located in the counting room.

For the two single monitor counters, linear amplifiers capable of high counting rates were used since the counters looked at forward angle elastic scattering with a high cross section and large background. The slow output of each amplifier was fed to a single channel analyzer (S.C.A.) as well as to a linear gate which was triggered by the S.C.A. In this way only events from the peak of interest in each monitor were fed to a biased amplifier and output shaper and then routed to a pulse height analyzer (PHA) and also to a scaler.

Outgoing tritons and $^{3}$He's were detected in four two-counter telescopes mounted on the movable detector platforms in the chamber. The two systems on each side of the beam axis were mounted $10^{\circ}$ apart on the platform, and the platforms were always set so that the two pairs of telescopes were symmetrically oriented about the beam axis as shown in the upper left-hand corner of Fig. 4. Collimators (single for solid targets, double for gas targets) were such that the angular dispersion was $1.1^{\circ}$ and the solid angle was $1 \times 10^{-4}$ sr.

Figure 4 also outlines schematically the remote electronics fed by the detectors which was utilized to identify particles of interest and store the data. Signals from the $\Delta$E- and E-preamplifiers were amplified and required to meet fast coincidence criteria ($2\tau \sim 100$ ns) and were then fed to a Goulding-Landis particle identifier. The operation of this device which depends on an empirical power-law for the range of charged particles in silicon, $R \sim aE^{1.73}$, where $a$ is characteristic of

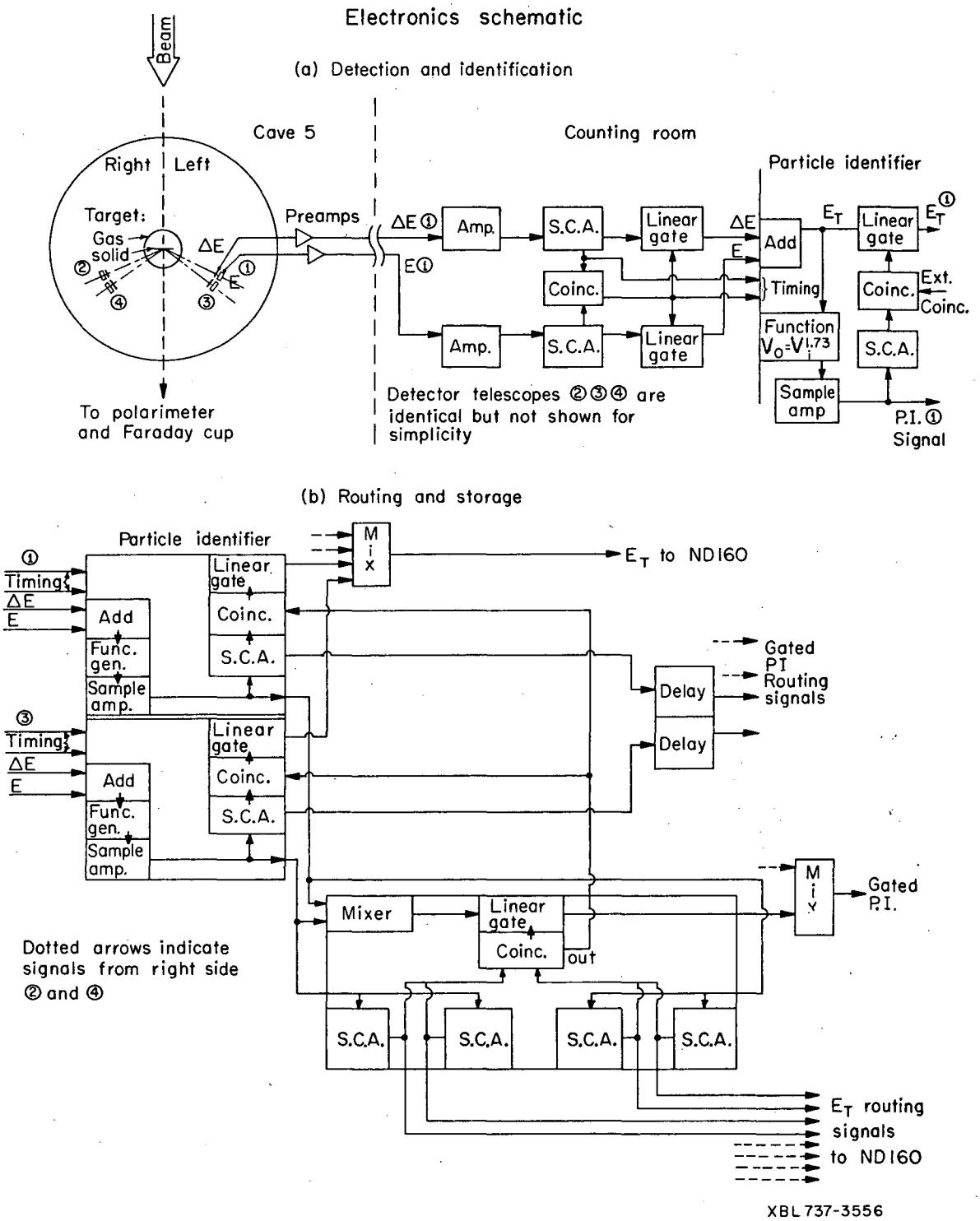


Fig. 4. Schematic diagram of the electronics.

particle type has been given elsewhere (Gou 64). Particle identifier spectra were obtained which were comparable to those obtained by e.g. Fle 67. Identifier signals corresponding to tritons and $^3$He's were fed to S.C.A.'s in an external 4-channel router whose output was used to gate the total energy signals, $E_T$, and to generate routing signals for the Nuclear Data 160, 4096-channel analyzer in which $E_T$ was stored.

The electronics used for the polarimeter were similar to those used in the chamber, but simpler since only two telescopes were used and only elastic protons needed to be identified and stored.

## E. Data Collection and Analysis

Total energy signals for identified particles of interest were routed into the Nuclear Data 160 pulse height analyzer which was operated in either 16 × 256 channel or 8 × 512 channel mode. For each set of angles, two sets of spectra were collected, one for each of the two orientations of the incident proton spin. Therefore all the data for a particular set of two angles could be stored together in the analyzer-16 spectra in all if both tritons and $^3$He's were collected; 8 spectra if (as for the $^{208}$Pb target) only tritons were of interest. Data from the analyzer were transferred to magnetic tape via a PDP-5 computer after each set of angles for subsequent analysis.

As an example, consider the spectra shown in Fig. 5 obtained from the $^{208}$Pb target at $\theta_{lab} = 37.5^\circ$. These four spectra are used to obtain a single analyzing power value at this angle for each of the states labeled by $J^\pi$. As will be presented later in Chapter IV, this particular angle happens to be near a maximum analyzing power for both the ground (0+) and

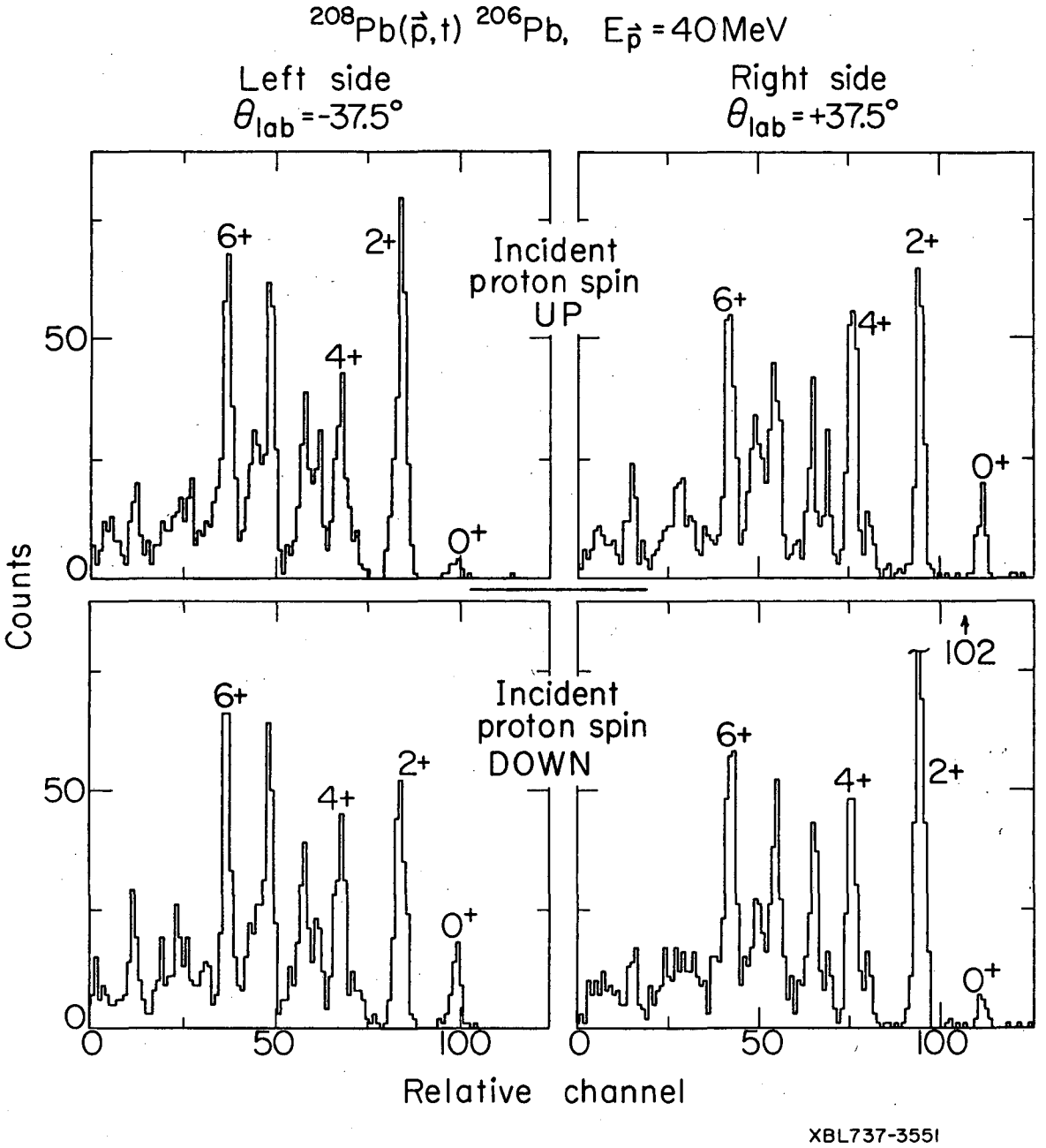


Fig. 5. Example of four of the spectra from which a measurement of analyzing power is taken. The beam polarization was $|p_y| = 0.794 \pm 0.013$.

first excited ($2^+$) states. It is quite evident from the figure that an asymmetry exists for both of these states, which reverses sense when the polarization of the beam is reversed.

For a particular state (e.g., the ground state) the number of counts in a peak, $N_i^j$, for the $i^{th}$ side and incident beam polarization $j$, is proportional to the cross-section $\sigma_i^j$ over the exposed solid angle, times that solid angle $\Omega_i$, i.e. $N_i^j \propto \sigma_i^j \Omega_i$. The observed asymmetry, $e_y$ is determined as

$$e_y = \frac{N_L - N_R}{N_L + N_R}$$

$$= \frac{\sigma_L \Omega_L - \sigma_R \Omega_R}{\sigma_L \Omega_L + \sigma_R \Omega_R} \quad ,$$

if the beam polarization is fixed. Notice that $e_y$ depends on the solid angle $\Omega_i$ and therefore is sensitive to any instrumental asymmetry. This dependence on instrumental asymmetry can be removed in first order (Pla 68) by using data obtained for both beam polarizations: Rearrange the above to

$$e_y^{\uparrow} = \frac{1 - \frac{N_R^{\uparrow}}{N_L^{\uparrow}}}{1 + \frac{N_R^{\uparrow}}{N_L^{\uparrow}}} = \frac{1 - r^{\uparrow}}{1 + r^{\uparrow}} \quad ,$$

where

$$r^{\uparrow} = \frac{N_R^{\uparrow}}{N_L^{\uparrow}} = \frac{\sigma_R^{\uparrow} \Omega_R}{\sigma_L^{\uparrow} \Omega_L} \quad ; \quad \text{also} \quad r^{\downarrow} = \frac{\sigma_L^{\downarrow} \Omega_L}{\sigma_R^{\downarrow} \Omega_R} \quad .$$

Now

$$\frac{\sigma_R^{\uparrow}}{\sigma_L^{\uparrow}} \equiv \frac{\sigma_L^{\downarrow}}{\sigma_R^{\downarrow}} \quad ,$$

since the two ratios are obtained from identical experiments differing only in a physical rotation by $\phi = 180^{\circ}$ in the lab. The dependence on instrumental asymmetry can be removed from $r^{\uparrow}$ and $r^{\downarrow}$ by considering the geometrical mean

$$(r^{\uparrow}r^{\downarrow})^{1/2} = \left(\frac{\sigma_R^{\uparrow}}{\sigma_L^{\uparrow}} \frac{\sigma_L^{\downarrow}}{\sigma_R^{\downarrow}} \times \frac{\cancel{\sigma_R}}{\cancel{\sigma_L}} \frac{\cancel{\sigma_L}}{\cancel{\sigma_R}}\right)^{1/2}$$

$$= \left(\frac{\sigma_R^{\uparrow 2}}{\sigma_L^{\uparrow 2}}\right)^{1/2} = \frac{\sigma_R}{\sigma_L} = r \quad ,$$

which leaves only the ratio which depends on the analyzing power of the nuclear reaction. Then $e_y = \frac{1 - r}{1 + r} = p_y \cdot A_y$ where $A_y$ is the analyzing power of the reaction and $p_y$ is the incident beam polarization.[2] The above argument is exact if the beam polarization is the same in magnitude for both orientations, and is true to first order in any case. Since for most polarized ion sources, and for the Berkeley source in particular $|p_y| \simeq$ constant, this procedure removes any effects of instrumental asymmetry, so long as such asymmetry is constant during the complete measurement.

Analyzing the polarimeter data to obtain beam polarization follows identically except that here $A_y$ is known, and $p_y$ is determined from the measured $e_y$.

In the apparatus used for these experiments, care was taken to make $\frac{\Omega_L}{\Omega_R} \cong 1$, i.e. the instrumental asymmetry was minimal. Therefore an additional check on the data could be obtained by calculating the value of

$$\left( \frac{N_R^{\uparrow}}{N_L^{\uparrow}} \cdot \frac{N_R^{\downarrow}}{N_L^{\downarrow}} \right)^{1/2} ,$$

and ensuring that it be statistically constant and approximately unity.

Relative differential cross sections were obtained by summing the counts in the peaks from the four spectra and normalizing either to the monitor or to the Faraday cup readings or both. The cross sections which appear in the figures in Chapter IV, have been further normalized by a common factor for each target to previously determined absolute values available in the literature (e.g. Cer 64, Fle 71, Fle 68a, Fle 68b, Cer 66, Smi 70). The analyzing powers are, of course, not affected by this normalization procedure.

# III. THEORETICAL CONSIDERATIONS

The nuclear processes which have been considered in this work can be conveniently characterized in terms of the values of the angular momenta and parity which are transferred. Furthermore, since the mechanism of these transitions has been assumed to be a direct process, it can be formulated mathematically using the distorted wave Born approximation (DWBA). In this chapter, then, the angular momentum and parity selection rules which pertain to direct (p,t) and (p, $^3$He) reactions will first be outlined, followed by a brief discussion of the DWBA theory which has been applied in an attempt to account for the experimental results.

## A. Selection Rules

The total angular momentum J transferred by two nucleons 1 and 2, between an initial and final state is given by

$$\vec{J}_f = \vec{J}_i + \vec{J} \quad ; \quad \vec{J} = \vec{j}_1 + \vec{j}_2 \tag{1}$$

J is the vector sum of the transferred orbital angular momentum L and the transferred intrinsic angular momentum (spin) S;

$$\vec{J} = \vec{L} + \vec{S} \quad ; \quad \vec{L} = \vec{\ell}_1 + \vec{\ell}_2$$

$$\vec{S} = \vec{s}_1 + \vec{s}_2 \quad . \tag{2}$$

The transferred isospin T is given by

$$\vec{T}_f = \vec{T}_i + \vec{T} \quad , \tag{3}$$

and is related to the transferred spin (by requiring antisymmetry for the total wave function of the two transferred nucleons):

$$S + T = 1 \quad . \tag{4}$$

For (p,t), T = 1 so that S = 0; for (p, $^3$He), T can be either 0 or 1, so that S is either 1 or 0, respectively.

The parity change is given by

$$\Delta\pi = (-1)^{\ell_1 + \ell_2} = (-1)^L \quad , \tag{5}$$

if the two nucleons are in a relative S-state.

More extensive treatments of these rules can be found in the many articles on direct reactions (e.g. Gle 63, Gle 65, Tow 69).

## B. DWBA Calculations

Distorted wave Born approximation calculations have been undertaken to predict the shapes of differential cross sections and analyzing powers using the program DWUCK.[3] This is a zero-range code which permits a spin-orbit distortion to be included in the optical potentials. The following discussion will outline the theory upon which the program is based.

### 1. Outline of the Method

The theory adopted in this work has been advanced and developed entirely by others and a number of excellent and detailed accounts exist elsewhere. Among the works which provide a rather complete theoretical background are the following; Rom 65, Dav 66, Tob 61, Sat 64, Aus 64,

Gle 63, Gle 65, Tow 69. Also of interest is a recent survey (Kah 71) of DWBA calculations for (p,t) reactions in the 1p-shell.

The applicability of the Born approximation is based largely on the assumption of a direct mechanism. That is, the interaction responsible for the transition is assumed to occur only once and to endure for a time of the order of the nuclear transit time for the bombarding particle ($\sim 10^{-22}$ sec). As a result only a few nucleons are involved and only a few degrees of freedom in the nuclear system are excited. The principal experimental characteristic which distinguishes a direct process from, say, a statistical or compound nuclear event is a strongly forward peaked cross section, often displaying a diffraction pattern, whose magnitude is relatively insensitive to the bombarding energy at energies substantially above the threshold. At the incident proton energies employed in these experiments (40 - 50 MeV), the assumption of a purely direct process is a valid one in general.

In a distorted wave calculation the transition is treated as occurring between elastic scattering states; that is, incoming and outgoing particles are described by wave functions which are solutions of the Schroedinger equation which contains an optical potential giving the effects of nuclear forces in an average way, including absorption, Coulomb effects, and spin-orbit distortion.

The DWBA theory characterizes a pickup transition such as (p,t) between a target nucleus A and a residual nucleus B by a transition amplitude $T_{fi} \equiv T_{fi}(J_A M_A \mu_i \rightarrow J_B M_B \mu_f)$ where J, M, and $\mu$ are total angular momentum, total angular momentum projection and light particle spin projection, respectively. The transition amplitude is of the form

$$T_{fi} \propto \int dr_i \int dr_f \, \chi^{(-)*}(k_f, r_f) \, \langle B, f | V | A, i \rangle \, \chi^{(+)}(k_i, r_i) \quad . \quad (6)$$

Here the $\chi$'s are the distorted waves mentioned above which describe the elastic scattering states. The interior matrix element of the interaction which causes the transition is called the form factor and contains the information on nuclear structure, reaction mechanism and selection rules. The differential cross section is expressed in terms of the $T_{fi}$

$$(d\sigma/d\Omega) \propto \sum_{M_A M_B \mu_i \mu_f} |T_{fi}|^2 \quad . \quad (7)$$

If a spin dependence is included such as is the case for distorted waves generated by optical potentials which include a spin-orbit strength, the differential cross section can be written (Gle 63, Gle 65)

$$(d\sigma/d\Omega) \propto \sum_{M\mu_f\mu_i}^{J} \left| \sum^{\gamma LST} G_{\gamma LSJT} \, B^{LSJT}_{M\mu_i\mu_f} \right|^2 \quad . \quad (8)$$

where LSJT are the quantum numbers of the transferred pair, $\gamma$ is the configuration of the transferred nucleons ($[n\ell j][n'\ell' j']; JT$), G is the spectroscopic or structure amplitude including a spectroscopic factor for the light particles, and B is the kinematic and angular momentum transfer amplitude which includes the distorted waves obtained from the elastic scattering optical parameters. Transforming the spatial part of the wave function of the two nucleons in state $\gamma$ to relative and center-of-mass coordinates and restricting their relative motion to S-state, the differential cross section takes the form

$$(d\sigma/d\Omega) \propto \sum_{M\mu_i\mu_f}^{J} \left| \sum^{LST} \sum^{N} G_{NLSJT}\, B^{LSJT}_{M\mu_i\mu_f} \right|^2 , \qquad (9)$$

where N is the principal quantum number of the center-of-mass motion.

The center-of-mass motion of a pair of nucleons in a pure state (jj') can be described as a projected wave function outside a passive core;

$$\tilde{\phi}_{jj',JST}(\underset{\sim}{R}) = \sum \tilde{u}_{jj',LSJT}(\underset{\sim}{R})\; Y_L(\hat{\underset{\sim}{R}}) , \qquad (10)$$

where the tilde signifies a projected wave function, and $Y_L(\hat{\underset{\sim}{R}})$ is a spherical harmonic.

The structure factors arise in the expansion of the radial function $\tilde{u}(R)$ in a harmonic oscillator function basis:

$$\tilde{u}_{jj',LSJT}(R) = \sum_{N} G_{NLSJT}(jj')\; u_{NL}(2\nu R^2) . \qquad (11)$$

For two nucleons in a mixed configuration the projected radial wave function is of the form

$$\tilde{\psi}_{JST}(R) = \sum_{jj'} \beta_{jj'}\, \tilde{\phi}_{jj',JST}(R) , \qquad (12)$$

where $\beta_{jj'}$ is a coefficient of fractional parentage (cfp). Then

$$\tilde{\psi}_{JST}(R) = \sum_{jj'} \beta_{jj'} \sum_{L} \sum_{N} G_{NLSJT}(jj')\; u_{NL}(2\nu R^2) , \qquad (13)$$

where $G_{NLSJT} = \sum_{jj'} \beta_{jj'} G_{NLSJT}(jj')$. The evaluation of $G_{NLSJT}$ will be discussed in section B-2 of this chapter.

Polarization effects in direct reactions have been rather extensively discussed by Goldfarb and Johnson (Gol 60). An earlier paper by Wolfenstein (Wol 56) discusses a number of concepts related to polarized nucleons and contains some useful definitions. Two more elementary articles (Bar 67, Ros 67) exist which provide a good introductory treatment of polarization phenomena along with (Gla 69) which is more extensive.

From an experimentalist's point of view the nature of the analyzing power for a $(\vec{p},t)$ reaction, for example, can best be visualized by considering the reverse $(t,\vec{p})$ transition. Time reversal invariance requires that the analyzing power in the former be equal to the polarization of the outgoing protons in the latter as induced by an unpolarized triton beam (Hae 74). The polarization is then directly related to the transition amplitude $T_{fi}$ in the following way.

If the two projections of a spin 1/2 particle are designated + and -, then the probability in terms of the previously defined transition amplitude that the outgoing proton will have a spin + is

$$\xi_+ = \sum_{M_A M_B \mu_t} |T_{fi}(M_B \mu_f \rightarrow M_A +)|^2 \quad . \tag{14}$$

The polarization p is defined as

$$p \equiv \frac{\xi_+ - \xi_-}{\xi_+ + \xi_-} \quad . \tag{15}$$

In terms of the differential cross section, then,

$$p = \frac{\sigma_{++} + \sigma_{-+} - \sigma_{+-} - \sigma_{--}}{\sigma_{++} + \sigma_{-+} + \sigma_{+-} + \sigma_{--}} \quad , \tag{16}$$

where we have abbreviated $\sigma_{-+} \equiv (d\sigma/d\Omega)\Big|_{\substack{\mu_t = - \\ \mu_p = +}}$ , etc.

2. Nuclear Structure

The two-nucleon transfer form factors were obtained in these calculations following the method of Glendenning (Gle 63, Gle 65) which uses harmonic oscillator wave functions for the transferred pair. The nuclear structure of the initial and final states enters the calculations via the $G_{NLSJT}$ in Eq. (9) which are defined following Eq. (13).

For the calculations in the 1p-shell the cfp's $\beta_{jj'}$ were obtained from a compilation by Cohen and Kurath (Coh 70) based on wave functions derived from an earlier effective-interaction calculation (Coh 65). The $G_{NLSJT}(jj')$ were derived from Glendenning's tables of (p,t) and (p, $^3$He) structure amplitudes (Gle 68) by making suitable corrections (Gle 65, Gle 73) for the oscillator parameter $\nu = 0.32\ F^{-2}$ which was taken from True (Tru 63).

Negative parity mass-14 residual states, which must involve some sd admixture to the 1p-shell, were assumed to have simple shell model configurations suggested by the $^{14}$N wave functions of True (Tru 63). These cases will be discussed more specifically in Chapter IV.

Calculations for $^{208}$Pb$(\vec{p},t)^{206}$Pb were done using the complete structure factors obtained by Reynolds et al. (Rey 67) who used wave

functions of True and Ford (Tru 58). In a comparison with other wave functions for the ground state transition, other structure amplitudes calculated by Broglia and Riedel (Bro 67) were employed.

3. Optical Potentials

A full description and justification of the optical model itself is available elsewhere (e.g. Fes 58, Hod 71). The proper choice of parameters characterizing the optical potential in the Schroedinger equation is often difficult, but nevertheless essential to the success of meaningful DWBA computations. Ideally one obtains, or has available data for the elastic scattering processes involving the appropriate channels at the same energy as occur in the reaction, and then determines a parameter set which accurately describes these data in the optical model. More often than not, however, these circumstances do not prevail, and it becomes a matter of experience and judgment to choose parameters from elastic scattering experiments using target nuclei of nearby mass and at similar bombarding energies.

Since for most of the reactions under study in this work, calculations have been done by others predicting differential cross sections, we have relied heavily on their experience rather than embarking on an entirely independent search for optical parameters. In addition, a recent compilation of optical model parameters (Per 72) has been consulted. The potentials used in the 1p-shell calculations are summarized in Table I. All calculations were done with a spin-orbit potential in the proton channel and some comments regarding the inclusion of a mass-3 spin-orbit term appear in section B-4 of this chapter.

Table I. Optical Model Parameters[a] used in DWBA in the lp-Shell.

| Target | Particle | $V_0$ (MeV) | $W_0$ (MeV) | $W_1$ (MeV) | $V_S$ (MeV) | $r_0$ (fm) | $r_0'$ (fm) | $r_s$ (fm) | $r_c$ (fm) | a (fm) | a' (fm) | $a_s$ (fm) | Ref. |
|---|---|---|---|---|---|---|---|---|---|---|---|---|---|
| $^{15}N$, $^{16}O$ | proton (43.8 MeV) | 44.53 | 17.51 | 6.51 | 6.20 | 1.141 | 1.26 | 1.066 | 1.3 | 0.715 | 0.64 | 0.674 | b |
| | mass-3 | 220.0 | 23.8 | -- | -- | 1.22 | 1.80 | -- | 1.3 | 0.530 | 0.990 | -- | c |
| $^{13}C$ | proton (49.6 MeV) | 38.38 | 21.49 | 3.81 | 5.75 | 1.141 | 1.26 | 1.066 | 1.3 | 0.715 | 0.64 | 0.674 | b |
| | mass-3 | 160.0 | 14.86 | -- | -- | 1.31 | 1.73 | -- | 1.3 | 0.565 | 0.826 | -- | d |
| | | 169.0 | 32.1 | -- | -- | 1.14 | 1.82 | -- | 1.4 | 0.675 | 0.566 | -- | e |

[a]The optical potential was defined as:

$$V(r) = V_c(r) - V_0\left(\frac{1}{e^x + 1}\right) - iW_0\left(\frac{1}{e^{x'} + 1}\right) - iW_1 e^{-x'^2} - \left(\frac{\hbar}{M_\pi c}\right)^2 V_S \frac{1}{r}\frac{d}{dr}\left(\frac{1}{e^{x_s} + 1}\right) \vec{\sigma} \cdot \vec{\ell}$$

where $V_c(r)$ is the Coulomb potential for a uniformly charged sphere of radius $r_c A^{1/3}$ fm; $x = (r - r_0 A^{1/3})/a$, $x' = (r - r_0' A^{1/3})/a'$ and $x_s = (r - r_s A^{1/3})/a_s$.

[b]Quoted in reference (Fle 71) from proton elastic scattering on $^{16}O$.

[c]Quoted in reference (Fle 71) determined from $^{3}He$ elastic scattering on $^{12}C$.

[d]From (Per 72). This potential yielded the most favorable overall fits in $^{13}C$ transitions which are presented in Chapter IV.

[e]Quoted in reference (Fle 71) from $^{3}He$ elastic scattering on $^{14}N$; yielded generally poorer fits than (d). See text Chapter IV.

For the calculations for the $^{208}Pb(\vec{p},t)^{206}Pb$ reactions, it was fortunate that the exact elastic scattering data for the entrance channel (40 MeV protons on $^{208}Pb$) were available (Fri 67) and in fact had been used to obtain excellent differential cross section fits for the transitions which we are considering (Smi 68, Smi 70). In addition, a global prescription for proton optical potentials has been found by Becchetti and Greenlees (Bec 69) and was also used in these calculations.

The situation for the triton exit channel is, however, less ideal. Some elastic scattering data have been obtained for tritons (Fly 69) but at an energy of 20 MeV, which is much lower than that encountered in these experiments ($\sim$ 34 MeV triton lab energy). Also a global prescription (Bec 71) similar to that for protons has been developed but the input data to that search were also low energy ($\leq$ 20 MeV). Although potentials from both these sources were examined, very poor fits resulted, and therefore, for the fits which are presented here, we followed the example of (Smi 68, Smi 70) and used a triton potential from Glendenning (Gle 67). The parameters used for the lead calculations included spin-orbit distortion only in the proton channel and are summarized in Table II.

4. Further Specific Assumptions

In addition to those approximations inherent in the derivation of the DWBA method from formal scattering theory, a number of other assumptions can be made which lead to substantial simplification in the actual calculations. Although each of these assumptions can reduce the power of the theory in principle, it is possible to illustrate for particular circumstances that in fact a small price is paid for the benefits of simplicity.

Table II. Optical Parameters[a] used in DWBA for $^{208}Pb(\vec{p},t)^{206}Pb$.

| Particle | $V_0$ (MeV) | $W_0$ (MeV) | $W_D$ (MeV) | $V_S$ (MeV) | $r_0$ (fm) | $r_0'$ (fm) | $r_s$ (fm) | $r_c$ (fm) | a (fm) | a' (fm) | $a_s$ (fm) | Ref. |
|---|---|---|---|---|---|---|---|---|---|---|---|---|
| proton (scattering) | 54.62 | 5.31 | 5.60 | 5.84 | 1.125 | 1.386 | 1.026 | 1.25 | 0.873 | 0.624 | 0.794 | b |
| (global) | 51.8 | 6.1 | 4.338 | 6.2 | 1.17 | 1.32 | 1.01 | 1.17 | 0.75 | 0.658 | 0.75 | c |
| triton | 160.0 | 20.0 | -- | -- | 1.1 | 1.6 | -- | 1.4 | 0.75 | 0.75 | -- | d |

[a]The optical potential was defined as:

$$V(r) = V_c(r) - V_0\left(\frac{1}{e^x + 1}\right) - i\left(W_0 - 4W_D \frac{d}{dx'}\right)\left(\frac{1}{e^{x'} + 1}\right) + \left(\frac{\hbar}{M_\pi c}\right)^2 V_S \frac{1}{r}\frac{d}{dr}\left(\frac{1}{e^{x_s} + 1}\right) \vec{\sigma} \cdot \vec{\ell}$$

where $V_c(r)$ is the Coulomb potential for a uniformly charged sphere of radius $r_c A^{1/3}$ fm; $x = (r - r_0 A^{1/3})/a$, $x' = (r - r_0' A^{1/3})/a'$, and $x_s = (r - r_s A^{1/3})/a_s$.

[b]From (Fri 67), 40 MeV elastic scattering on $^{208}Pb$.

[c]From (Bec 69), derived from a global prescription therein.

[d]From (Gle 67), and references therein.

A major objective of this work has been to determine to what extent an understanding of the analyzing powers for these two-nucleon transfer reactions can be derived from reasonably elementary methods, and therefore, three further approximations have been incorporated into the calculations:

(i) Spin-Isospin in the Two Particle Interaction. Under certain conditions it is possible to factor a quantity D(S,T) (Tow 69, Gle 65) out of the radial integrals contained in B of Eq. (9). D(S,T) is directly related to the two-body exchange mixture in the interaction potential of the form factor (Eq. (6)), describing the relative strength of S = 0 and S = 1 transfer which can occur in most (p, $^{3}$He) transitions. Investigations (Fle 68a, Fle 71) have shown that S = 0 transfer is enhanced by about a factor of three over S = 1 as determined from cross section ratios for (p,t) and (p, $^{3}$He) transitions to mirror states. In order to evaluate the effects of this factor on analyzing powers, some (p, $^{3}$He) transitions on the $^{13}$C and $^{15}$N targets were calculated multiplying the appropriate G-factors for S = 0 by $\sqrt{3}$. The results showed no dramatic effects on the shape of the analyzing power, and no improvements of the fits to the data were obtained. Some of these results are illustrated in Chapter IV for $^{15}$N($\vec{p}$, $^{3}$He)$^{13}$C.

In view of the as yet not understood effects evident in some simple ($\vec{p}$,t) transitions which will be shown in Chapter IV, and on the basis of the above mentioned survey, this spin dependence has been generally neglected in these calculations.

(ii) Zero-Range Approximation. The radial integral incorporated in the B-factor (Eq. (9)) is, in general, six-dimensional. If it is

assumed that either the range of the internal wave function of the outgoing light particle, or the range of the interaction potential is short enough to be replaced by a delta-function, this integral is reduced to three dimensions with considerably improved calculational facility. In these calculations the latter replacement was used. The extent to which this leads to poorer agreement with experiment is taken as an indication of the importance of finite-range effects.

A substantial effort has been made by a number of workers (e.g., Aus 64, Ros 71, Cha 73) to modify the DWBA formalism to eliminate the need for the zero-range approximation. There is some indication (Nel 70b) that improvement in fits to analyzing power data is possible if finite range effects are included, but it is not obvious that large qualitative changes can be obtained in this way. Therefore, since the program which was available to us did not include finite range effects and because of the emphasis noted above on a simple approach, finite range effects were ignored in these calculations. In view of the generally good fits obtained for the differential cross sections, this procedure seems to have been reasonable.

(iii) Spin-Orbit Distortion in the Exit Channel. The optical potentials used to generate the distorted waves in the program included a spin-orbit distortion potential in the proton channel. In principle, the mass-3 channel ought also to include such a term. However few measurements exist using polarized mass-3 particles from which the magnitude of the spin-orbit strength could be determined. It is believed to be of the order of 2 - 5 MeV (Nel 70b, McE 70). Such a value is

consistent with the rather naive view that the spin-orbit interaction takes place only with the odd nucleon in the light particle, the pair being coupled to zero spin and thus being essentially spectators. This simple picture would require a spin-orbit strength $\sim$ 1/3 that of the proton since the odd nucleon carries one third of the orbital angular momentum of the mass-3 particle.

A survey of the effects of including such a potential was carried out and some typical results are shown in Fig. 6. It is evident that some quantitative but no significant overall qualitative improvement in fits to the analyzing power resulted, and there was no effect on the differential cross section. As a consequence, the mass-3 spin-orbit potential was omitted in the calculations presented here.

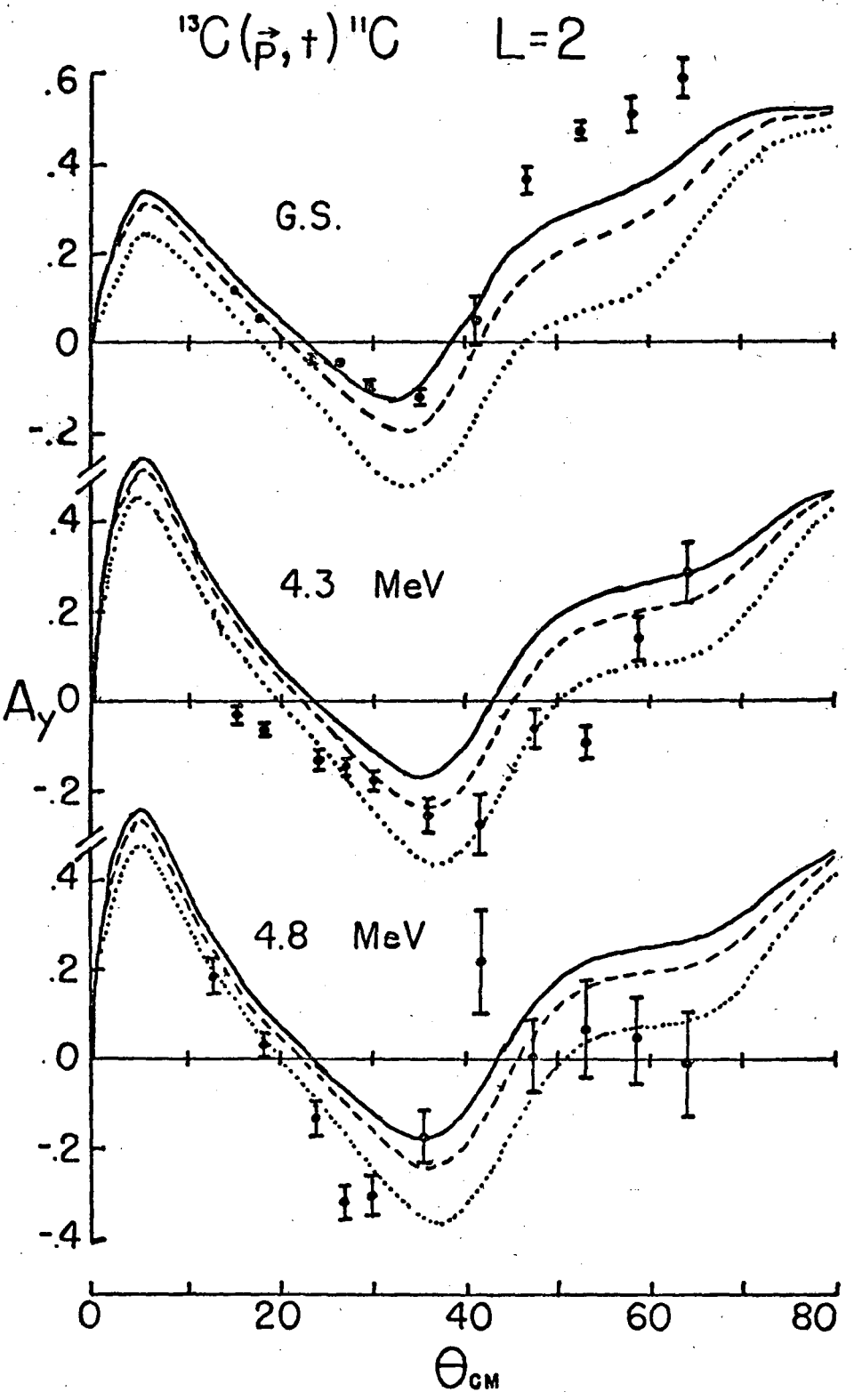


Fig. 6. An example showing the effect of including a spin orbit term in the exit channel optical potential for DWBA. The solid curve results from a calculation without such a potential; the dashed, with $V_{so}$ = 2 MeV; and the dotted, with $V_{so}$ = 6 MeV. See text.

# IV. RESULTS AND DISCUSSION

## A. Transitions in the 1p-Shell

Although the selection rules governing transferred quantum numbers in (p,t) and (p, $^3$He) reactions have been given in Chapter III it is convenient to summarize some salient features at this point in order to introduce a useful notation. Without reproducing the complete selection rules we note that for spin 0 and 1/2 targets, a (p,t) transition is characterized by a single value for the transferred orbital angular momentum L; a (p, $^3$He) transition is characterized by one or more sets of transferred J, L, S, where J and S are the transferred total and spin angular momentum, respectively. As can be seen from Eq. (9), the differential cross section involves a coherent sum over L and S and an incoherent sum over J. We have adopted the following notation for characterizing a complex (p, $^3$He) transition:

$$(J/L/S) = (J_1/L_{11},L_{12}\ldots/S_{11},S_{12},\ldots) \quad ,$$

$$(J_2/L_{21},L_{22},\ldots/S_{21},S_{22},\ldots) \quad , \ \ldots$$

where parentheses indicate a coherent sum over the indicated $L_{ij}$ and $S_{ik}$ to give the $J_i$, and that the cross sections for the $J_i$ are then added incoherently according to Eq. (9). Therefore, as an example:

$(J/L/S) = (2/2/0,1),(3/2/1)$ implies

$$(d\sigma/d\Omega) \propto \sum_{J=2,3} \left| \sum_{\substack{L=2 \\ S=0,1}} \right|^2 \quad .$$

The $(\vec{p},t)$ and $(\vec{p}, {}^3He)$ transitions induced on $^{16}O$, $^{15}N$, and $^{13}C$ targets for which theoretical calculations were undertaken are summarized in Table III. A few additional $(\vec{p}, {}^3He)$ transitions on $^{13}C$, as well as all the transitions observed on the $^7Li$ and $^9Be$ targets are listed in Table IV as cases for which no calculations were attempted. Some results of early analysis of part of these data have been published (Har 70b).

1. $^{16}O(\vec{p},t)$ and $(\vec{p}, {}^3He)$

These reactions have been previously examined with unpolarized beams (Cer 64a, Fle 71), and to some extent with polarized beams (Nel 70a, Nel 70b). Typical spectra from the present work of identified tritons and $^3He$'s showing states in $^{14}O$ and $^{14}N$, respectively, are presented in Fig. 7. Because the target spin is $0^+$, all reactions on this nucleus occur with unique J, and in the case of $(\vec{p},t)$ this implies unique L = J. In $(\vec{p}, {}^3He)$ at most two L-values can contribute (coherently) to the unique J.

Figures 8 and 9 confirm the previously observed and theoretically expected results that the transitions to the analog final states at 0 MeV in $^{14}O$ and at 2.31 MeV in $^{14}N$ have similar angular distributions for both the differential cross sections (Cer 64a) and the analyzing powers (Nel 70a). The DWBA calculations for this pair of transitions yielded excellent fits to the data for both the differential cross sections and the analyzing powers.

The data for the analyzing powers of these two transitions are shown again in Fig. 10, superimposed to emphasize the similarity. Also in this figure are data for three other pairs of analog transitions for which analyzing powers have been measured for the first time. For each

Table III. Summary of Two Nucleon Pick-Up Transitions Compared with DWBA.

| Target $J^\pi$, T | $E_{\vec{p}}$ [a] | $(\vec{p},t)$ Final State (MeV) | $J^\pi$, T [b] | L | $(\vec{p}, {}^3He)$ Final State (MeV) | $J^\pi$, T [b] | (J/L/S) |
|---|---|---|---|---|---|---|---|
| $^{16}O$ $0^+$, 0 | 43.8 | $^{14}O$ | | | $^{14}N$ | | |
| | | g.s. | $0^+$, 1 | 0 | g.s. | $1^+$, 0 | (1/0,2/1) |
| | | 5.17[c] | $(1^-)$, 1 | 1 | 2.31 | $0^+$, 1 | (0/0/0) |
| | | 6.29[c] | $(3^-)$, 1 | 3 | 3.95 | $1^+$, 0 | (1/0,2/1) |
| | | 6.59 | $2^+$, 1 | 2 | 5.11[c] | $2^-$, 0 | (2/1,3/1) |
| | | 7.78 | $2^+$, 1 | 2 | 7.03 | $2^+$, 0 | (2/2/1) |
| | | 9.72 | $(2^+)$, 1 | 2 | 9.17 | $2^+$, 1 | (2/2/0) |
| $^{15}N$ 1/2-, 1/2 | 43.8 | $^{13}N$ | | | $^{13}C$ | | |
| | | g.s. | 1/2-, 1/2 | 0 | g.s. | 1/2-, 1/2 | (0/0/0),(1/0,2/1) |
| | | 3.51 | 3/2-, 1/2 | 2 | 3.68 | 3/2-, 1/2 | (1/0,2/1),(2/2/0,1) |
| | | 7.39 | 5/2-, 1/2 | 2 | 7.55 | 5/2-, 1/2 | (2/2/0,1),(3/2/1) |
| | | 15.07 | 3/2-, 3/2 | 2 | 15.11 | 3/2-, 3/2 | (2/2/0) |
| $^{13}C$ 1/2-, 1/2 | 49.6 | $^{11}C$ | | | $^{11}B$ | | |
| | | g.s. | 3/2-, 1/2 | 2 | g.s. | 3/2-, 1/2 | (1/0,2/1),(2/2/0,1) |
| | | 2.00 | 1/2-, 1/2 | 0 | 2.12 | 1/2-, 1/2 | (0/0/0),(1/0,2/0) |
| | | 4.31 | 5/2-, 1/2 | 2 | 4.44 | 5/2-, 1/2 | (2/2/0,1),(3/2/1) |
| | | 4.79 | 3/2-, 1/2 | 2 | 5.02 | 3/2-, 1/2 | (1/0,2/1),(2/2/0,1) |
| | | 6.48 | 7/2-, 1/2 | d | 6.74 | 7/2-, 1/2 | (3/2/1) |
| | | 12.47 | 1/2-, 3/2 | 0 | 12.94 | 1/2-, 3/2 | (0/0/0) |

(continued)

Table III. (continued)

[a] $E_{\vec{p}}$ is the beam energy in MeV.

[b] $J^{\pi}$, T assignments and excitation energies are from (Ajz 68, Ajz 70) except for the $^{16}O$ 9.72 MeV state from (Fle 71) and the T = 3/2 analog states in mass 11 from (Cos 68).

[c] Two nucleon cfp's were not available for these negative parity states in (Coh 70). Shell model configurations were based on (Tru 63) as follows

$$|^{14}O^{*}\ (5.17),\ 1^{-}\rangle = |[p_{1/2}\ s_{1/2}]_{1^{-}}\rangle$$

$$|^{14}O^{*}\ (6.29),\ 3^{-}\rangle = |[p_{1/2}\ d_{5/2}]_{3^{-}}\rangle$$

$$|^{14}N^{*}\ (5.11),\ 2^{-}\rangle = |[p_{1/2}\ d_{5/2}]_{2^{-}}\rangle \quad .$$

[d] This transition is L-forbidden. See text.

Table IV. Data Summary - No DWBA Calculations Performed.

| A. ($E_p$ = 49.6 MeV) | Target $J^\pi$, T | Reaction | $E_x$ (MeV) | $J^\pi$, $T^a$ |
|---|---|---|---|---|
| | $^{13}C$ (1/2-, 1/2) | $(\vec{p}, {}^3He)$ $^{11}B$ | 8.57 | < 5/2-, 1/2 |
| | | | 8.93 | 5/2-, 1/2 |
| | | | 11.60 | (1/2-, 3/2-), 1/2 |

B. ($E_{\vec{p}}$ = 43.7 MeV)

| Target | 2S + $l_{L_J}$, T | (p,t) $E_x$ (MeV) | 2S + $l_{L_J}$, $T^b$ | L | Residual Nucleus $E_x$ (MeV) | (p, $^3$He) 2S + $l_{L_J}$, $T^b$ | (J/L/S) |
|---|---|---|---|---|---|---|---|
| $^9$Be | $^2P_{3/2}$, 1/2 | g.s. | $^2P_{3/2}$, 1/2 | 0,2 | g.s. | $^2P_{3/2}$, 1/2 | (0/0/0),(1/0,2/1),(2/2/0,1),(3/2/1) |
| | | 0.431 | $^2P_{1/2}$, 1/2 | 0 | 0.478 | $^2P_{1/2}$, 1/2 | (0/0/0),(1/0,2/1) |
| | | 4.55 | $^2F_{7/2}$, 1/2 | 2,4 | 4.63 | $^2F_{7/2}$, 1/2 | (2/2/0,1),(3/2/1),(4/4/0,1) |
| | | 6.5 | $^2F_{5/2}$, 1/2 | 2,4 | 7.48 | $^4P_{5/2}$, 1/2 | (1/0,2/1),(2/2/0,1),(3/2/1) |
| | | 10.79 | $^2P_{5/2}$, 3/2 | 0,(2) | 11.13 | $^2P_{3/2}$, 3/2 | (0/0/0),(2/2/0) |
| $^7$Li | $^2P_{3/2}$, 1/2 | g.s. | $^2P_{3/2}$, 1/2 | 0,2 | g.s. | $^2P_{3/2}$, 1/2 | (0/0/0),(1/0,2/1),(2/2/0,1),(3/2/1) |

[a] $J^\pi$, T assignments and excitation energy from (Ajz 68), (Fle 67).

[b] 2S + $l_{L_J}$, T assignments and excitation energy from (Lau 66), (Cer 66), (McG 67).

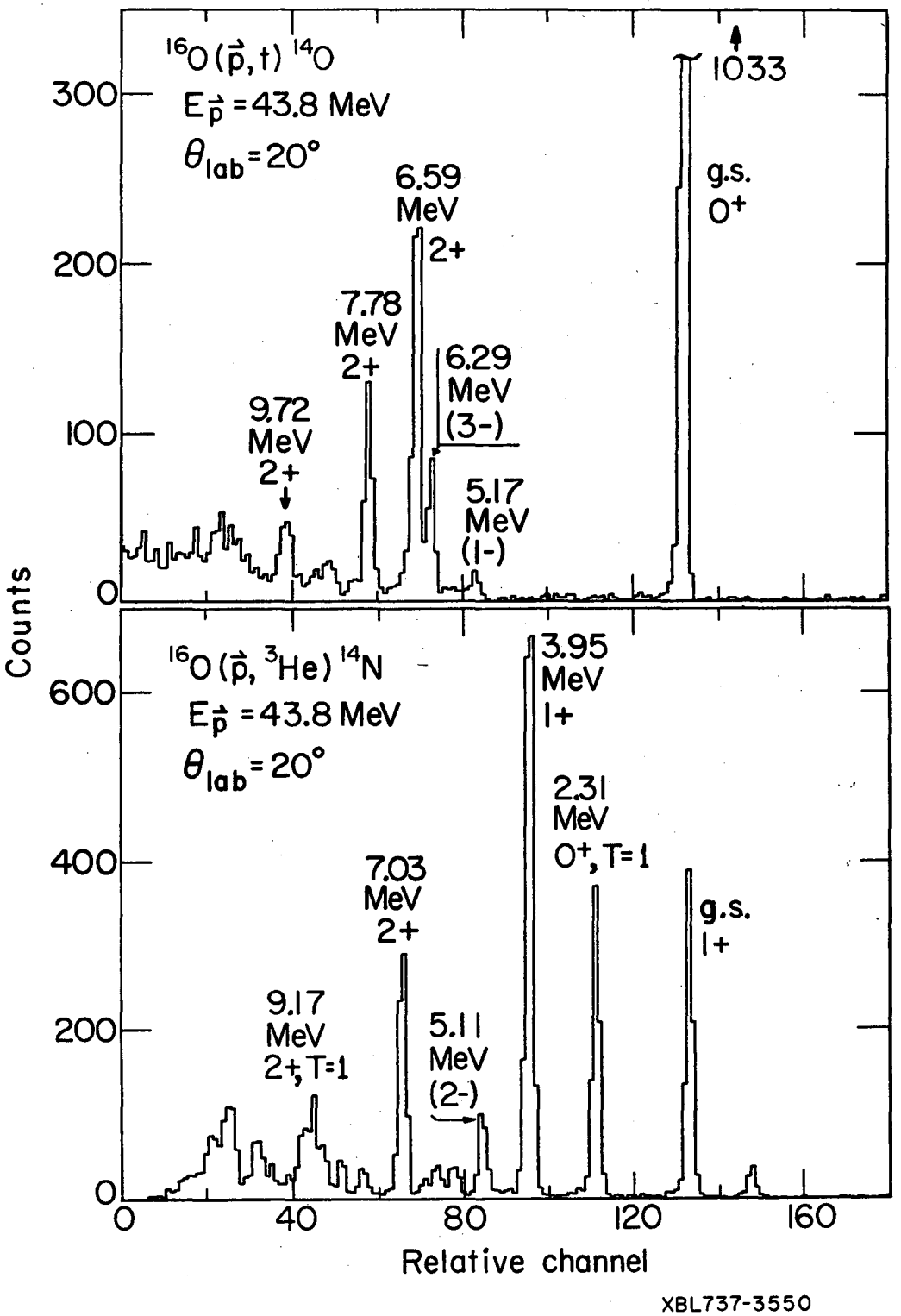


Fig. 7. Energy Spectra for the $^{16}O(\vec{p},t)\,^{14}O$ and $^{16}O(\vec{p},\,^{3}He)\,^{14}N$ reactions.

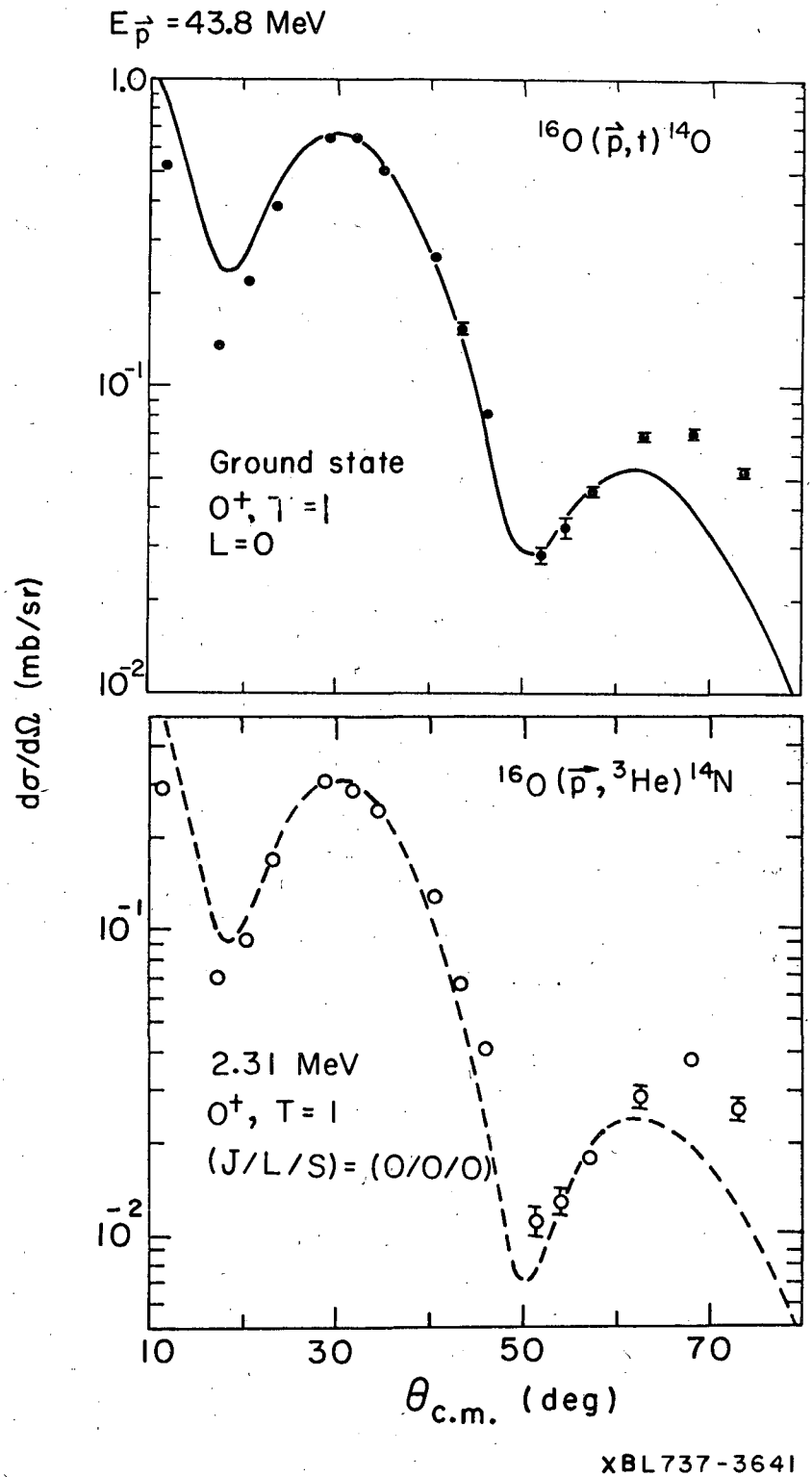


Fig. 8. Differential cross section angular distribution for the (p,t) and (p, $^3$He) transitions to the $0^+$, T = 1 analog states at 0 MeV in $^{14}$O and 2.31 MeV in $^{14}$N. The curves are DWBA calculations described in the text and normalized separately to the data. See also Fig. 9.

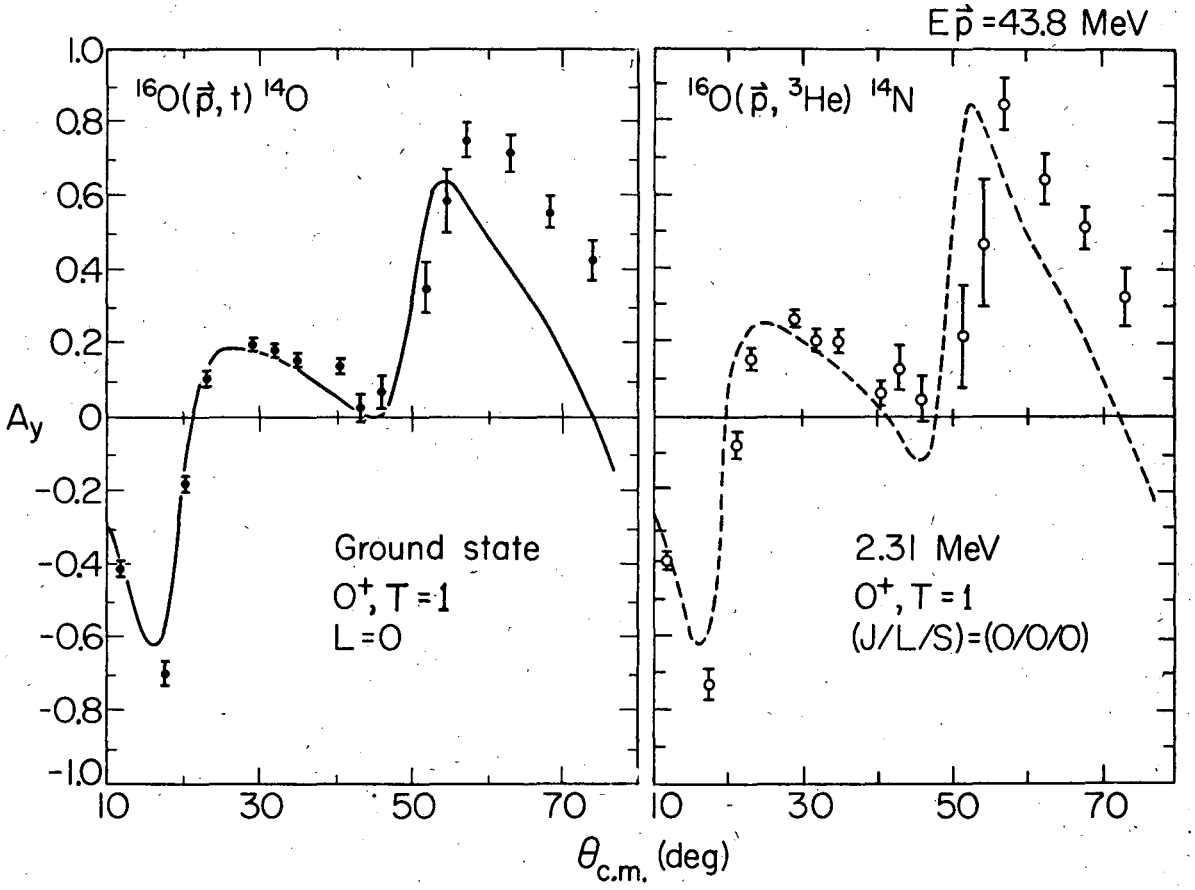


Fig. 9. Analyzing power angular distributions for the transitions described in the caption to Fig. 8. The curves are DWBA calculations described in the text.

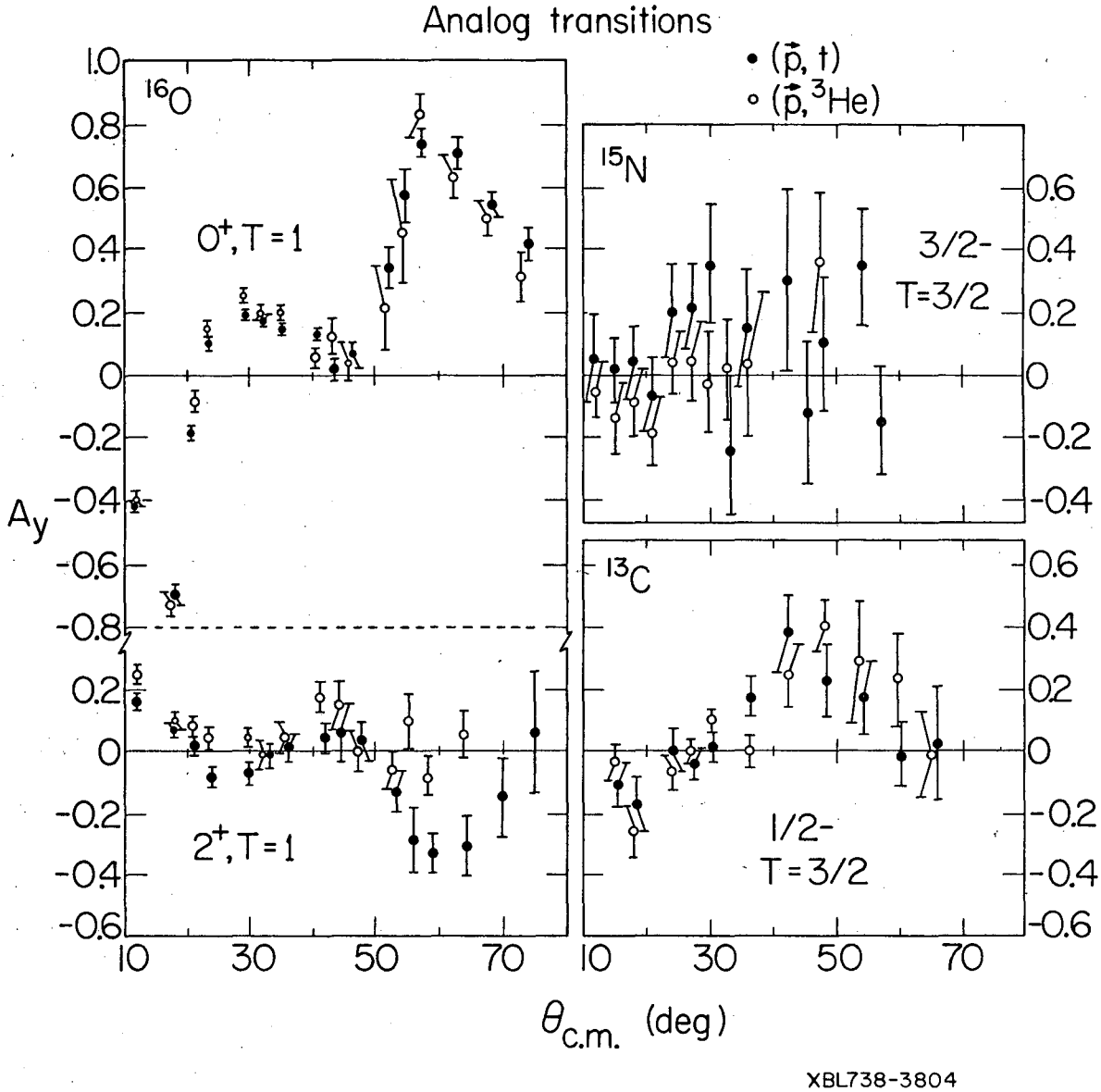


Fig. 10. Data for the analyzing powers of the four pairs of analog transitions observed in this work. Each pair is identified by the target and the final state $J^{\pi}$, T.

pair, the expected similarity is evident, although it is considerably less striking than in the case noted above, particularly for the transitions to the $2^+$, T = 1 states in mass-14 at back angles. Nevertheless, in view of the weakness of these latter transitions, the agreement is satisfactory. Each of these transitions will be discussed further later in the context of the other transitions leading to the particular residual nucleus.

Figures 11 and 14 summarize the differential cross sections (to be denoted $d\sigma/d\Omega$) and the analyzing powers ($A_y$) for transitions to several final states in $^{16}O(\vec{p},t)^{14}O$. Good agreement between the theoretical and experimental differential cross sections are evident in Fig. 11 for the L = 2 transitions to states in $^{14}O$ at 6.59, 7.78, and 9.72 MeV. The analyzing powers for the same three transitions are shown in Fig. 12. While the theory predicts similar shapes for all three, the data indicate that the 6.59 MeV transition strongly disagrees with this prediction and moreover, differs experimentally from the other two transitions which agree rather well with the theory. The data for the weakly populated 9.72 MeV state are somewhat inconclusive because of their large error bars.

The weak transitions to the negative parity states at 5.17 MeV (1-) and 6.29 MeV (3-), are summarized in Figs. 13 and 14. Although agreement in the differential cross section is obtained at forward angles for the 5.17 MeV L = 1 transition, the transition to the 6.29 MeV state which has been assigned (3-), is out of phase with the L = 3 calculation and shows a somewhat greater similarity to the L = 2 transitions shown in Fig. 11. This is in accord with the findings of Fleming et al. (Fle 71) who

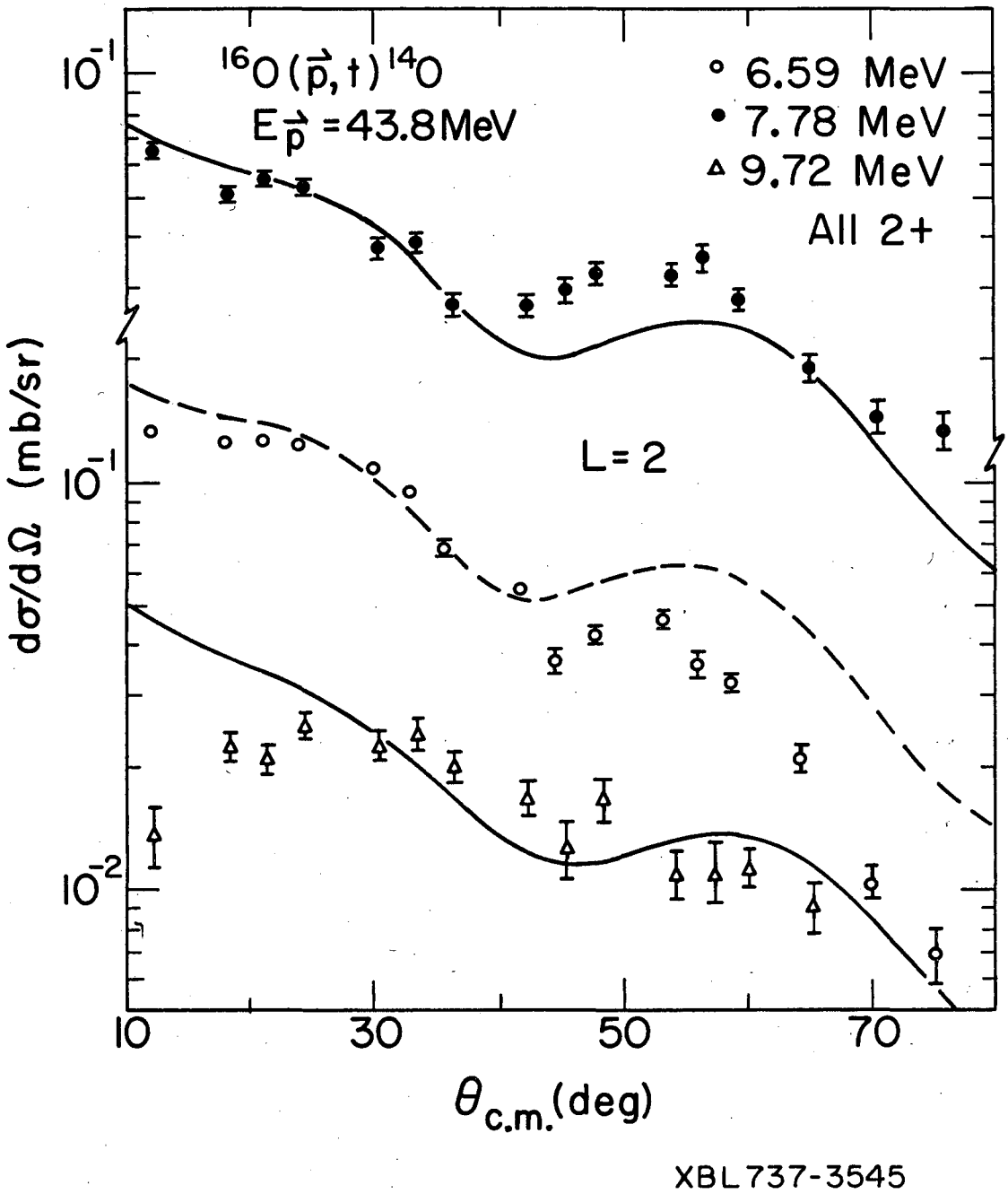


Fig. 11. Differential cross sections for L = 2 $^{16}O(\vec{p},t)^{14}O$ transitions. The curves are DWBA calculations described in the text and normalized separately to the data. See also Fig. 12.

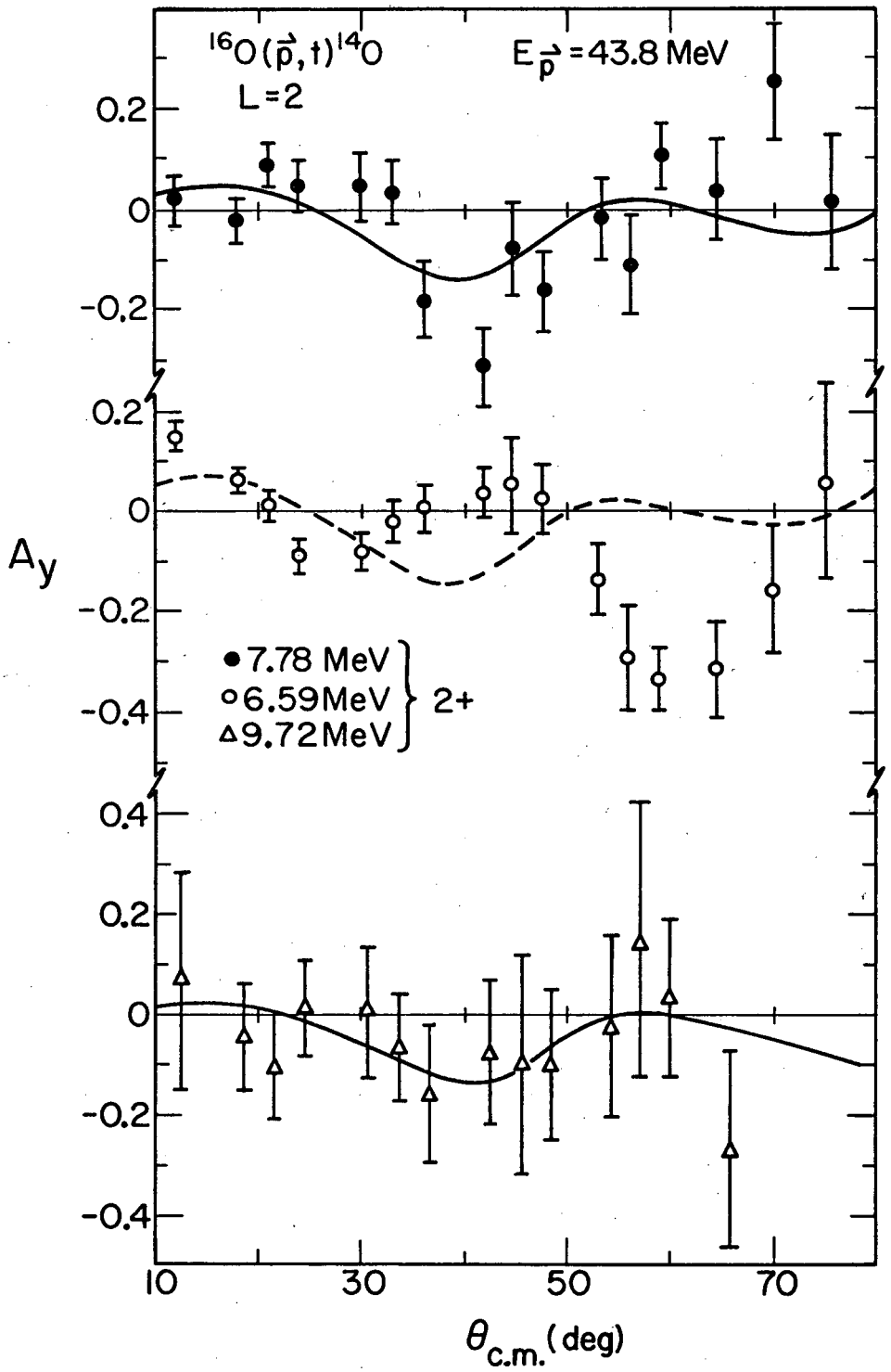


Fig. 12. Analyzing powers corresponding to the differential cross sections in Fig. 11. The curves are DWBA calculations described in the text.

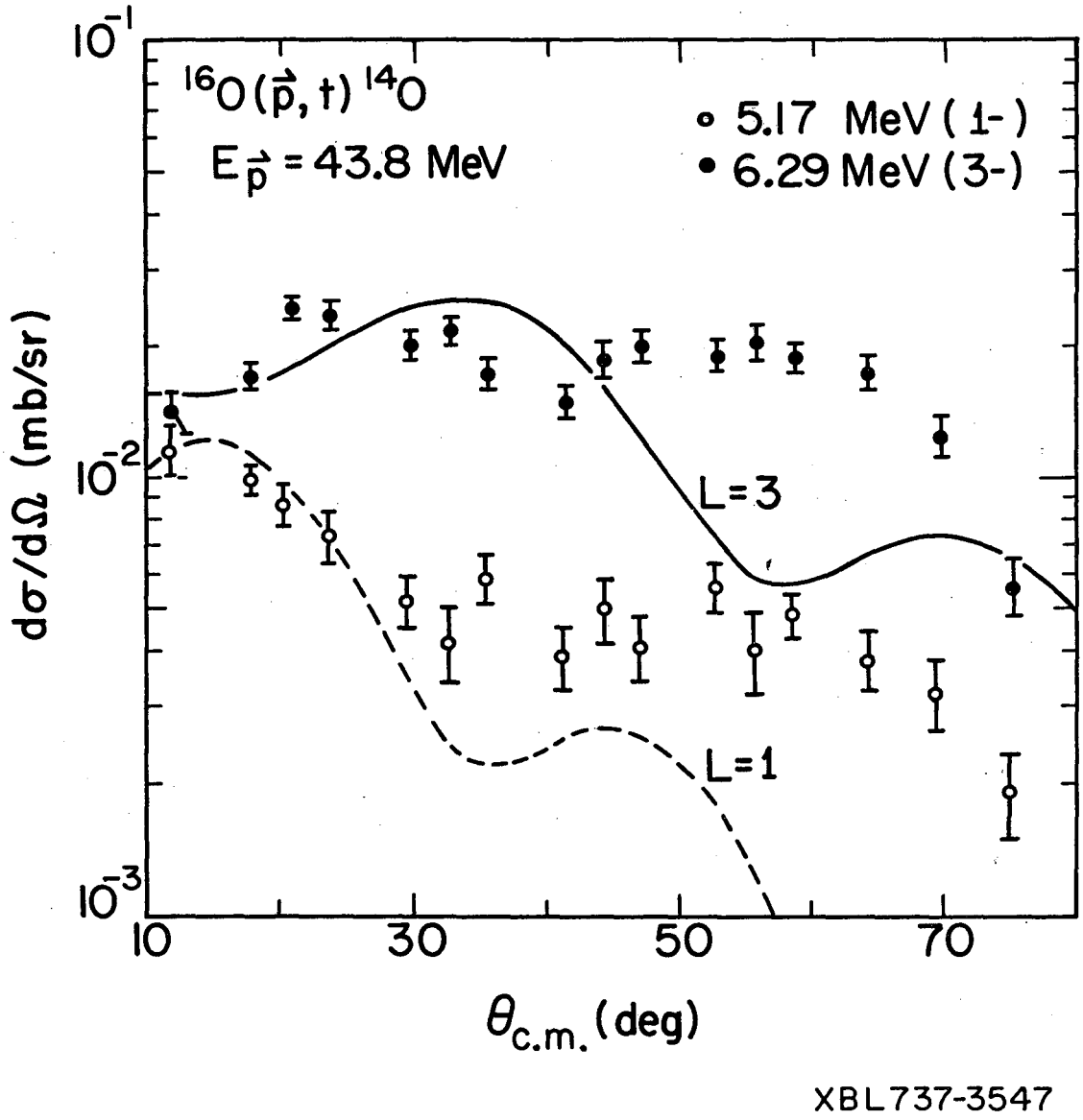


Fig. 13. Differential cross sections for the $(\vec{p},t)$ transitions to negative parity states in $^{14}O$. The curves are DWBA calculations described in the text and normalized separately to the data. See also Fig. 14.

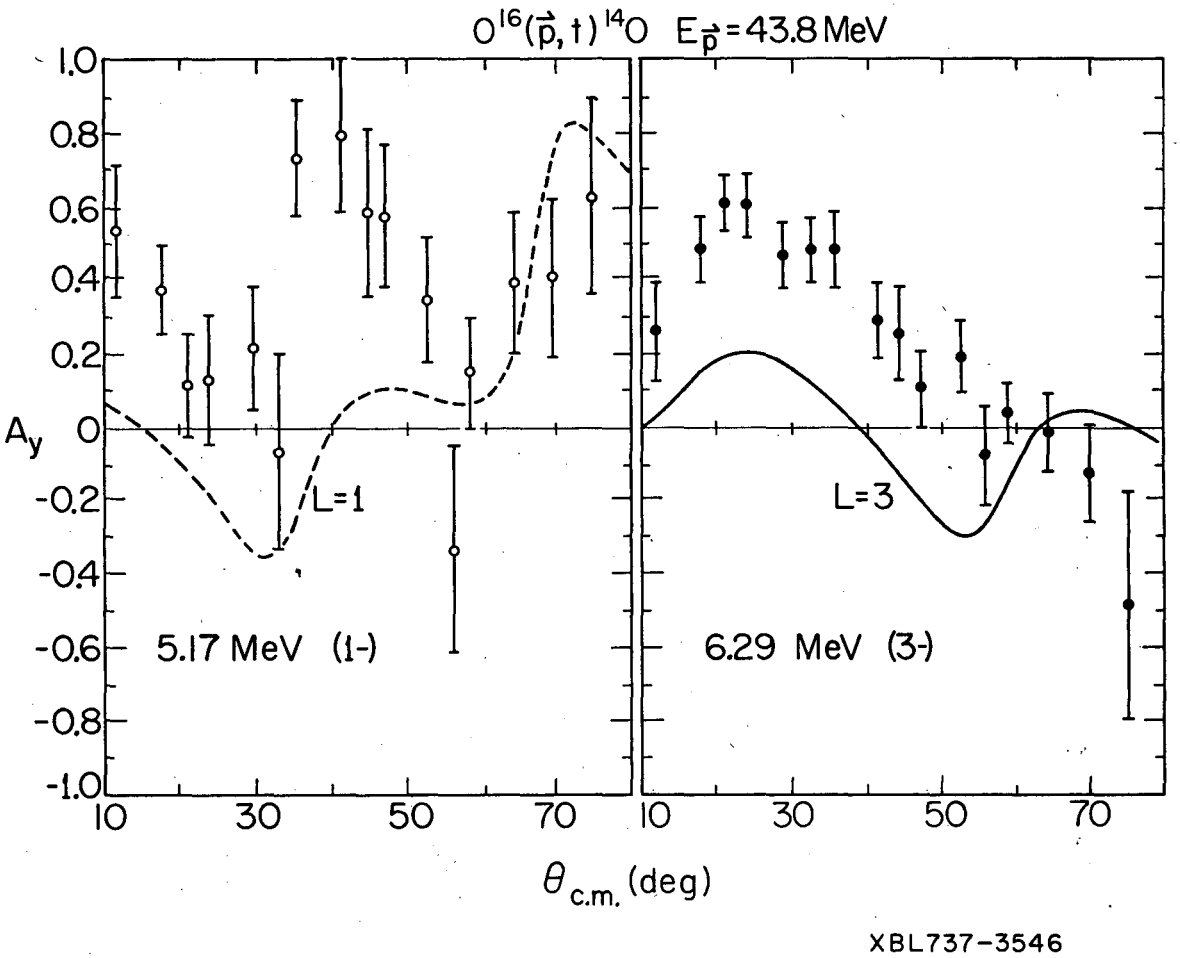


Fig. 14. Analyzing powers for the transitions described in the caption to Fig. 13. The curves show DWBA calculations described in the text.

concluded that an unambiguous L transfer assignment to this transition could not be made on the basis of these data.

For the analyzing powers of these transitions to odd spin states (Fig. 14) no agreement for either case is evident. Although no L = 2 prediction is shown for the 6.29 MeV transition, the data bear no similarity to the typical L = 2 shape shown for the three states in Fig. 12. The analyzing power, therefore, does not further elucidate the L transfer involved in this transition.

The $^{16}O(\vec{p}, {}^{3}He)^{14}N$ results are shown in Figs. 15-18. Of particular interest are the $1^+$ states in $^{14}N$ at 0 and 3.95 MeV shown in Figs. 15 and 16. Both transitions can go by L = 0 and 2 but the cfp's of Cohen and Kurath (Coh 70) indicate predominant L = 2 to the ground state and L = 0 to the 3.95 MeV state; the data in Fig. 15 for $d\sigma/d\Omega$ support this prediction, although the agreement is only qualitative for the 3.95 MeV transition. However there is no agreement whatsoever for the $A_y$ in either case as shown in Fig. 16, which is particularly surprising for the ground state whose $d\sigma/d\Omega$ is well fit. It is interesting to note that the predominantly L = 0 theoretical fit to $A_y$ for the 3.95 MeV $1^+$ state would give a better (but still qualitative) fit to the $1^+$ ground state transition $A_y$. In an effort to vary the details of the wave functions to determine the magnitude of the effect on $A_y$, calculations were carried out using structure factors corresponding to a pure jj configuration:[4] No major changes resulted and it is not clear that the simple DWBA is capable of resolving this discrepancy.

The remaining three $^{16}O(\vec{p}, {}^{3}He)^{14}N$ transitions are shown in Figs. 17 and 18. The 5.11 MeV (2-) state can be populated by L = 1 or 3.

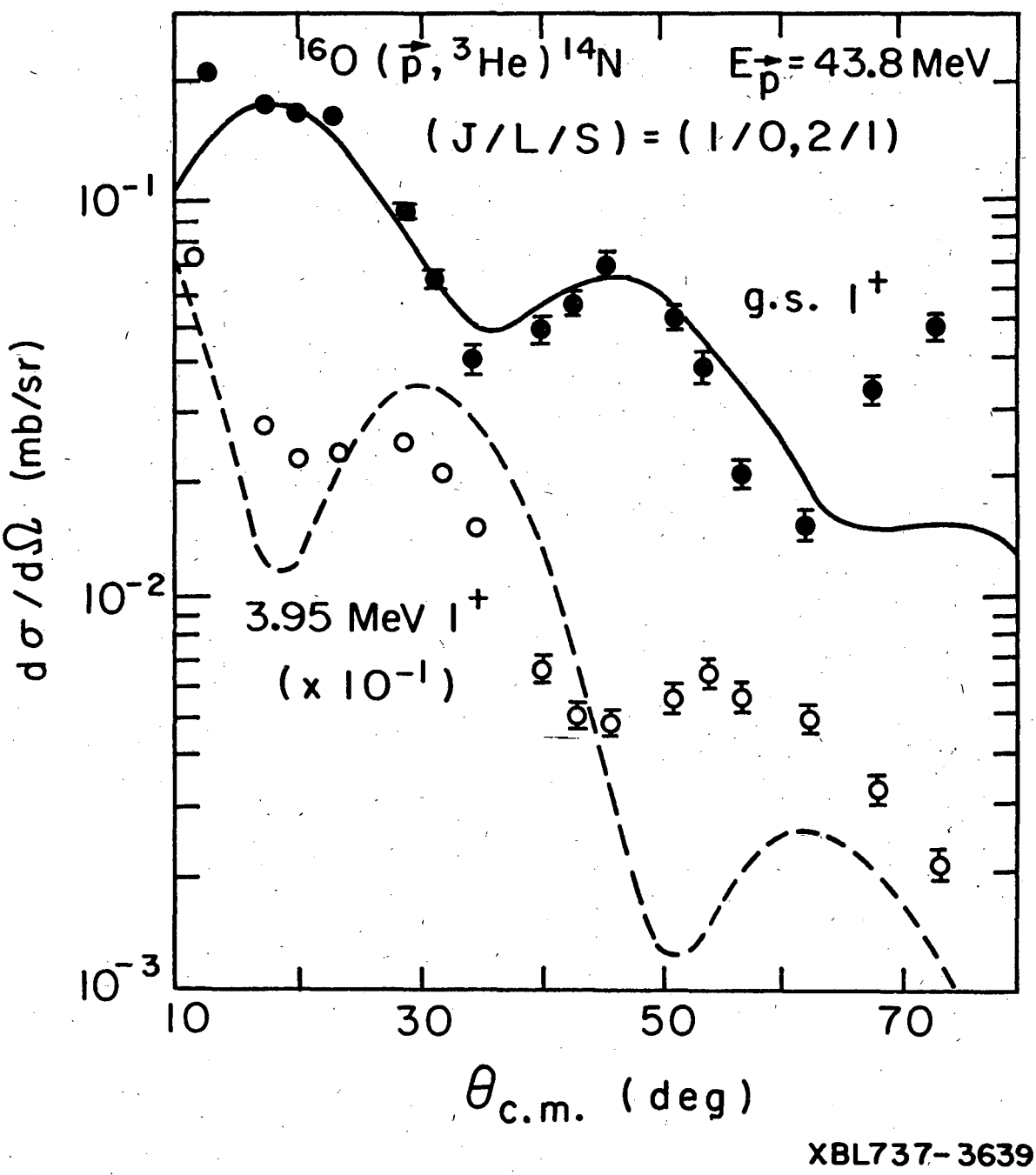


Fig. 15. Differential cross sections for the $^{16}O(\vec{p}, {}^3He)^{14}N$ transitions to the ground and 3.95 MeV states (1+) indicating the transferred (J/L/S) as explained in the text. DWBA calculations described in the text are shown by the curves and are normalized separately to the data. See also Fig. 16.

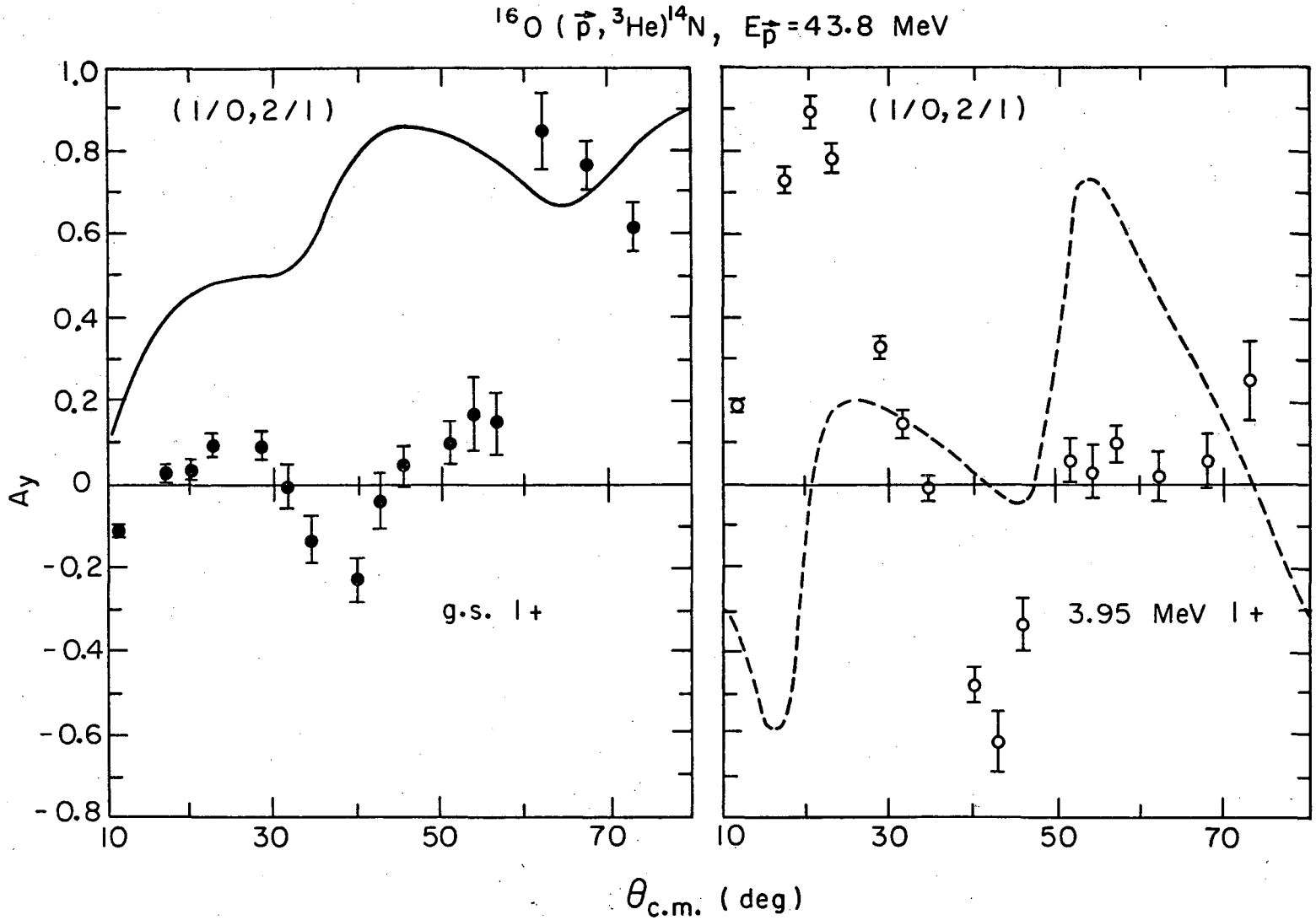


XBL737-3640

Fig. 16. Analyzing powers for the transitions described in the caption to Fig. 15. The curves show DWBA fits described in the text.

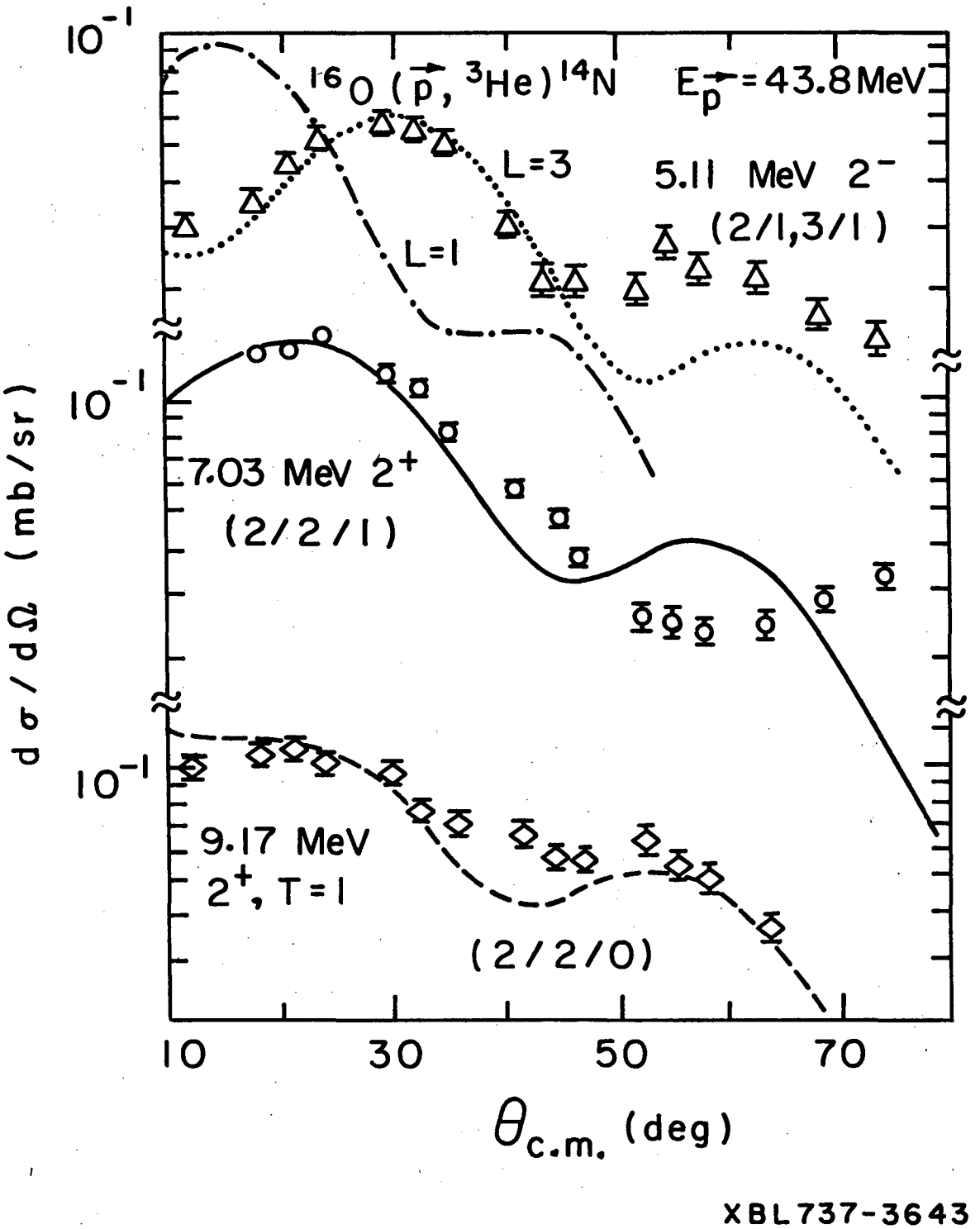


Fig. 17. Differential cross sections for $^{16}O(\vec{p}, {}^3He)$ to final states in $^{14}N$ indicating the transferred (J/L/S) as explained in the text. The curves are DWBA calculations described in the text and normalized separately to the data. See also Fig. 18.

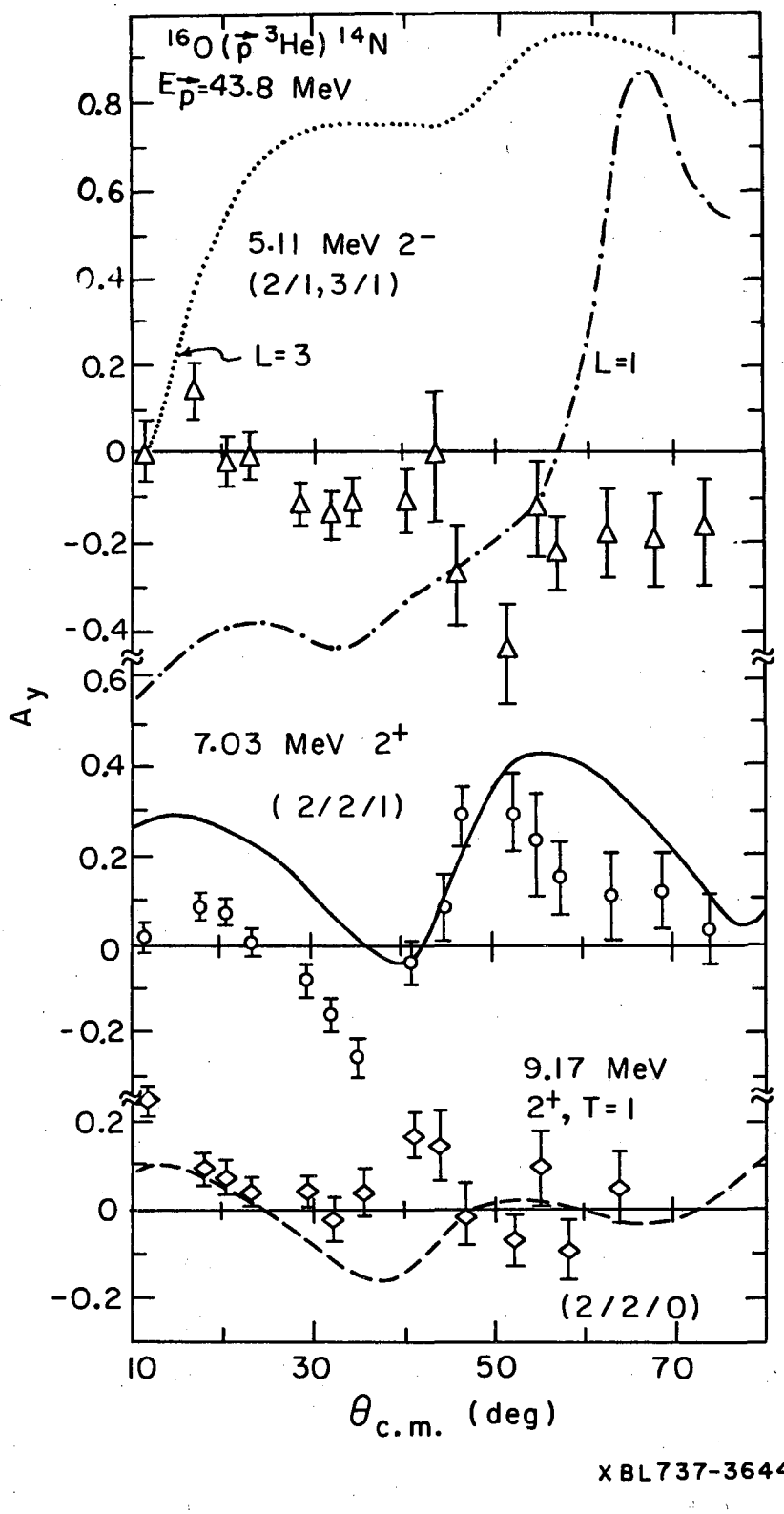


Fig. 18. Analyzing powers for the transitions shown in Fig. 17. The curves are DWBA calculations described in the text.

Since cfp's were not available for this transition, separate calculations for the two allowed L-transfers are shown. The $d\sigma/d\Omega$ (Fig. 17) clearly indicates dominant L = 3 characteristics but in Fig. 18 no agreement for either L = 1 or 3 in the $A_y$ is apparent.

The $2^+$ states at 7.03 and 9.17 MeV are T = 0 and T = 1, respectively, the latter being the analog of the 6.59 MeV $2^+$ state in $^{14}O$. Figure 17 shows rather good DWBA agreement with the experimental $d\sigma/d\Omega$ for both of these, although primarily at forward angles for the T = 0 state. The calculated $A_y$ for the T = 0 state in Fig. 18 is also in reasonable qualitative agreement with the data. Comparison of the $A_y$ for the T = 1 state with that of its analog in Fig. 10 shows a clear experimental similarity. However, the disagreement with the theory shown earlier in Fig. 12 for the $(\vec{p},t)$ case at 6.59 MeV in $^{14}O$ persists also for the $(\vec{p}, {}^3He)$ analog at 9.17 MeV in $^{14}N$ shown in Fig. 18.

2. $^{15}N(\vec{p},t)$ and $(\vec{p}, {}^3He)$

These reactions have been previously investigated using unpolarized beams (Fle 68a, Fle 68b). Figure 19 shows examples of $^{13}N$ and $^{13}C$ spectra obtained from the $^{15}N$ target. In this case, the corresponding $(\vec{p},t)$ and $(\vec{p}, {}^3He)$ reactions yield pairs of mirror states in the final nuclei, as well as T = 3/2 analogs at $\sim$ 15 MeV. Since the spin of the target is 1/2-, the selection rules permit up to four combinations of transferred (J/L/S) for the $(\vec{p}, {}^3He)$ case as indicated in Table III, although the $(\vec{p},t)$ transitions remain unique.

The $d\sigma/d\Omega$ and $A_y$ for the L = 0 ground state (p,t) transition are shown in Figs. 20 and 21, and bear strong experimental resemblance to the

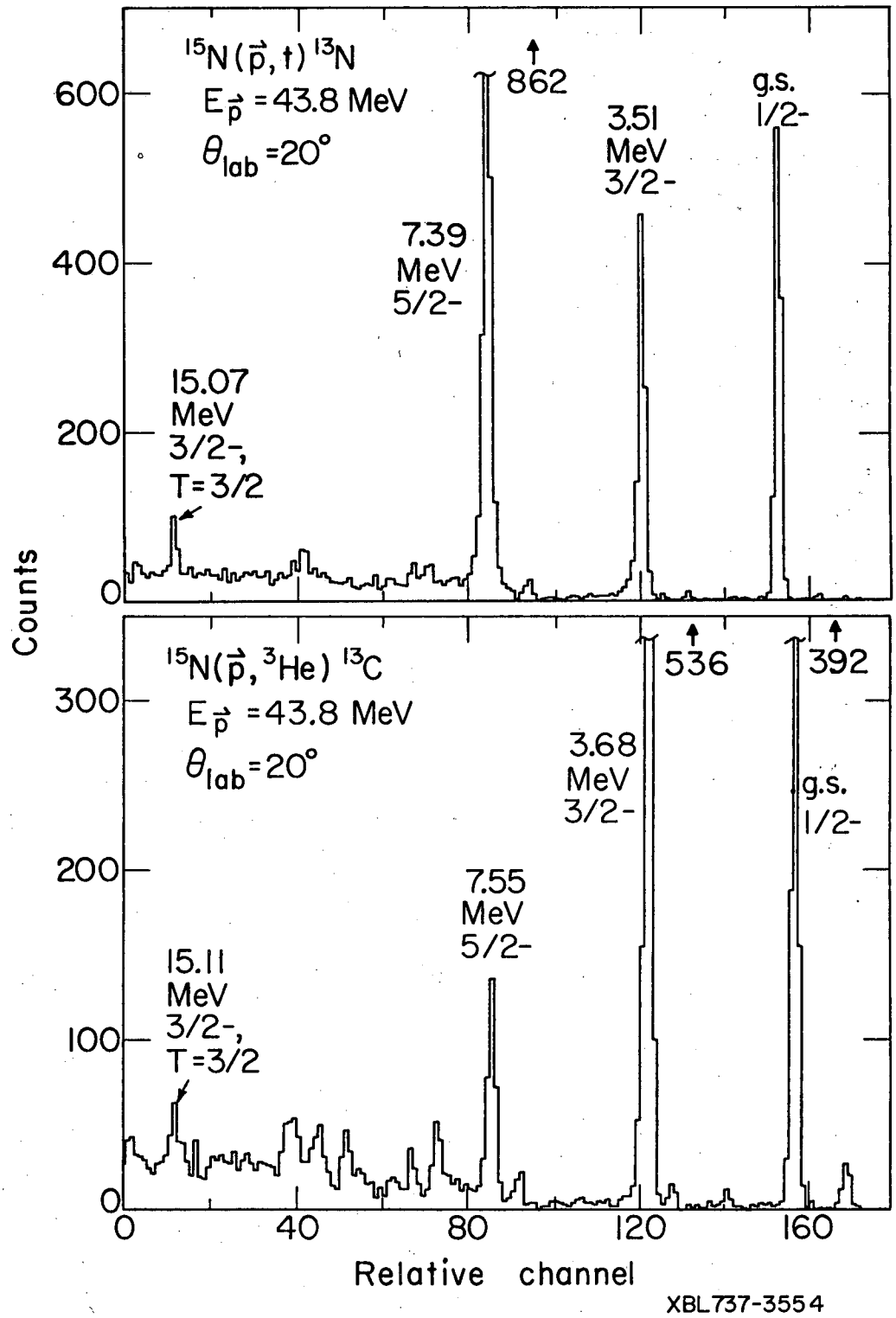


Fig. 19. Energy spectra for the $^{15}N(\vec{p},t)^{13}N$ and $^{15}N(\vec{p},\ ^3He)^{13}C$ reactions.

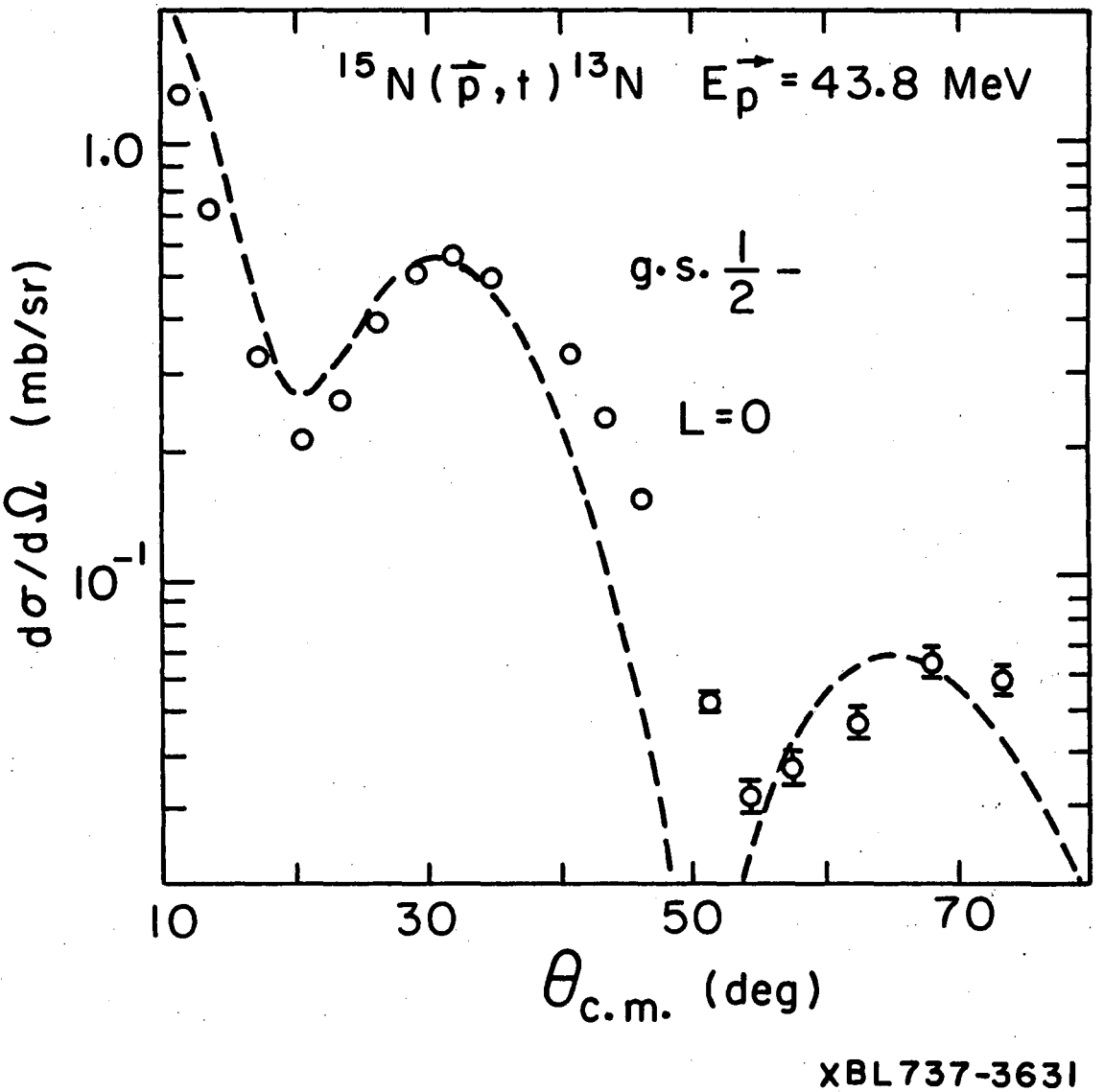


Fig. 20. Differential cross section for the $^{15}N(\vec{p},t)^{13}N$ (ground state) reaction. The curve is a DWBA calculation described in the text.

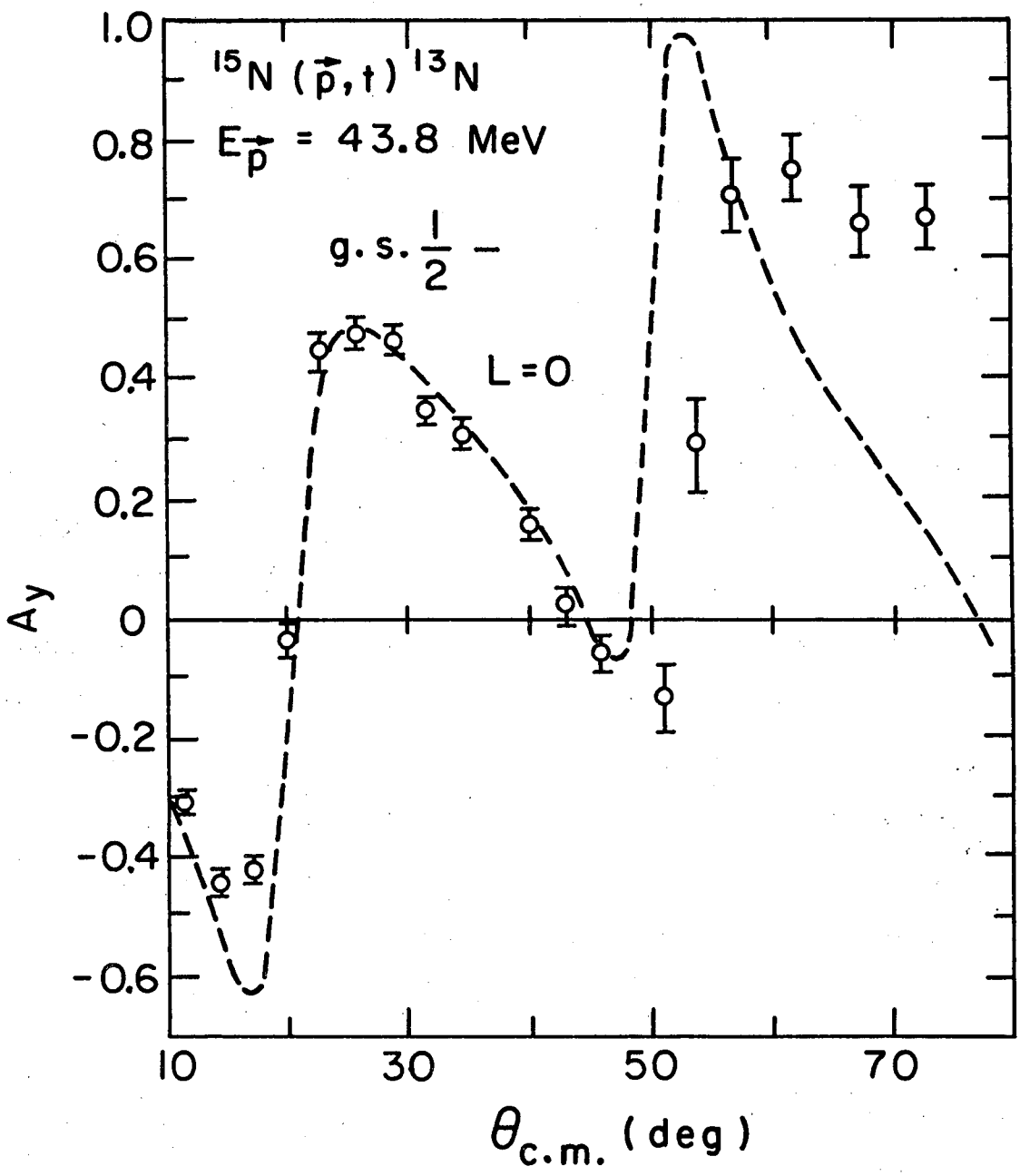


XBL737-3632

Fig. 21. The analyzing power for the $^{15}N(\vec{p},t)^{13}N$ ground state transition shown in Fig. 20. The curve is a DWBA calculation described in the text.

L = 0 analog transitions induced on $^{16}O$ (Figs. 8 and 9). Furthermore, very good DWBA agreement was obtained, as was the case for the reactions on $^{16}O$.

Three L = 2 $(\vec{p},t)$ results are shown in Figs. 22 and 23. All three transitions have similar $d\sigma/d\Omega$ shapes and are all fit well by the DWBA, particularly at forward angles. The theory predicts similar $A_y$ angular distributions also, but, the data indicate no such uniformity. The $A_y$ for the transition to the 3.51 MeV state agrees very poorly, while that to the 7.39 MeV state is fit rather well. The large error bars for the transition to the 15.07 MeV T = 3/2 state in Fig. 23 make the comparison of theoretical and experimental $A_y$'s inconclusive, although it appears the agreement is not good.

In Chapter III mention was made of the role of spin dependence in the interaction and its effect on the ratio of S = 0 and S = 1 transition amplitudes. Whether the enhancement of S = 0, which has been determined from other work (Fle 68a, Fle 71), has a major effect on the calculated analyzing power or not was examined for a number of $(\vec{p}, {}^3He)$ transitions on the $^{15}N$ target. The enhancement, which is of the order of a factor of three, was included by multiplying the structure factors pertaining to S = 0 terms in the cross section by $\sqrt{3}$. The results of this examination will be shown in the below Figs. 24 through 27 by the dashed curves, while the calculations with no S = 0 enhancement are given by solid curves. It will be seen that minor details are affected, but that no substantial changes in the qualitative predictions occur, nor does the inclusion of this effect bring improvement to the quality of the fits.

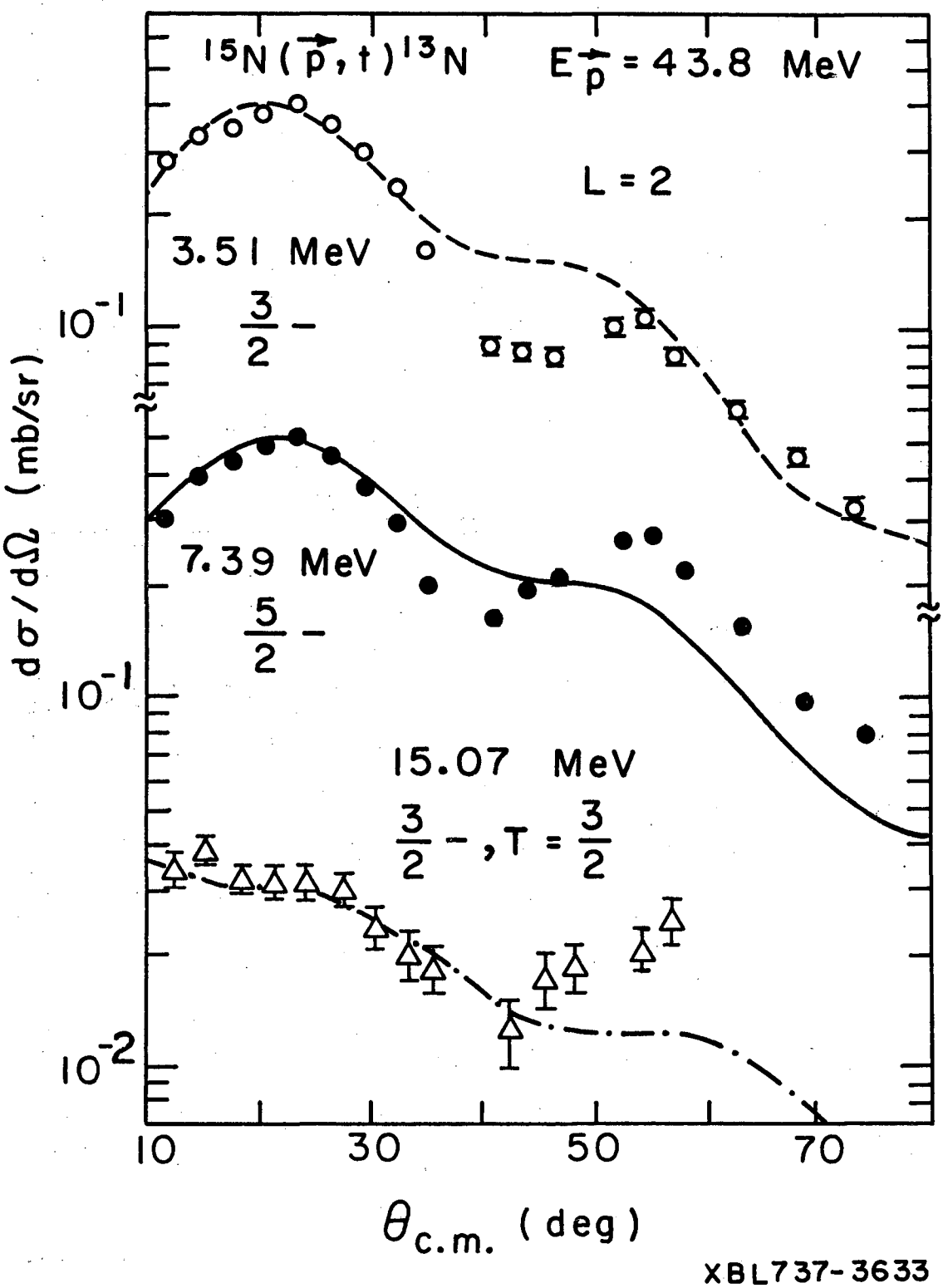


Fig. 22. Differential cross sections for L = 2 $^{15}N(\vec{p},t)^{13}N$ transitions. The curves are DWBA calculations described in the text and normalized separately to the data. See also Fig. 23.

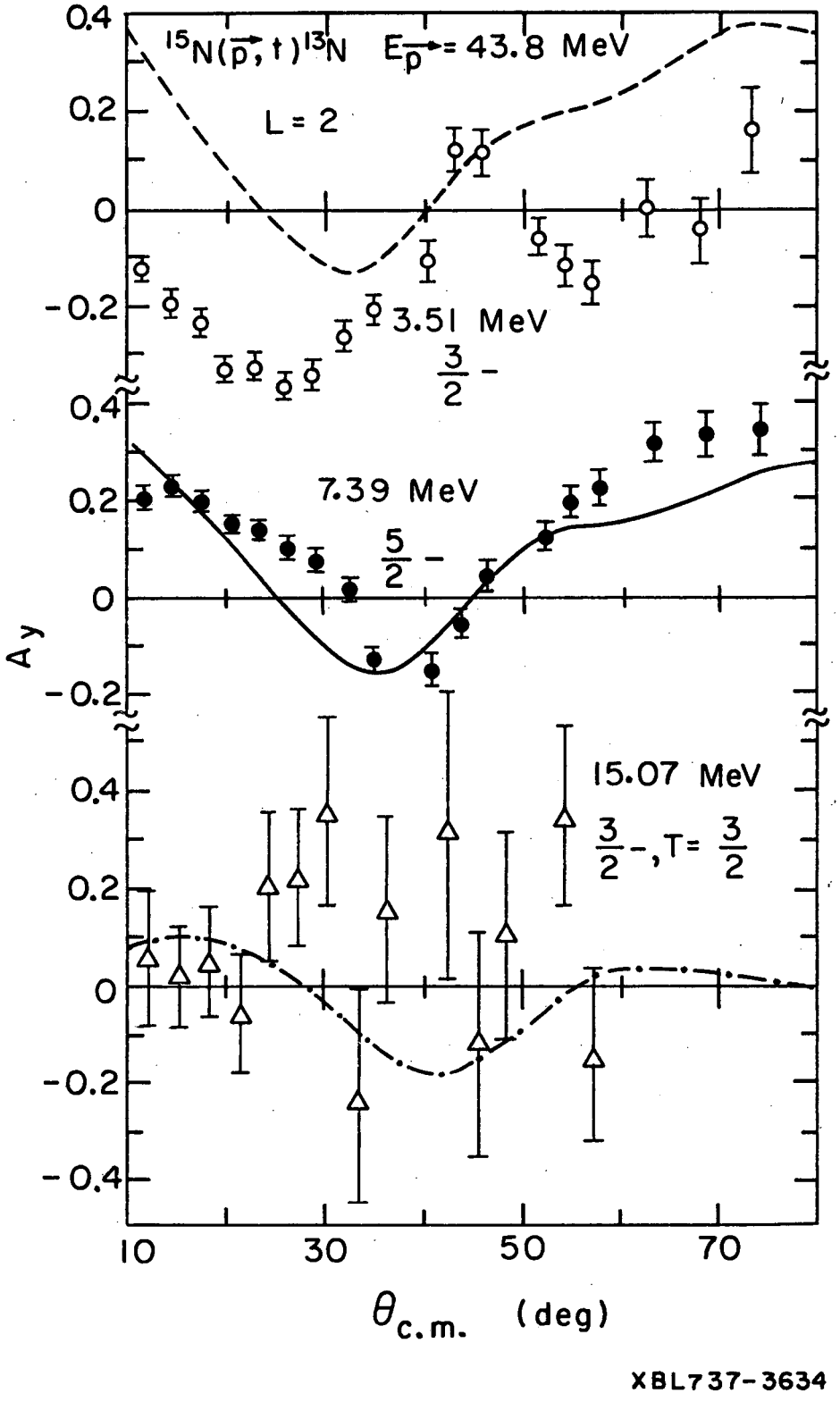


Fig. 23. Analyzing powers corresponding to the L = 2 transitions shown in Fig. 22. The DWBA calculations described in the text are shown by the curves.

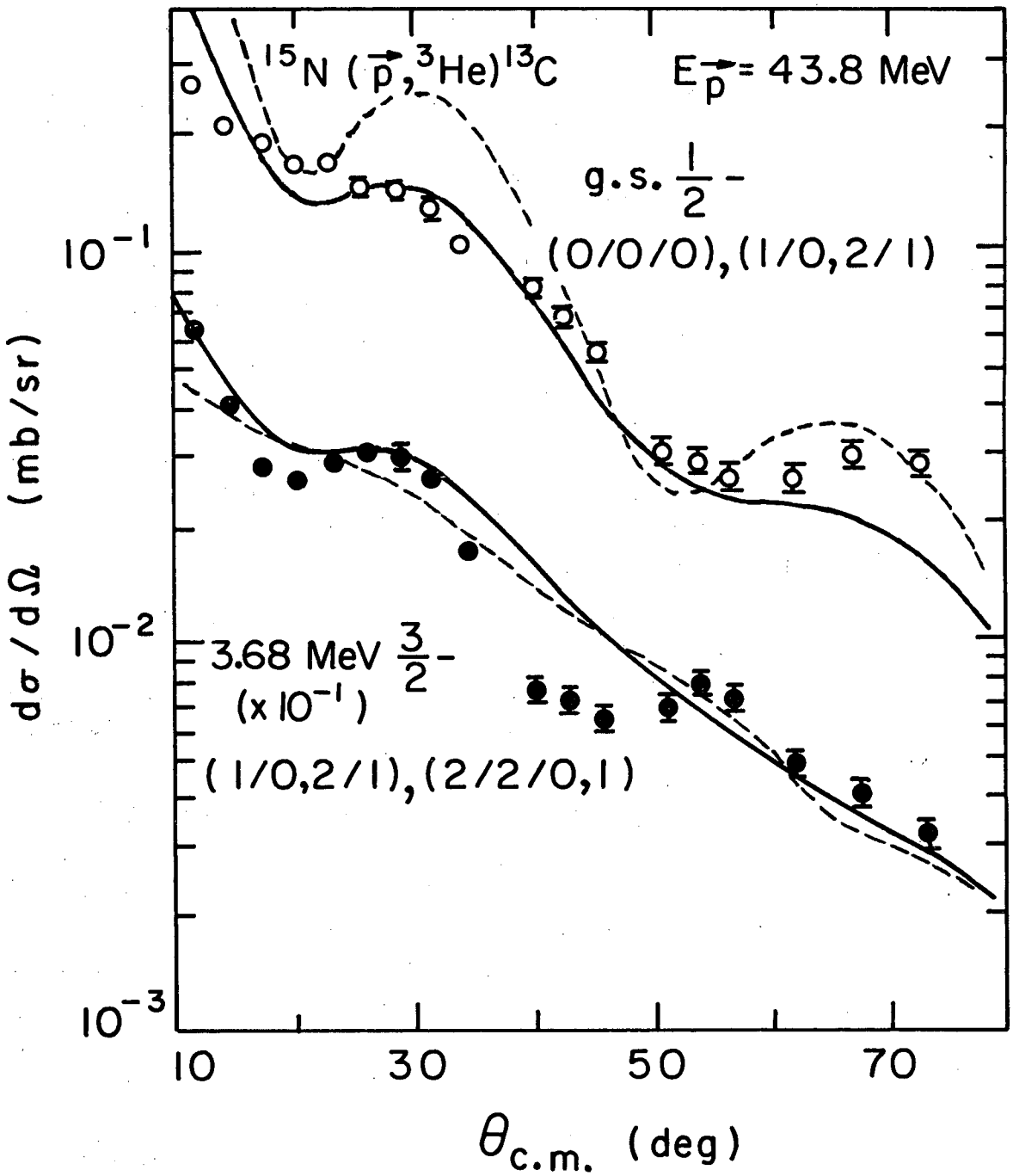


XBL737-3635A

Fig. 24. Differential cross sections for two $^{15}N(\vec{p}, {}^{3}He)^{13}C$ transitions to the ground and 3.68 MeV states, labeled by $J^{\pi}$ and transferred (J/L/S) as explained in the text. The curves are DWBA calculations normalized separately to the data. The solid curve results from neglecting spin dependence, while the dashed curve is obtained by including spin dependence. See text and also Fig. 25.

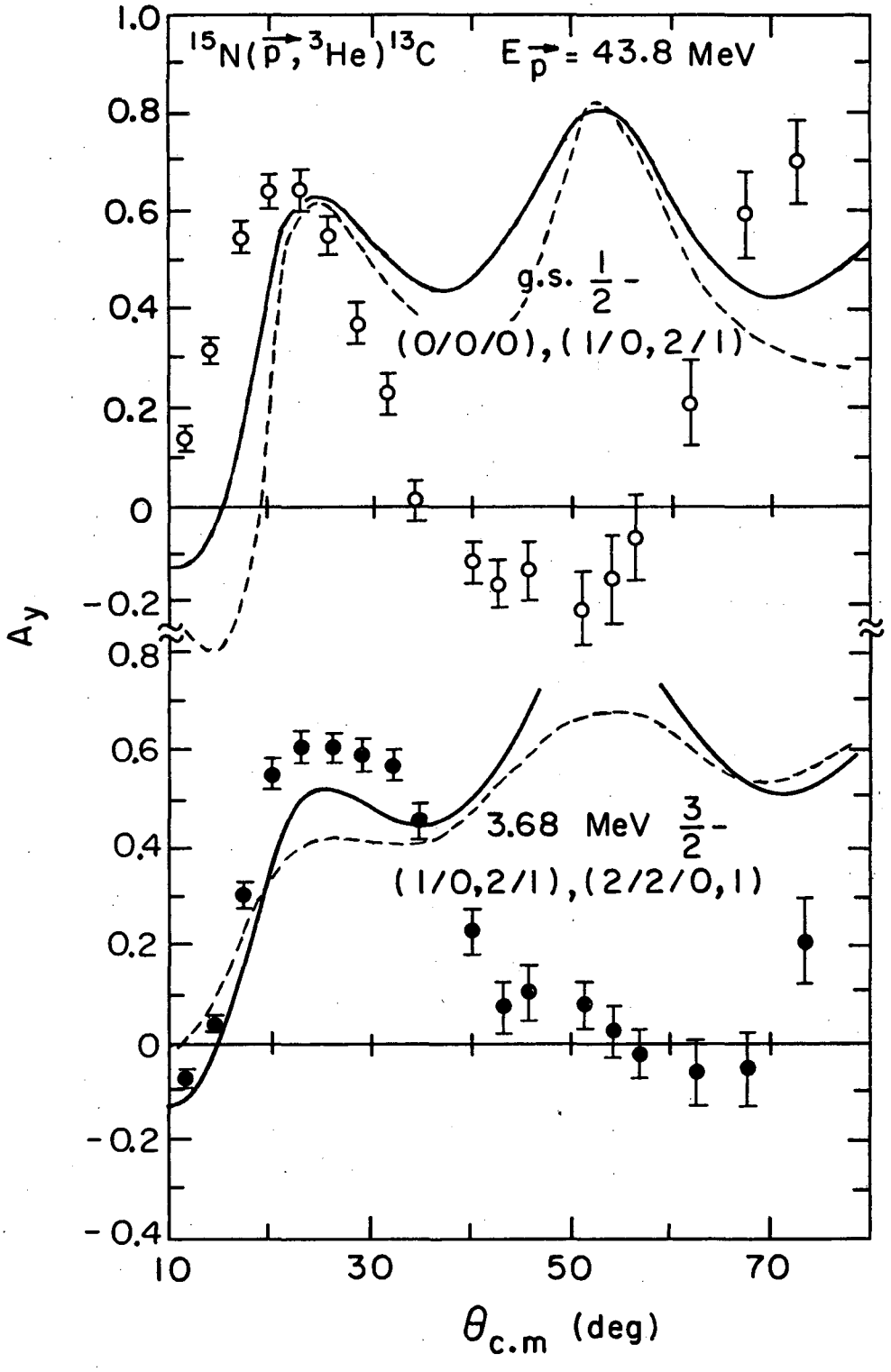


Fig. 25. Analyzing powers for the transitions shown in Fig. 24. The curves are DWBA calculations described in the text.

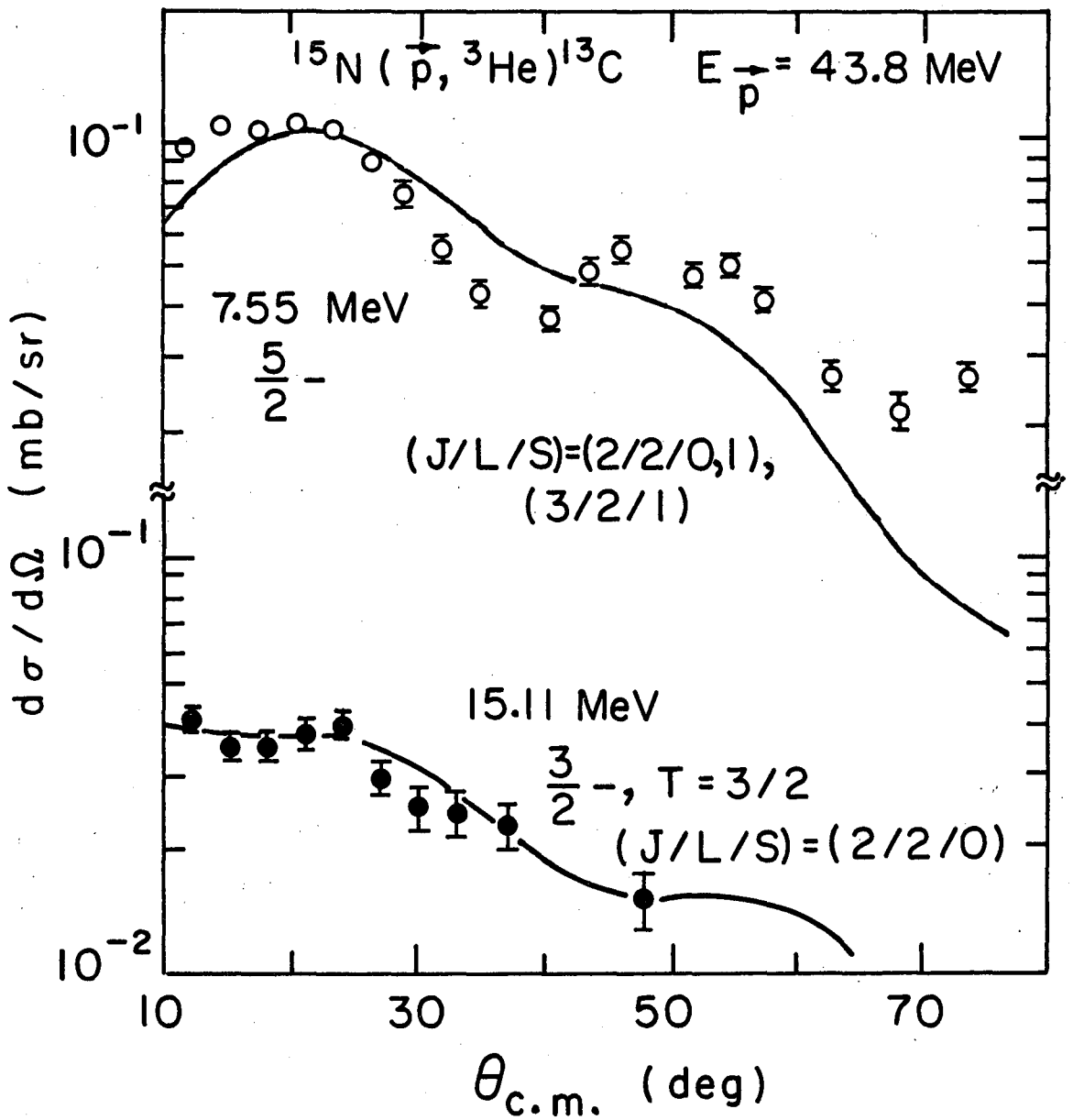


XBL737-3637A

Fig. 26. Differential cross sections for $^{15}N(\vec{p}, {}^3He)^{13}C$ 7.55 MeV and 15.11 MeV indicating transferred (J/L/S) and showing DWBA calculations (curves) normalized separately to the data and explained in the text. See also Fig. 27.

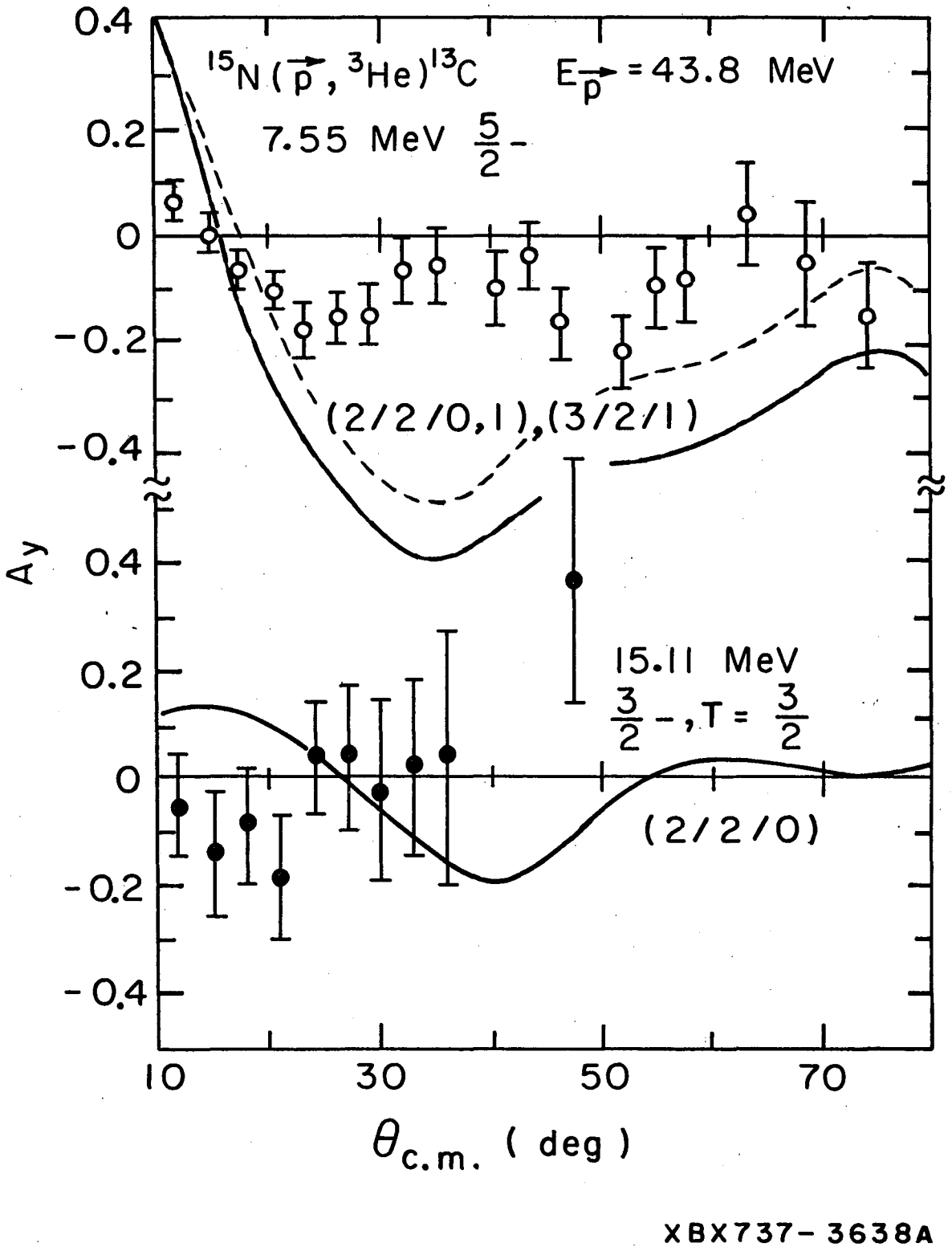


Fig. 27. Analyzing powers corresponding to the differential cross sections in Fig. 26, with DWBA fits described in the text shown by the curves. The dashed curve shows the effect of including spin dependence as explained in the text.

The $^{15}N(\vec{p}, {}^{3}He)$ results are shown in Figs. 24 to 27. Although these transitions lead to states in $^{13}C$ which are mirrors of the $^{13}N$ states, the increased complexity permitted in the $(\vec{p}, {}^{3}He)$ reaction makes it unlikely that either the $d\sigma/d\Omega$ or the $A_y$ to mirror states would be identical with the $(\vec{p},t)$ data. The transitions to the ground and first excited states both go by mixed L = 0, 2 and the wave functions indicate similar mixtures of L in both. The $d\sigma/d\Omega$ data (Fig. 24) indeed are in good agreement with the theory. In Fig. 25 are shown the $A_y$ data for the same two transitions. The theory again suggests that the two transitions should be nearly identical, and the data for the two transitions show reasonable similarity to each other, particularly at forward angles, but only fair agreement with the calculation in the same region. At angles beyond 30° c.m. neither transition agrees with the theory.

For the 7.55 MeV (5/2-) state, shown in Figs. 26 and 27 the selection rules allow L = 2, 4 but L = 4 is excluded in p-shell pick-up, so that the transition is pure L = 2 which both theory and experiment confirm for $d\sigma/d\Omega$. However, the analyzing power in Fig. 27 shows that the predicted $A_y$ is quite different from that for any of the L = 2 transitions arising in $(\vec{p},t)$. Although the $^{15}N(\vec{p}, {}^{3}He)^{13}C$ (7.55 MeV) transition proceeds via both S = 0 and 1 (see Table III), the structure amplitudes indicate that it is dominated by the S = 0 component, and, in fact incorporating the spin-dependence by further enhancing this component gave no change in the $d\sigma/d\Omega$, and only a minor effect in the $A_y$. One therefore might have expected more experimental similarity with the $A_y$ for the other L = 2, S = 0 transitions.

The pure L = 0 ($\vec{p}$, $^3$He) transition to the $^{13}$C state at 15.11 MeV (3/2-, T = 3/2) is also shown in Figs. 26 and 27. Good DWBA agreement for $d\sigma/d\Omega$ was obtained although the angular range for detecting $^3$He's from transitions to states at this high excitation was restricted by the thickness of the $\Delta E$ detectors. Again, as with the ($\vec{p}$,t) analog, the $A_y$ comparison with theory is limited by the large experimental errors-bars.

3. $^{13}C(\vec{p},t)$ and ($\vec{p}$, $^3$He)

Results from experiments on these reactions have been reported with unpolarized beams (Fle 68a, Cos 68). Representative ($\vec{p}$,t) and ($\vec{p}$, $^3$He) spectra from the present work showing final states in $^{11}$C and $^{11}$B are shown in Fig. 28. The $d\sigma/d\Omega$ and $A_y$ data and calculations for the mirror transitions and the T = 3/2 analogs are shown in Figs. 29 to 39.

Three L = 2, ($\vec{p}$,t) transitions to the ground (3/2-), 4.31 MeV (5/2-) and 4.79 MeV (3/2-) states respectively are shown in Figs. 29 and 30. While detailed agreement for $d\sigma/d\Omega$ with the DWBA is not achieved, there is a reasonable overall agreement. For the gound state $A_y$ in Fig. 30, however, there is excellent agreement. Nevertheless, the calculated fits are considerably less satisfactory for the two excited states. In contrast to the L = 2 disagreements for the $^{16}$O and $^{15}$N data, in $^{13}C(\vec{p},t)$ no dramatic difference--such as being completely out of phase--arises. Instead, the discrepancies are more subtle, in that the calculation retains an overall qualitative similarity, and yet fails to reproduce the details of magnitude and phase.

A more striking comparison with the results on the $^{15}$N and $^{16}$O targets occurs for the pure L = 0 transition to the 2.00 MeV (1/2-) state

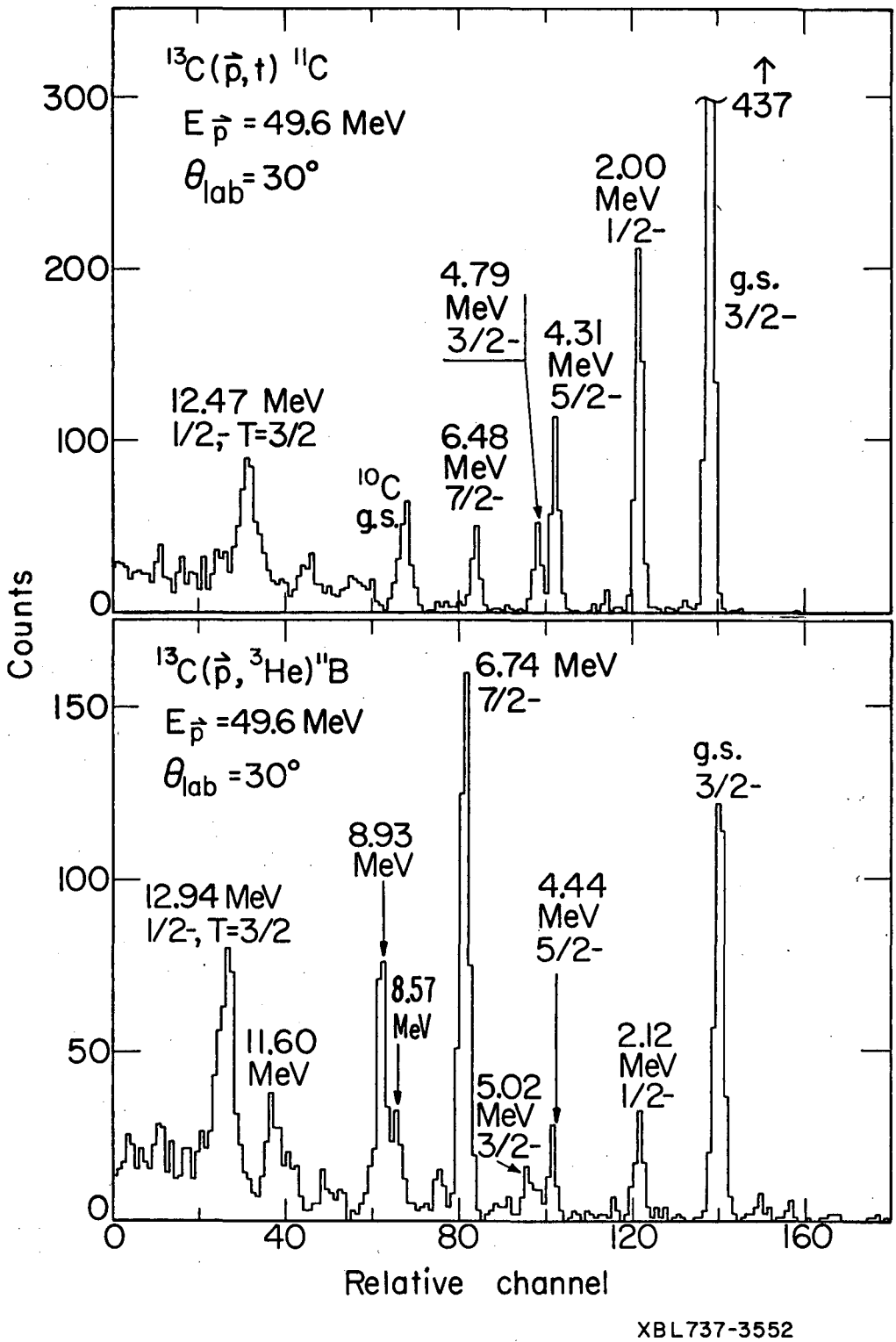


Fig. 28. Energy spectra for the $^{13}C(\vec{p},t)^{11}C$ and $^{13}C(\vec{p},\ ^{3}He)^{11}B$ reactions.

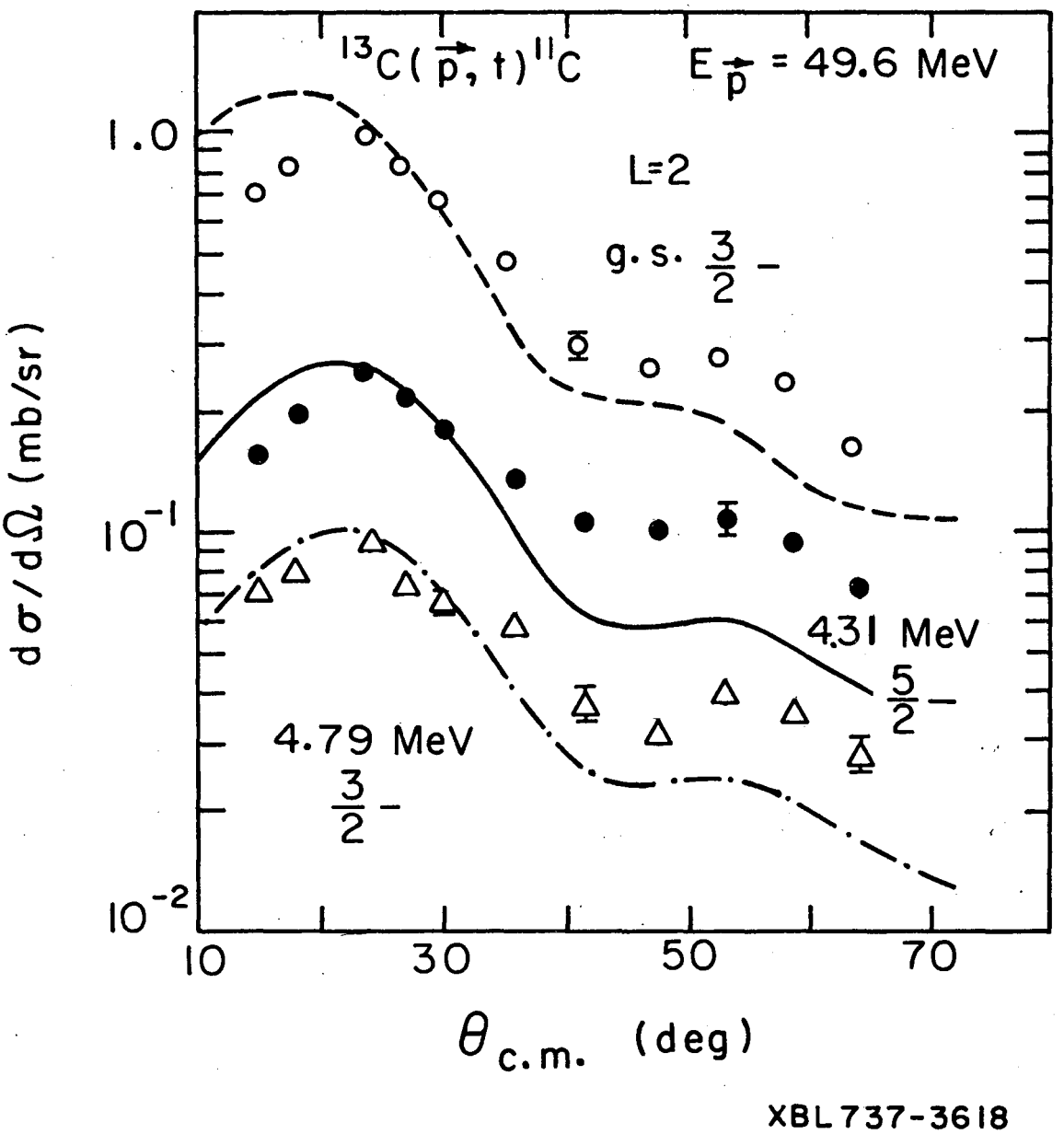


Fig. 29. Differential cross sections for L = 2 $^{13}C(\vec{p},t)^{11}C$ transitions. The curves are DWBA calculations described in the text and normalized separately to the data. See also Fig. 30.

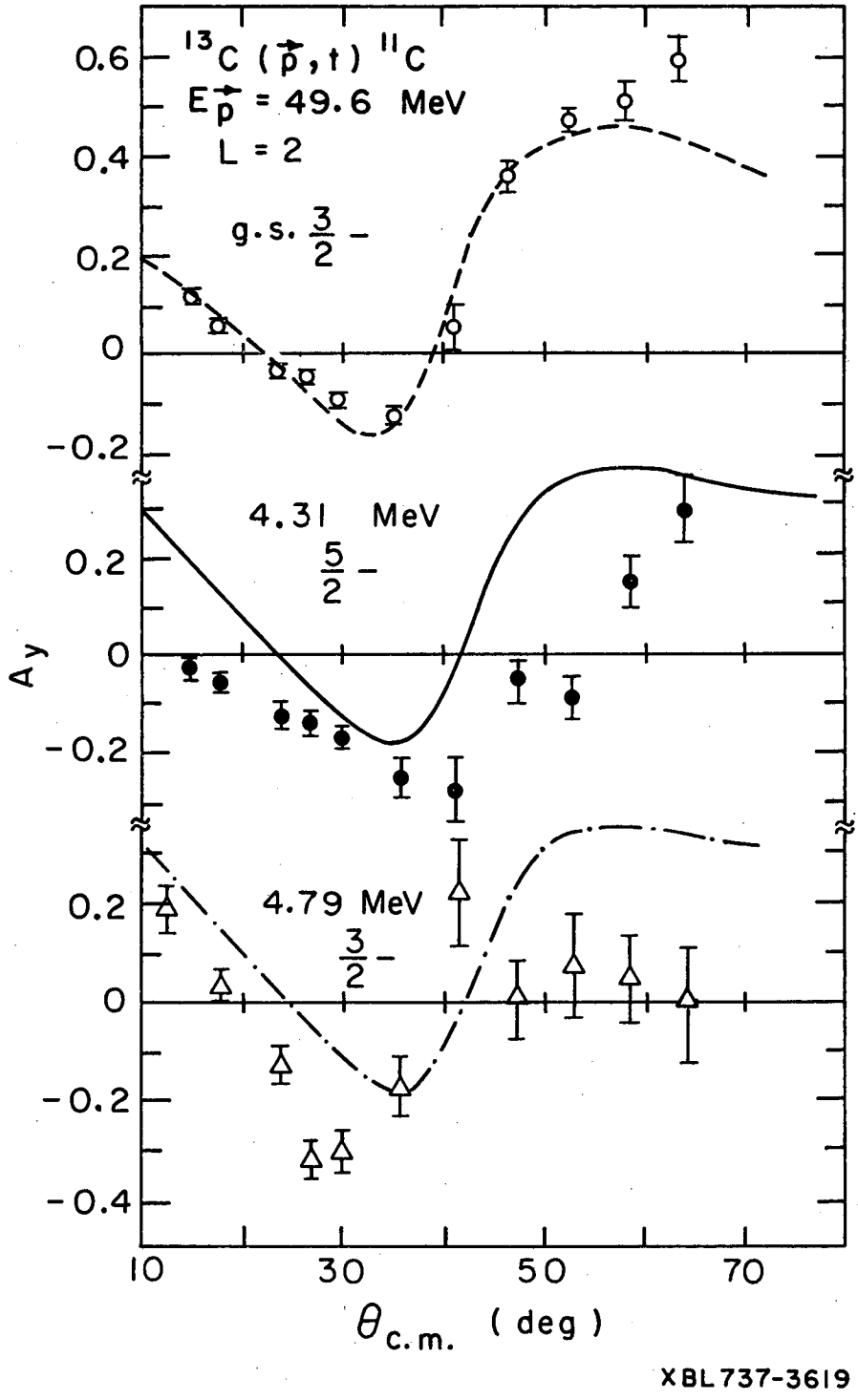


Fig. 30. Analyzing powers for the L = 2 transitions shown in Fig. 29 with curves indicating DWBA calculations described in the text.

in $^{11}C$ shown in Figs. 31 and 32. In Fig. 32 consider first only the dashed curve which is obtained using the mass-3 optical parameters (d) from Table I which yielded the most favorable overall fits for this target. As for the L = 2 cases above, the $d\sigma/d\Omega$ is in poorer detailed agreement than for the $^{16}O$ or $^{15}N$ results, but the $A_y$ shows no similarity whatsoever to the data, whereas rather good L = 0 agreement was obtained for both the other targets. It is interesting to note also that the data in Fig. 32 indicate a different behavior than in the other L = 0 cases, particularly at forward angles although the rather strong analyzing power at $\sim 60^\circ$ c.m. is similar in all. The small analyzing power at forward angles is somewhat similar to the results on $^{12}C(p,t)^{10}C$ (g.s.) (Nel 70b).

It was possible to obtain a prediction for the $A_y$ which qualitatively gave the strong maximum at $60^\circ$ by using a different set of optical parameters for the exit channel; these are listed as (e) in Table I. The results of this calculation are indicated in Fig. 32 by the dot-dashed curve. As can be seen, the data at forward angles are still not reproduced and the improvement in the $A_y$ fit is only minor. Agreement with the $d\sigma/d\Omega$ data using this set of parameters deteriorated considerably and is not shown. In addition, calculations with this set of parameters gave reduced overall agreement to the other transitions on $^{13}C$, especially that to the ground state, and are also not shown.

The results for the L = 0 analog transition to the 12.47 MeV (1/2-, T = 3/2) state also presented in Figs. 31 and 32 show that, although detailed fits to neither $d\sigma/d\Omega$ nor $A_y$ are obtained, the qualitative features of both are reasonably well reproduced.

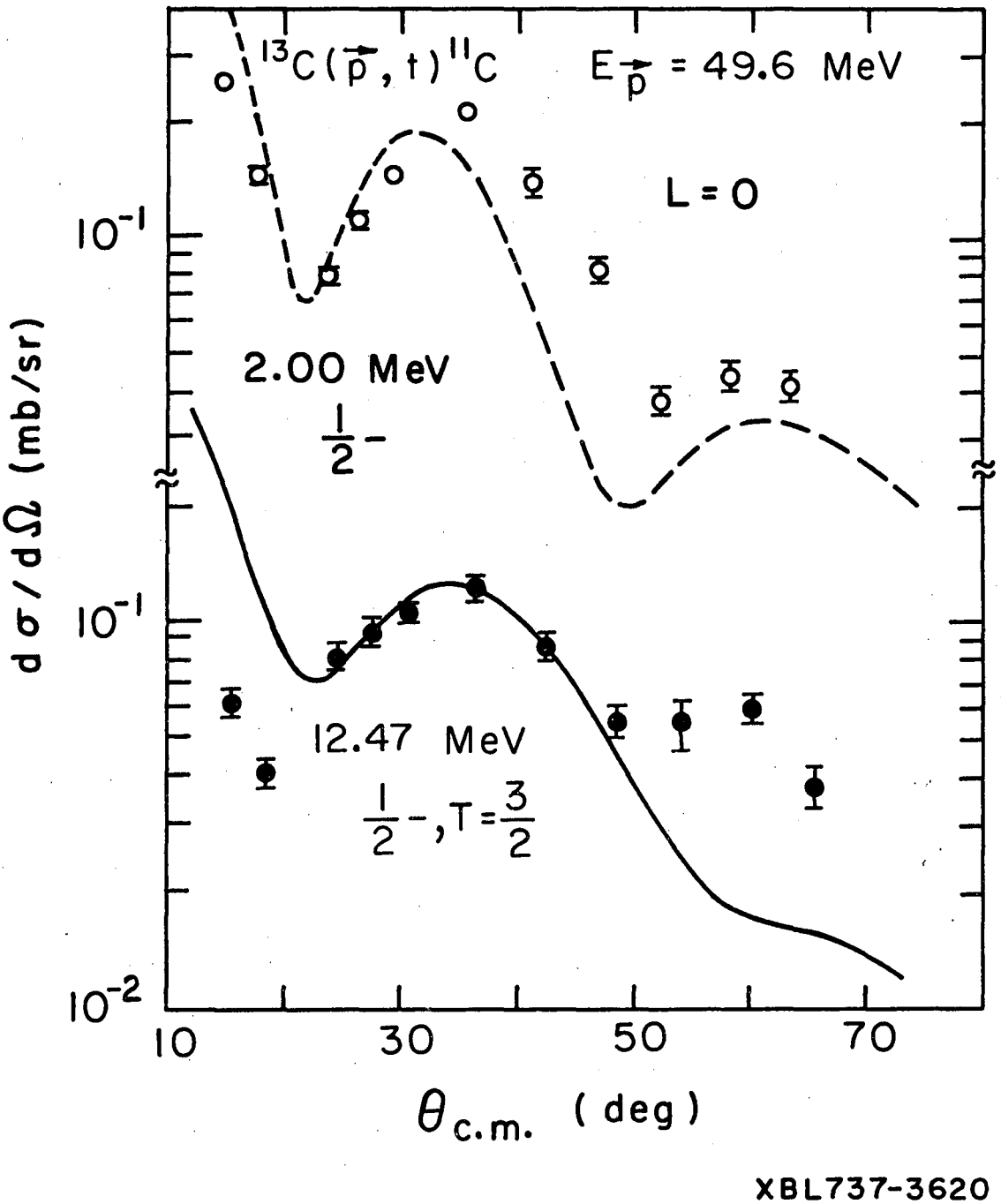


Fig. 31. Differential cross sections for L = 0 $^{13}C(\vec{p},t)^{11}C$ transitions. The curves are DWBA fits described in the text and normalized separately to the data. See also Fig. 32.

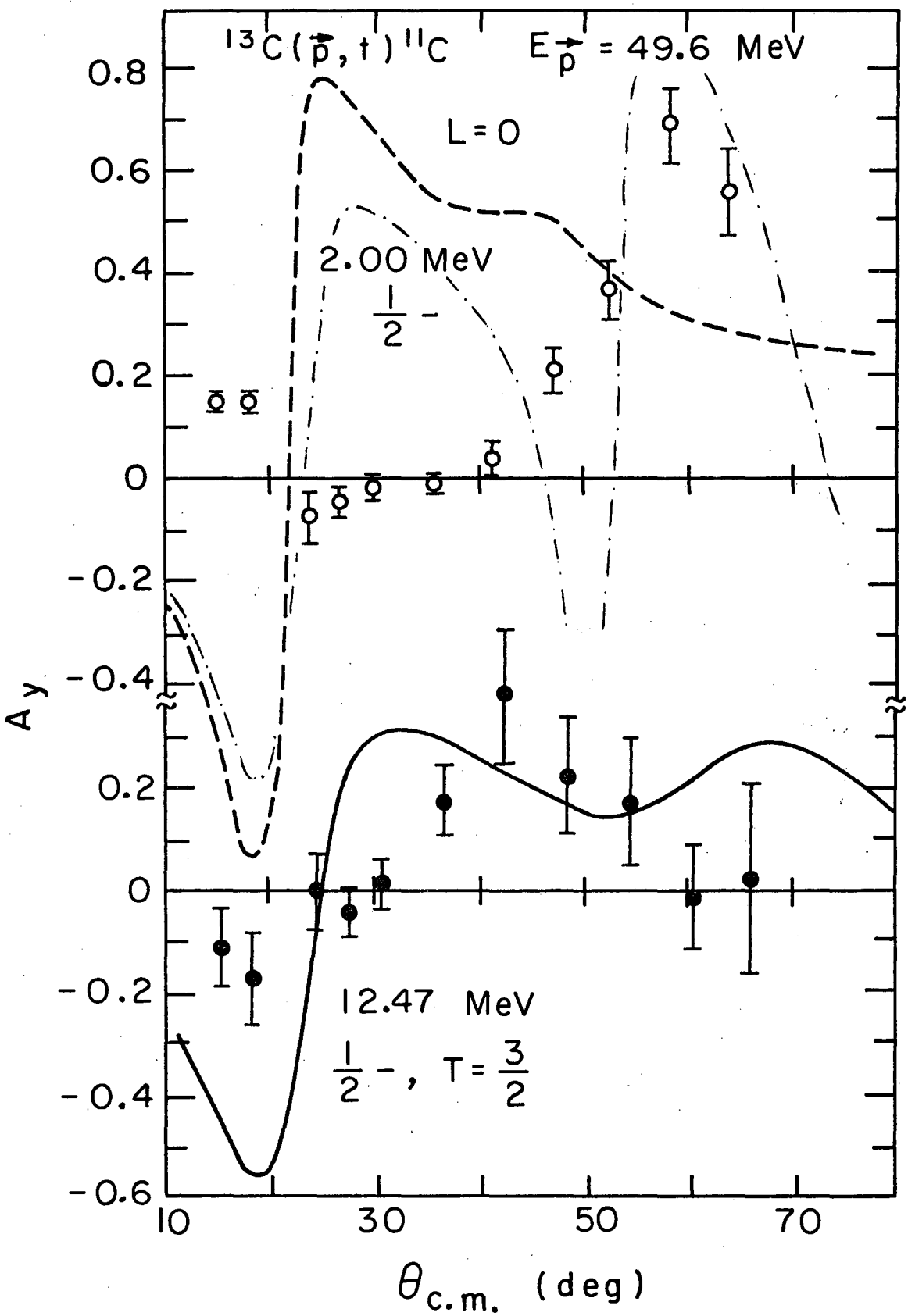


Fig. 32. Analyzing powers for the L = 0 transitions shown in Fig. 31 with curves indicating DWBA calculations. The dash-dot curve was obtained using an exit channel optical potential which qualitatively reproduced the back angle maximum in $A_y$, while the other curves result from using an optical potential judged to give the best overall fits on $^{13}C$.

The $(\vec{p},t)$ transition to the 6.48 MeV (7/2-) state in $^{11}C$ is L-forbidden, if simple p-shell pick-up of the two neutrons is assumed. Two explanations for the surprisingly large strength of the transition have been proposed (Fle 68a). The first assumes that a two-step mechanism plays a major role in the pick-up, involving an allowed L = 2 process, and the second hypothesizes that a small admixture of (1p 1f) structure in the $^{13}C$ ground state would account for the observed strength and permit the necessary L = 4 transfer. Calculations showing pure L = 2 and L = 4 transfer are shown with the data for $d\sigma/d\Omega$ and $A_y$ in Fig. 33. It is apparent that some suitable admixture of L = 2 and 4 might account for the nearly isotropic $d\sigma/d\Omega$, but it would seem that an L = 2 component has the dominant effect on the $A_y$. These results do not resolve the questions about this unusual transition but may indicate the presence of an allowed L = 2 process.

The $^{13}C(\vec{p}, {}^3He)$ transfers leading to states in $^{11}B$ which are mirrors of the above $^{11}C$ states are shown in Figs. 34 to 39. As for the $^{15}N$ target, $(\vec{p}, {}^3He)$ on $^{13}C$ is allowed to proceed, in general, through a complex admixture of transferred (J/L/S). Though the theory reproduces $d\sigma/d\Omega$ rather well for all these transitions, no agreement is obtained for $A_y$ with the exception in Fig. 37 of the 12.94 MeV (1/2-, T = 3/2) transition where a fair qualitative fit is obtained. The fit to the 6.74 MeV (7/2-) transition in Fig. 39 (allowed in $(\vec{p}, {}^3He)$) too is qualitatively correct, but the magnitude is wrong by a factor of two.

Transitions to three states in $^{11}B$ summarized in Table IV were also analyzed and the data are shown in Figs. 40 and 41. These are states for which no mirror states in $^{11}C$ were observed and two are of

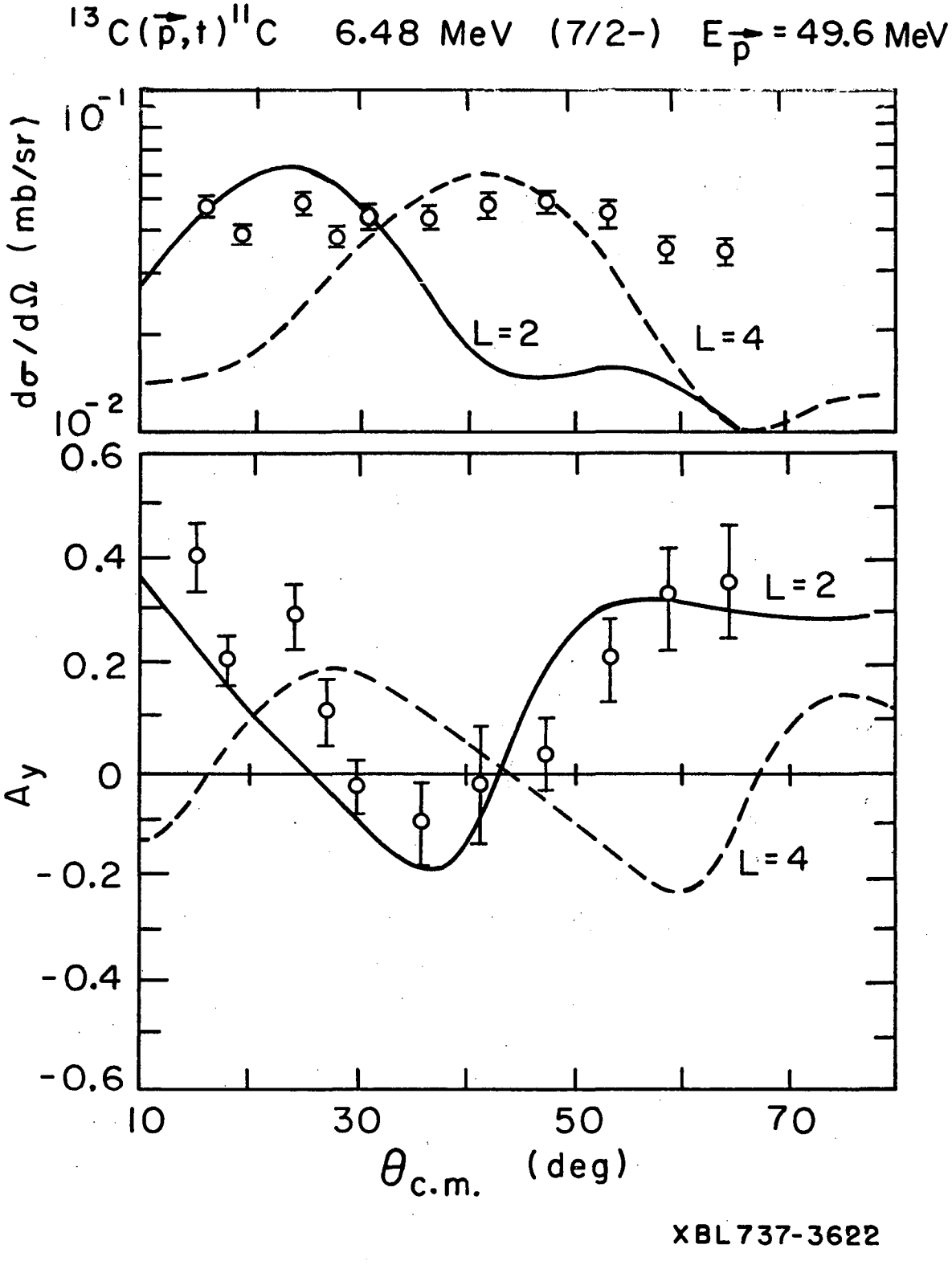


Fig. 33. Differential cross section and analyzing power for the L-forbidden $^{13}C(\vec{p},t)^{11}C$ transition to the 6.48 MeV (7/2-) state. The curves correspond to DWBA calculations with L = 2 and 4 as explained in the text, which are normalized separately to the data for $d\sigma/d\Omega$.

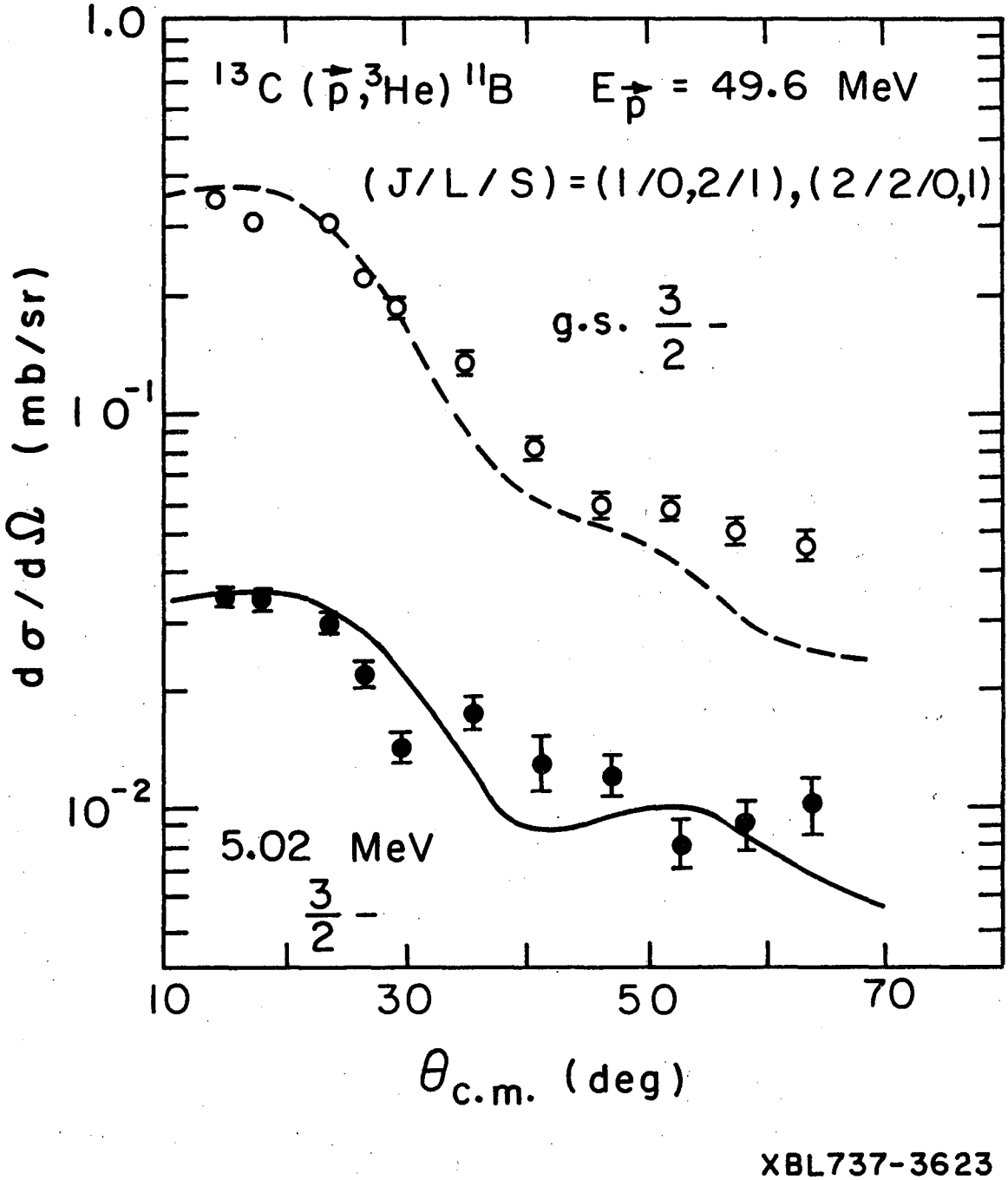


XBL737-3623

Fig. 34. Differential cross sections for two $^{13}C(\vec{p}, {}^{3}He)^{11}B$ transitions with the same allowed (J/L/S) transfer as indicated in the figure. The curves are DWBA fits described in the text and normalized separately to the data. See also Fig. 35.

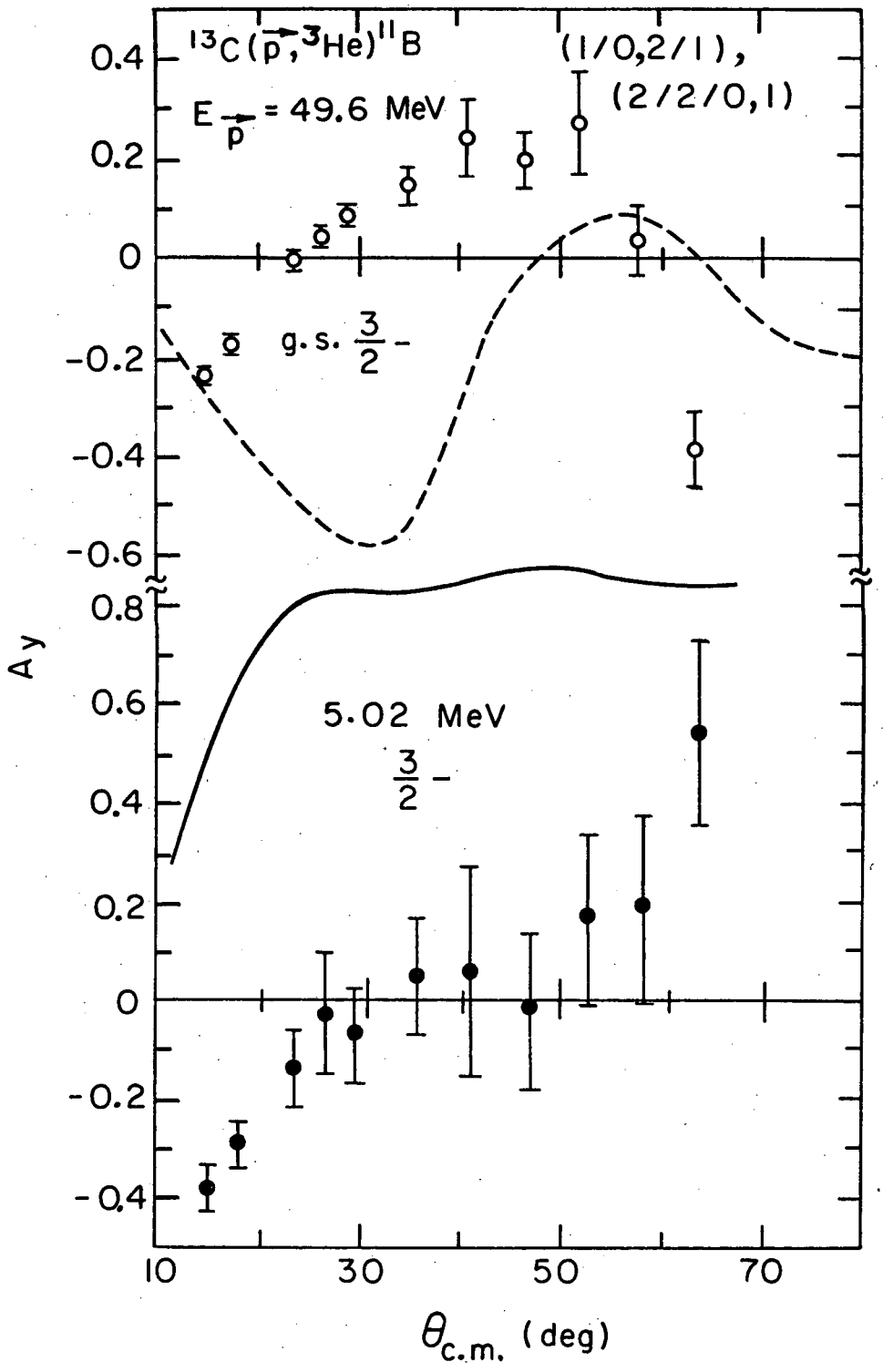


Fig. 35. The analyzing powers for the transitions shown in Fig. 34 with DWBA fits given by the curves and described in the text.

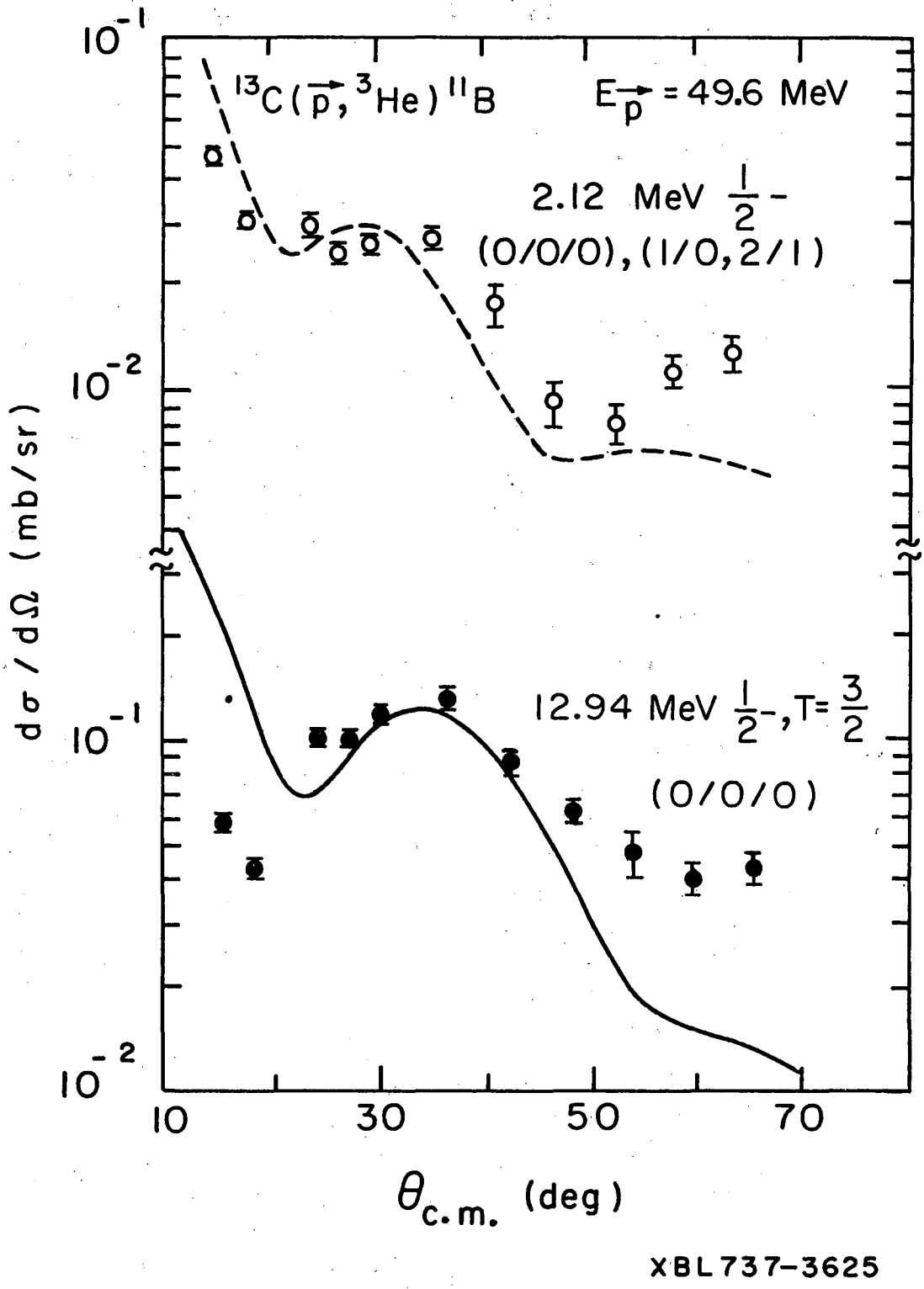


Fig. 36. Differential cross sections for two $^{13}C(\vec{p}, {}^3He)^{11}B$ transitions showing allowed (J/L/S) transfer. The curves describe DWBA fits discussed in the text and normalized separately to the data. See also Fig. 37.

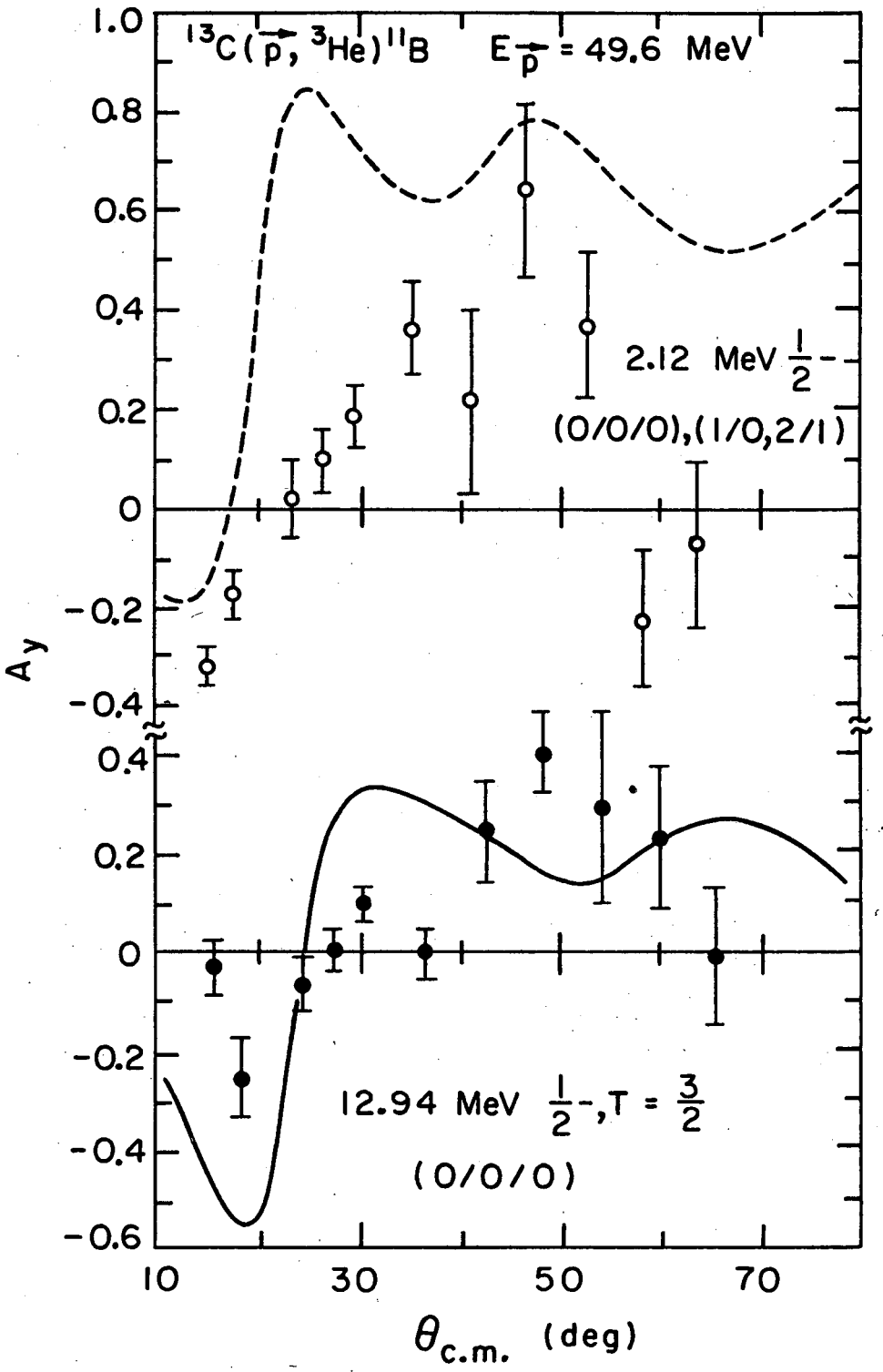


XBL 737-3626

Fig. 37. Analyzing powers for the transitions also shown in Fig. 36 with DWBA fits (curves) described in the text.

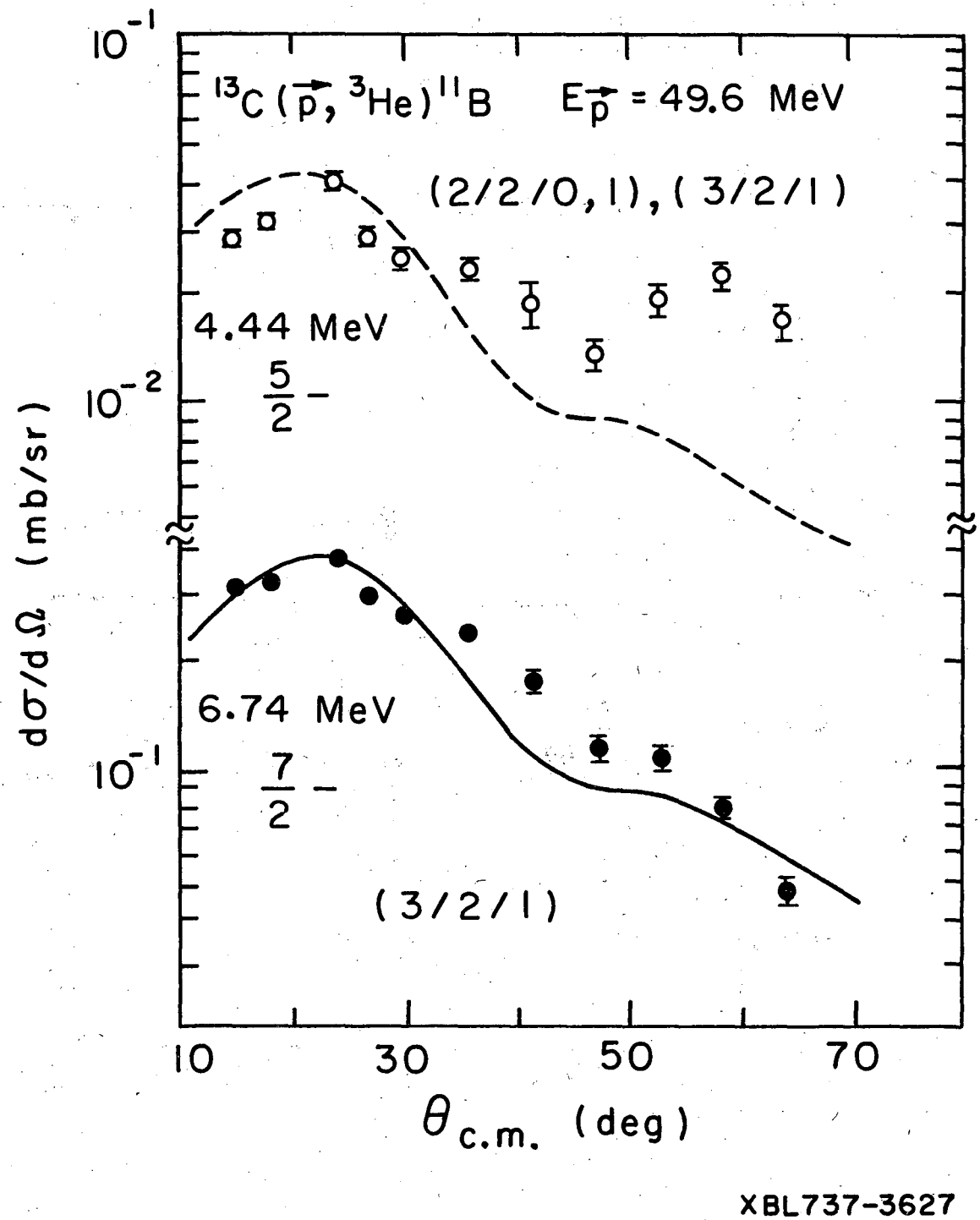


XBL737-3627

Fig. 38. Differential cross sections for $(\vec{p}, {}^3He)$ transitions to states in $^{11}B$, indicating the allowed transferred (J/L/S), and DWBA fits explained in the text which are normalized separately to the data. See also Fig. 39.

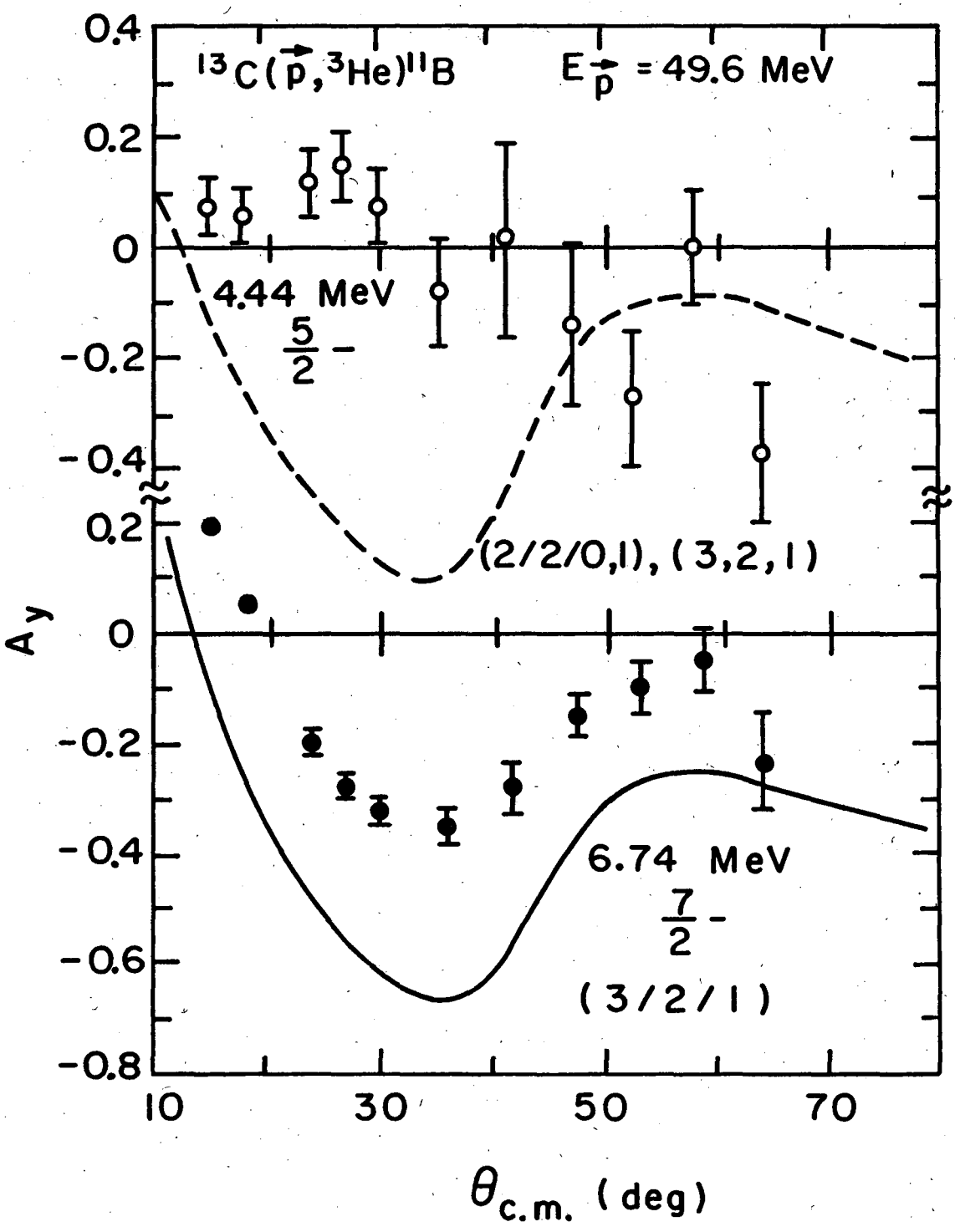


XBL737-3628

Fig. 39. Analyzing powers corresponding to the differential cross sections described in Fig. 38 with DWBA fits shown by the curves and described in the text.

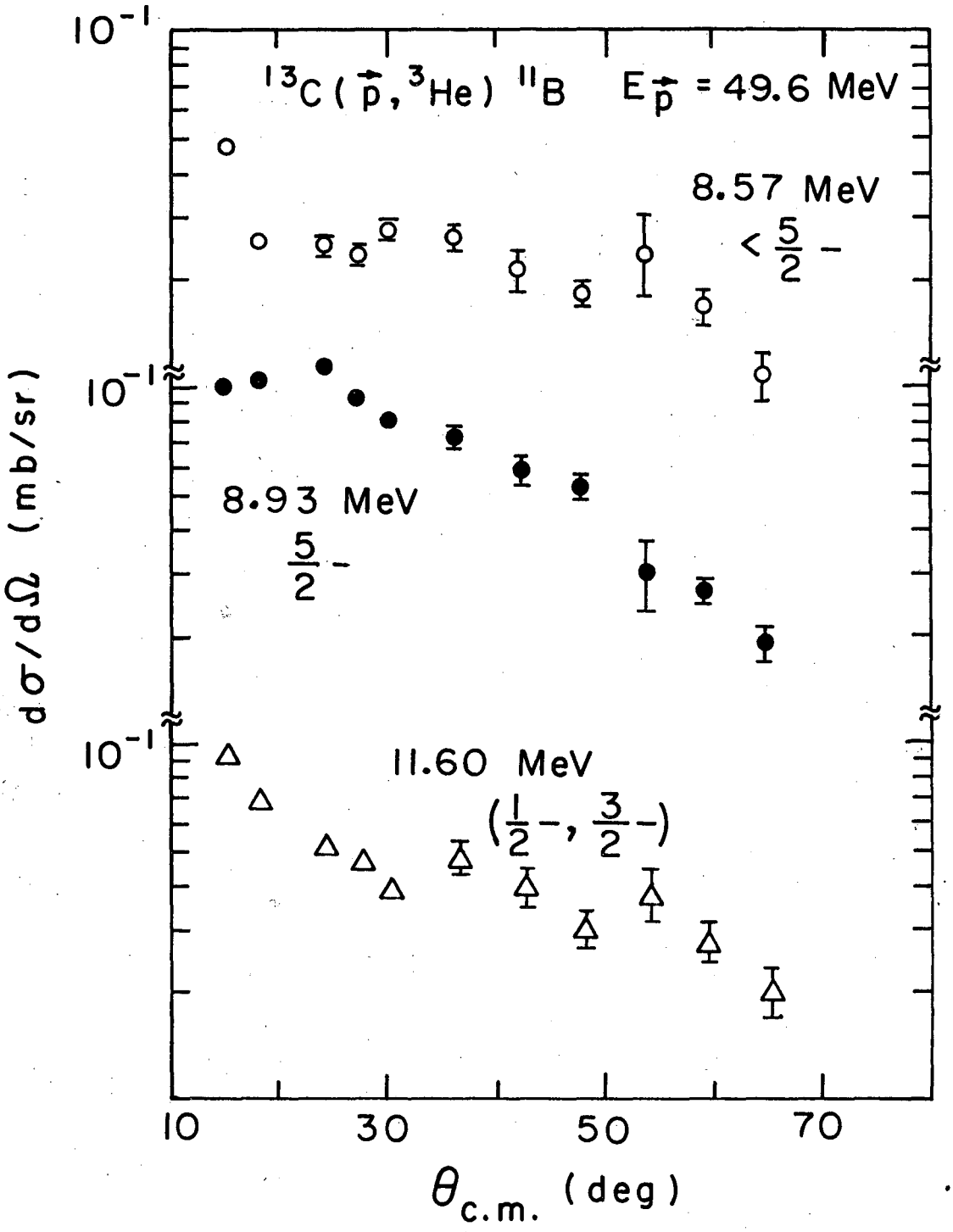


XBL737-3629

Fig. 40. Differential cross section data for the three $(\vec{p}, {}^{3}He)$ transitions to states in $^{11}B$ for which no mirror transitions to $^{11}C$ were observed. See also Fig. 41.

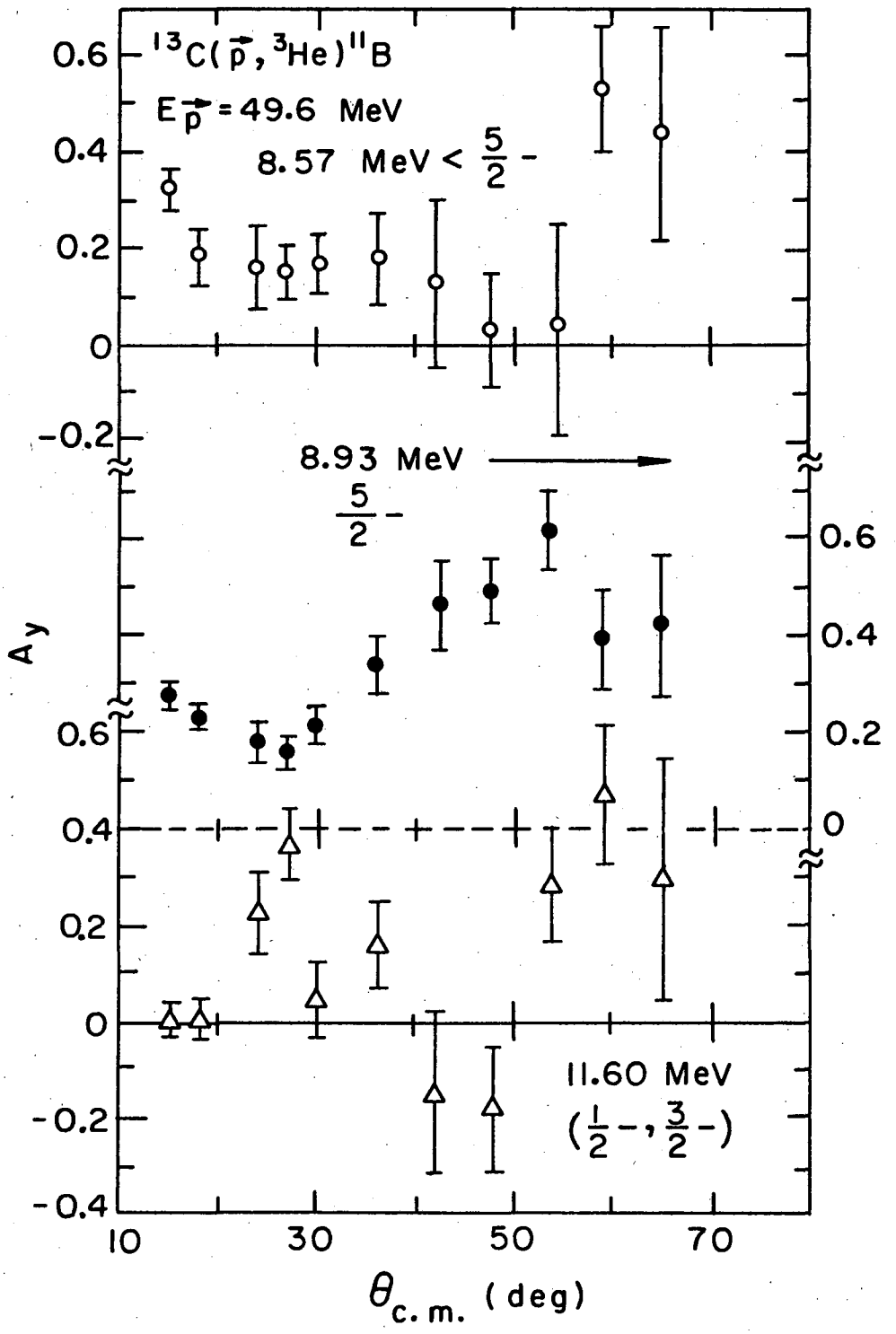


Fig. 41. Analyzing powers for the transitions shown in Fig. 40.

uncertain $J^{\pi}$ assignment (Fle 67). Neither the differential cross sections nor the analyzing powers for any of these transitions indicate characteristics of any of the simple transitions observed and no clear interpretation of these data is apparent. No DWBA calculations were attempted for these cases.

4. $^{9}Be(\vec{p},t)$, $(\vec{p}, {}^{3}He)$, and $^{7}Li(\vec{p},t)$, $(\vec{p}, {}^{3}He)$

The spectroscopy of mass-7 and mass-5 nuclei and the search for T = 3/2 states in these nuclei have been reported using these two nucleon transfer reactions induced by unpolarized beams (Cer 66, McG 68, Dét 65). Typical triton and $^{3}He$ spectra from the $^{9}Be$ and $^{7}Li$ targets are shown in Figs. 42 and 43. Because both these target nuclei have $J^{\pi} = 3/2-$, transitions to all final states observed, (see Table IV), with the exception of the weak 0.431 MeV (1/2-) state in $^{7}Be$, can proceed via multiple transfers of (J/L/S).

Our predominantly unsuccessful attempts to fit the analyzing powers of compound transitions in the three lower spin targets previously discussed suggests that there is little reason to expect the simple theory to prove adequate in accounting for the $A_y$ for $(\vec{p},t)$ and $(\vec{p}, {}^{3}He)$ on $^{9}Be$ or $^{7}Li$. The experimental results are presented in Figs. 44 to 51, and no DWBA calculations were attempted.

The ground state analyzing powers in mass-7 are shown in Figs. 45 and 49 and were obtained from two experiments, in one of which the energy resolution was not adequate to resolve the first excited states. In the second experiment, with improved resolution, the ground and first excited states were resolved and analyzed separately at six angles. By using a

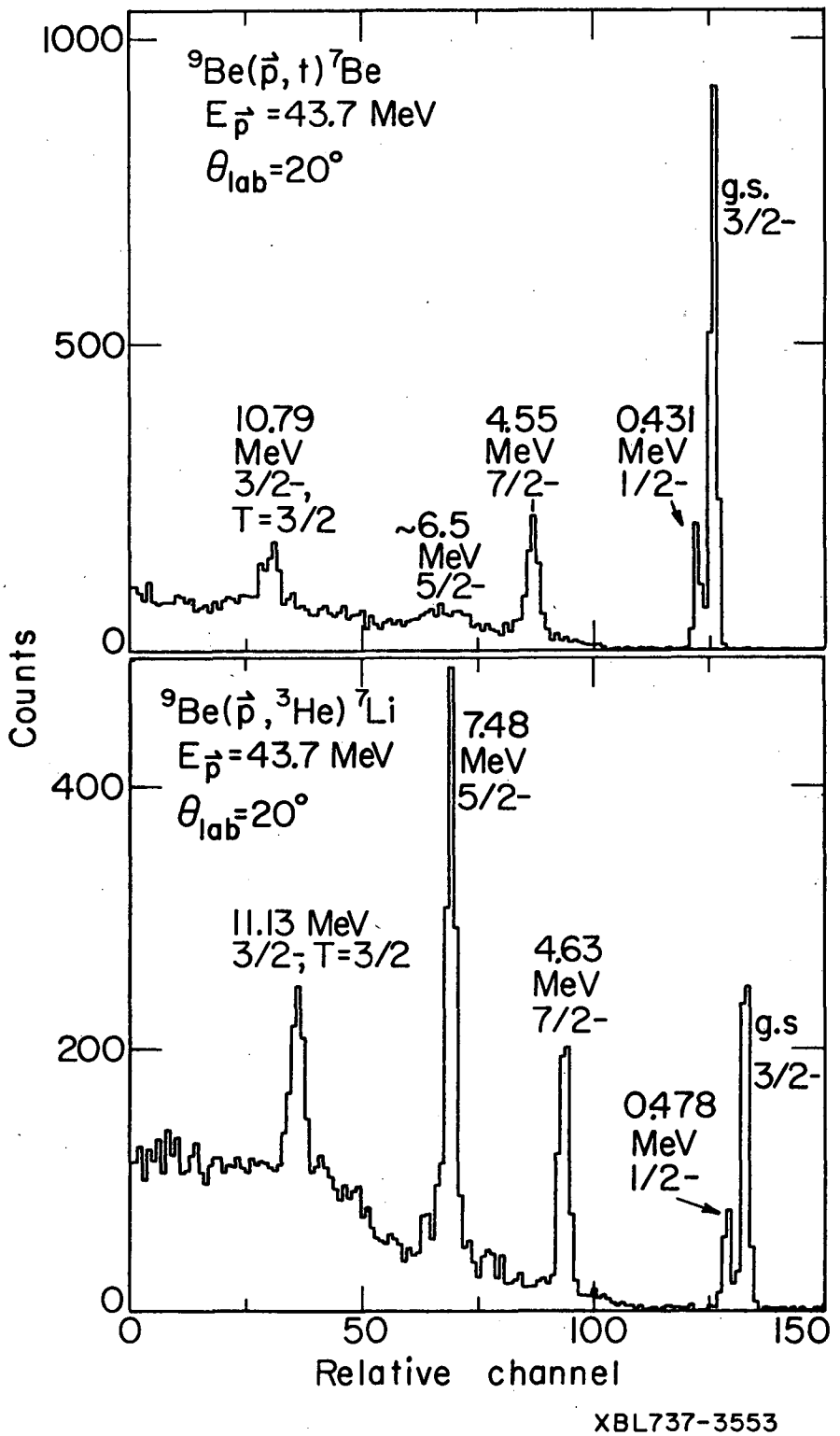


Fig. 42. Energy spectra for the $^9$Be($\vec{p}$,t) $^7$Be and $^9$Be($\vec{p}$, $^3$He) $^7$Li reactions.

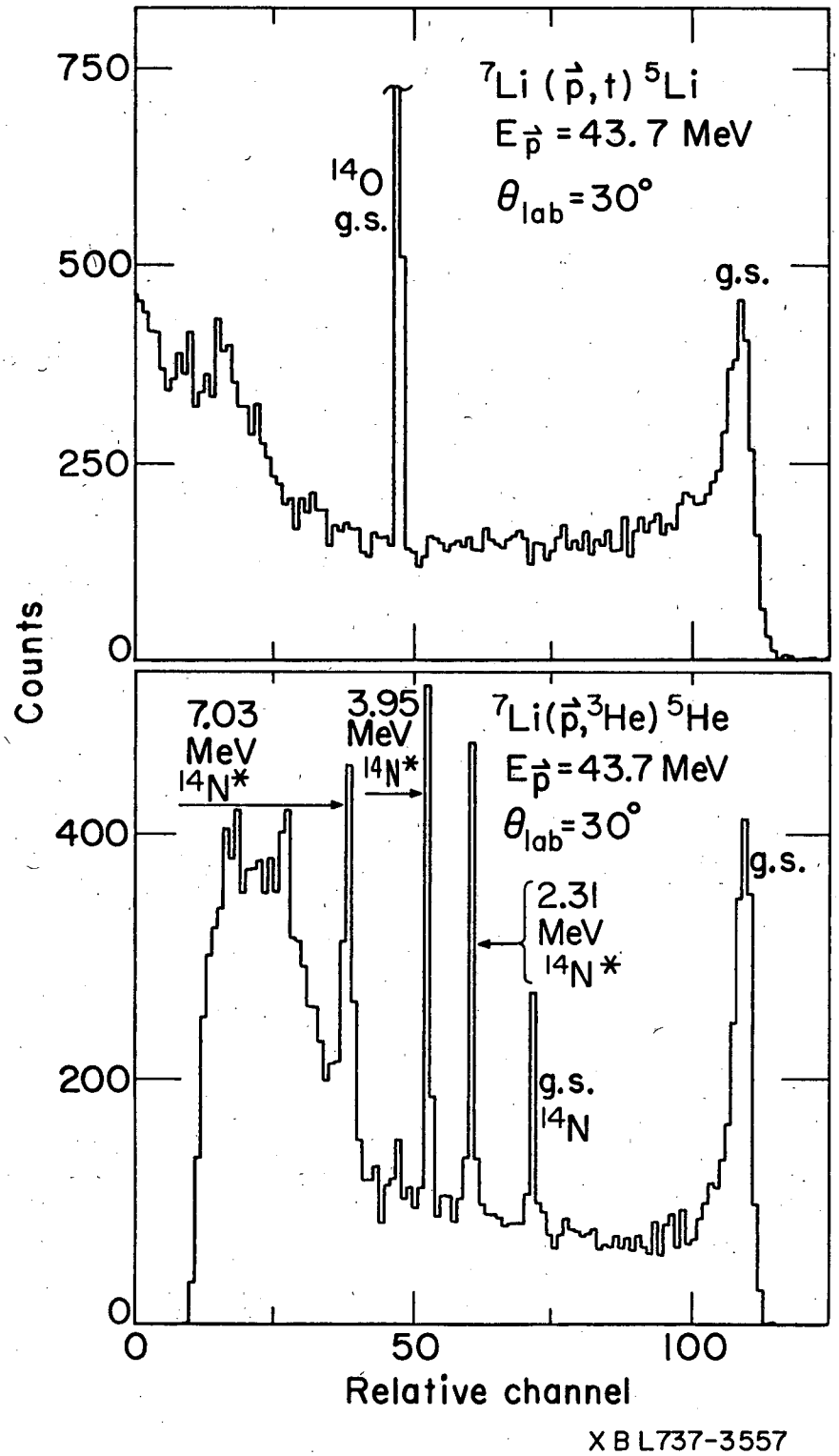


Fig. 43. Energy spectra for the $^7$Li($\vec{p}$,t)$^5$Li and $^7$Li($\vec{p}$, $^3$He)$^5$He reactions.

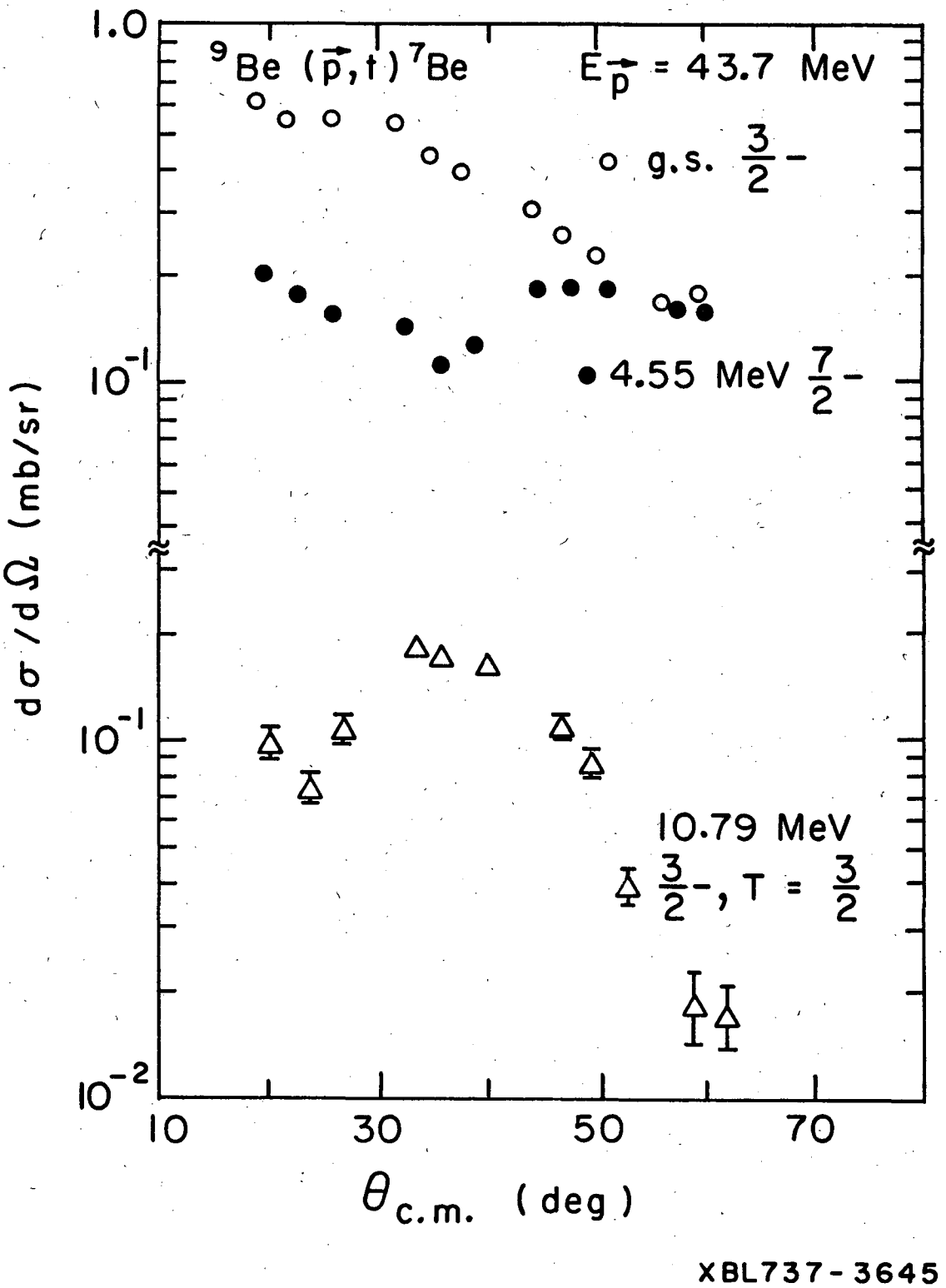


Fig. 44. Cross section data for three ($\vec{p}$,t) transitions to states in $^7$Be. See also Figs. 45 and 46.

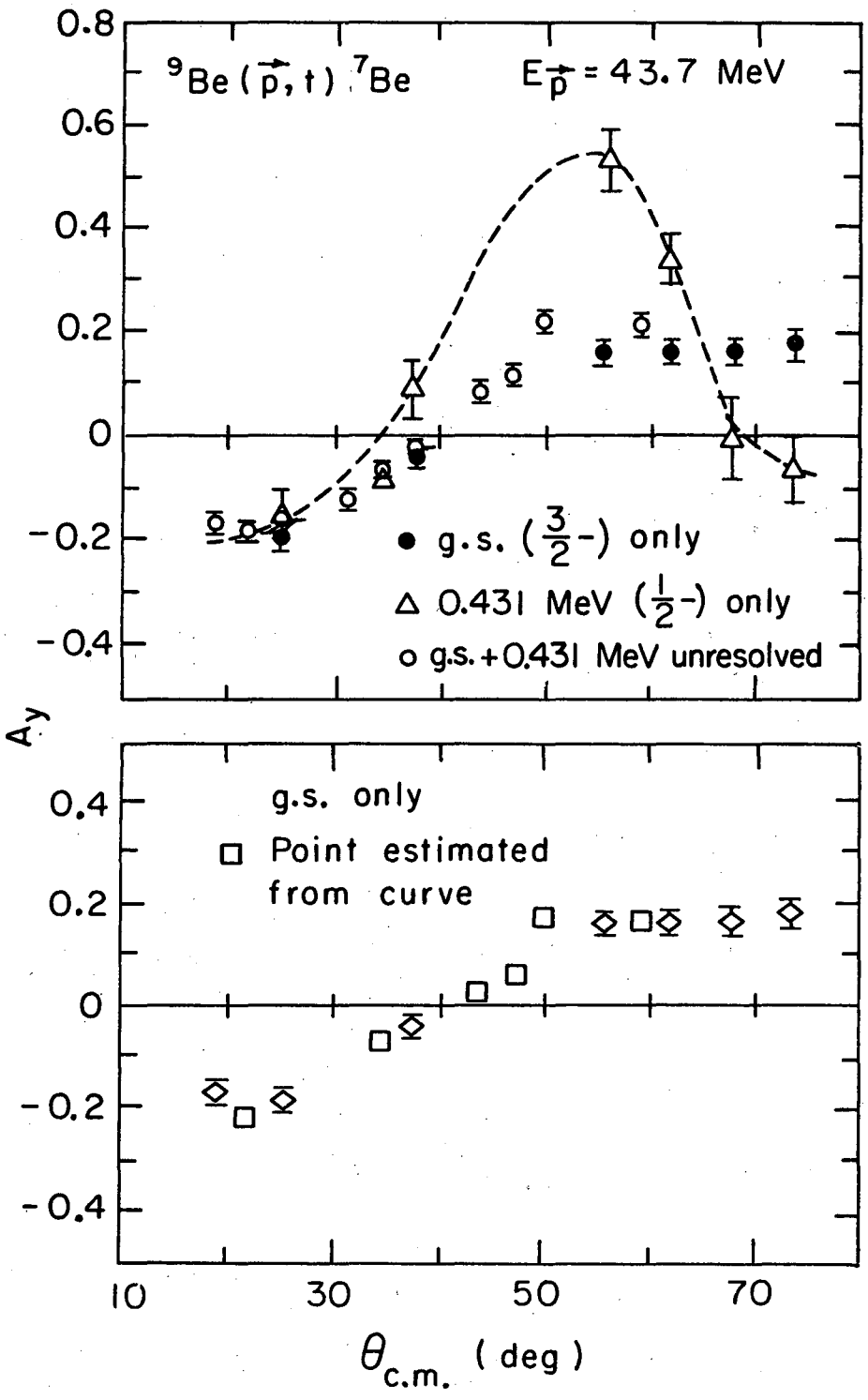


Fig. 45. Analyzing power data for the $^9$Be($\vec{p}$,t)$^7$Be ground state (shown in Fig. 44) and first excited state transitions. The data analysis is explained in the text.

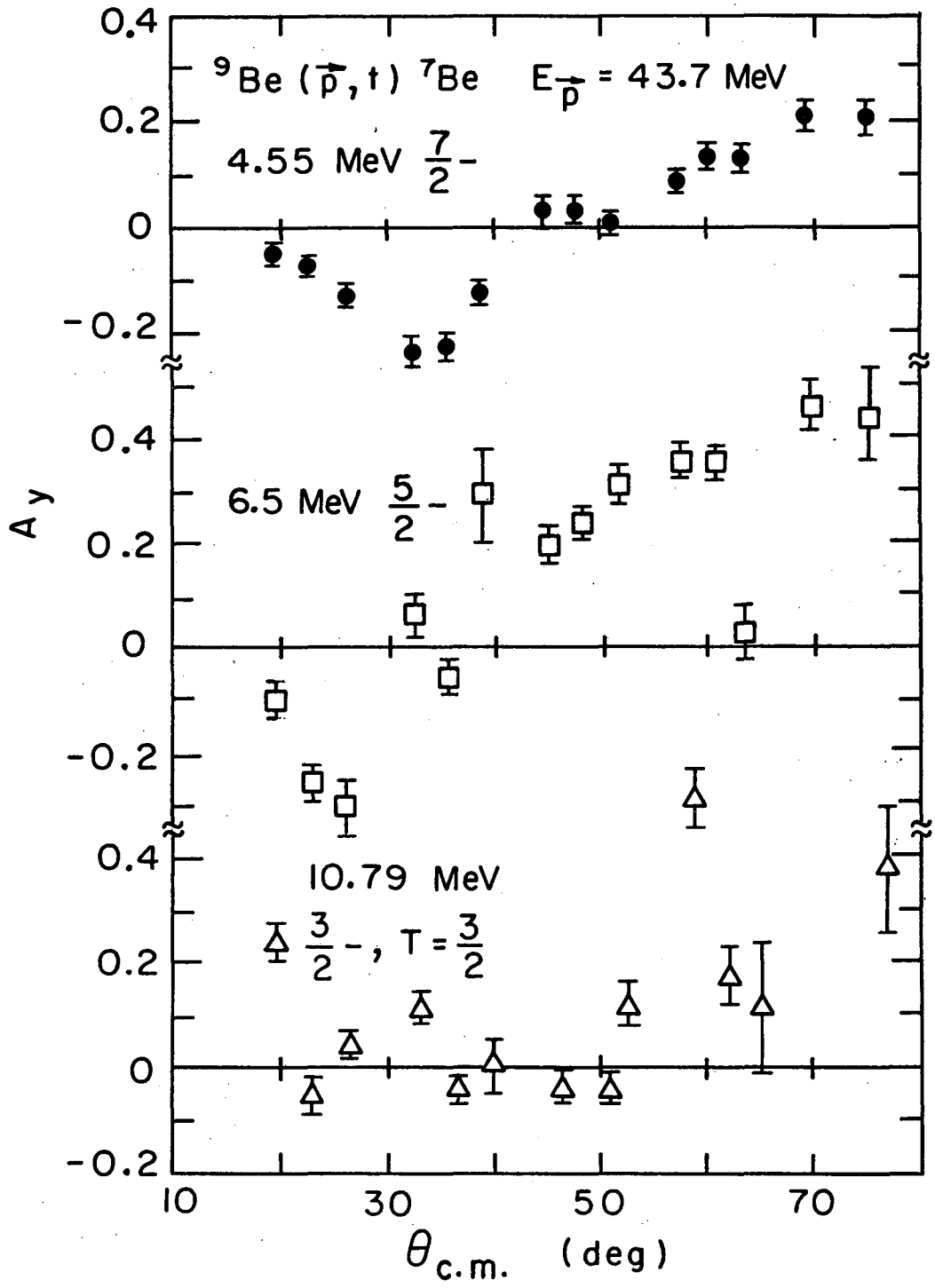


XBL737-3647

Fig. 46. Analyzing power data for three ($\vec{p}$,t) transitions to states in $^7$Be, for two of which the cross sections are shown in Fig. 44.

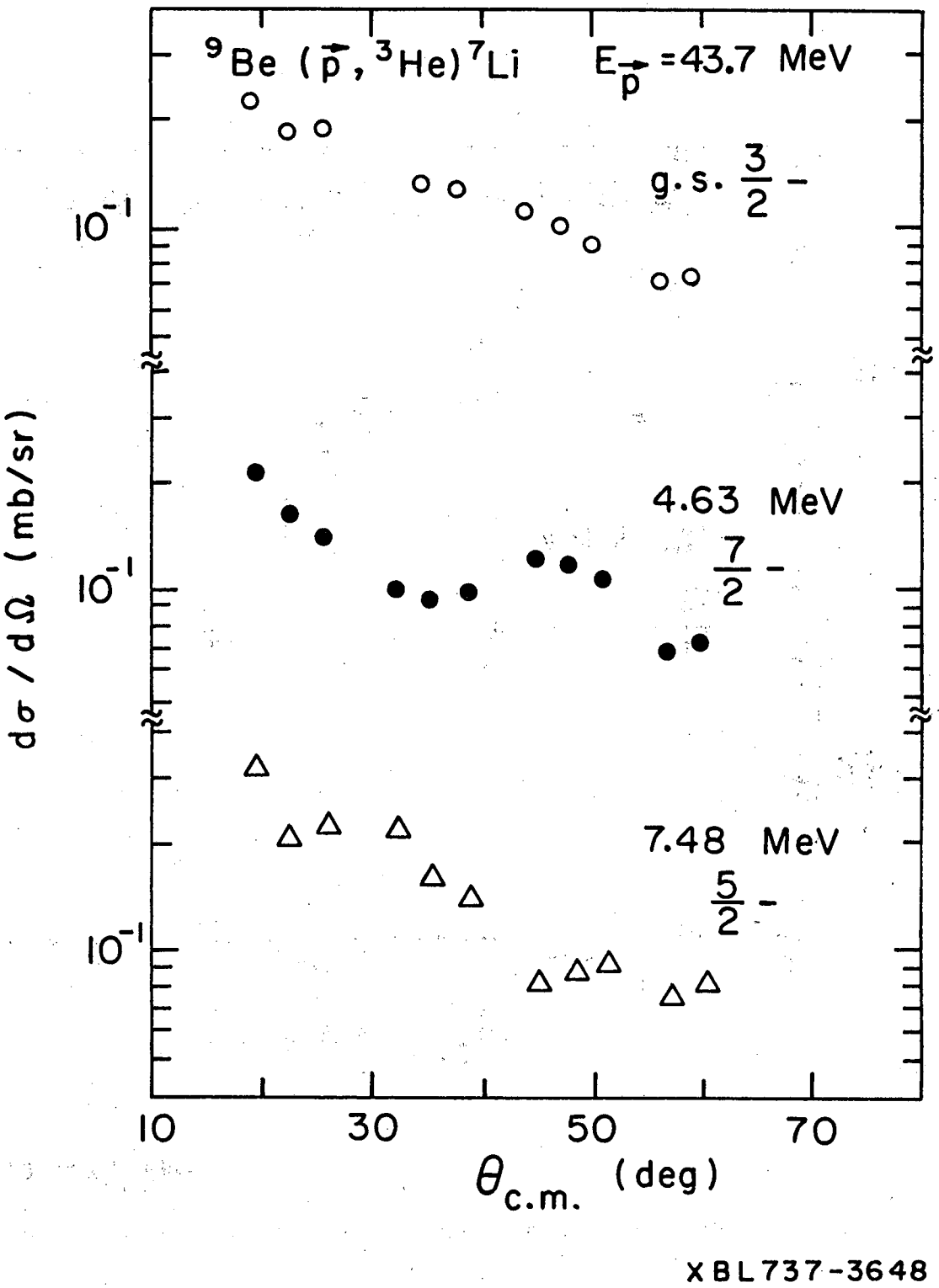


Fig. 47. Cross section data for three ($\vec{p}$, $^{3}$He) transitions to states in $^{7}$Li. See also Figs. 49 and 50.

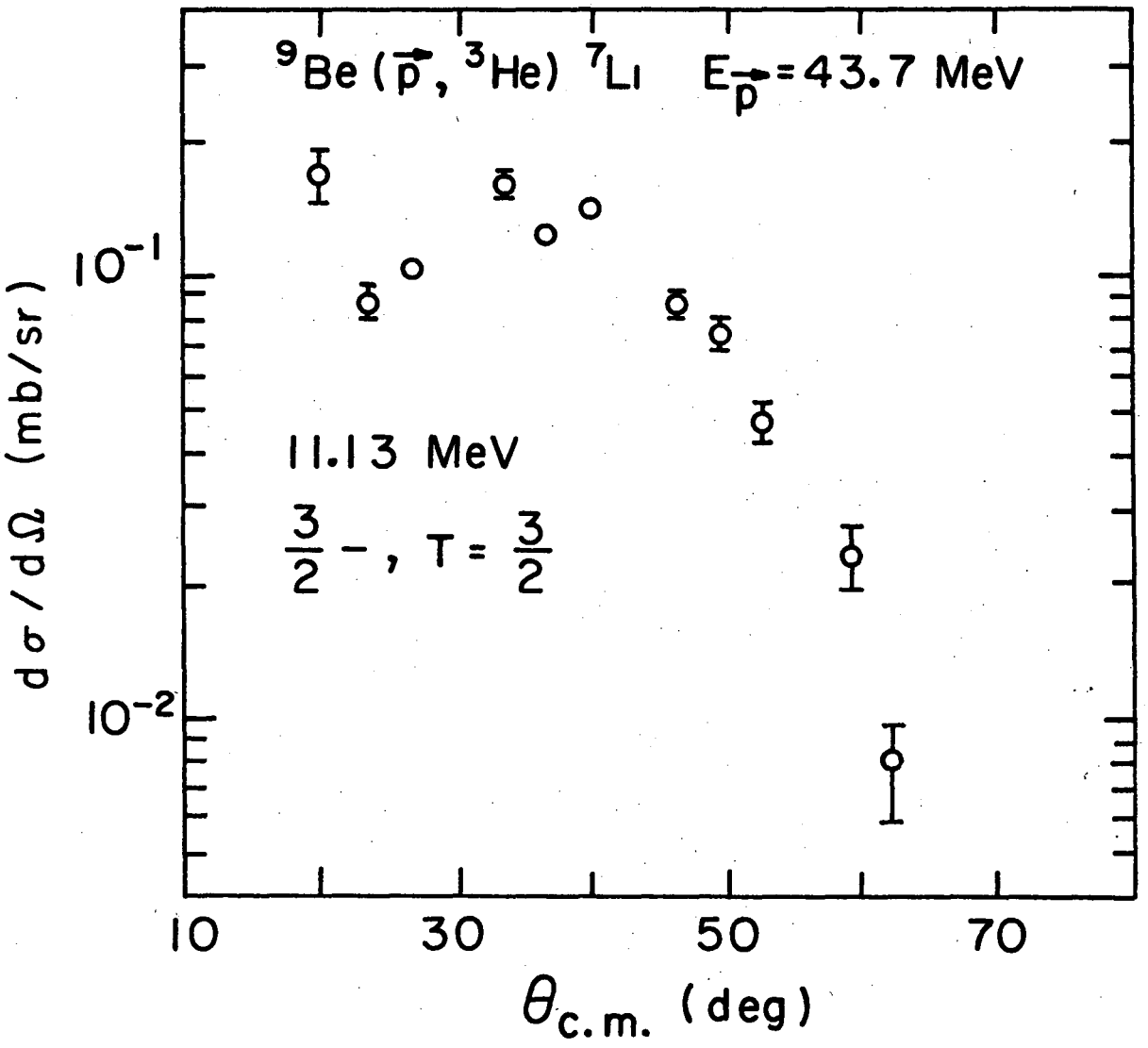


XBL737-3649

Fig. 48. Cross section data for the ($\vec{p}$, $^{3}$He) T = 3/2 analog transition to $^{7}$Li. See also Fig. 50.

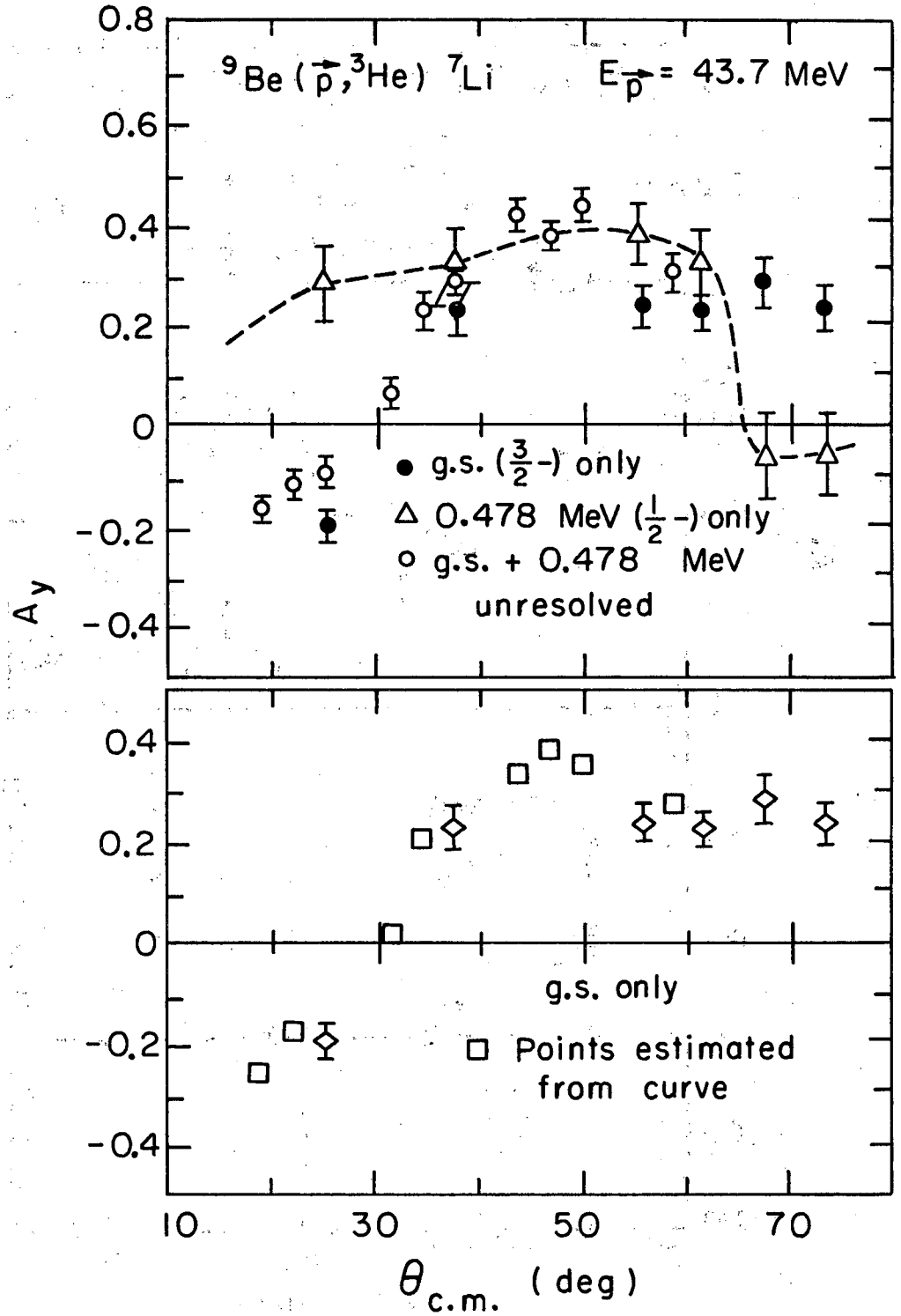


Fig. 49. Analyzing power data for the $^9$Be($\vec{p}$, $^3$He)$^7$Li ground state (shown in Fig. 47) and first excited state transitions. The data analysis is explained in the text.

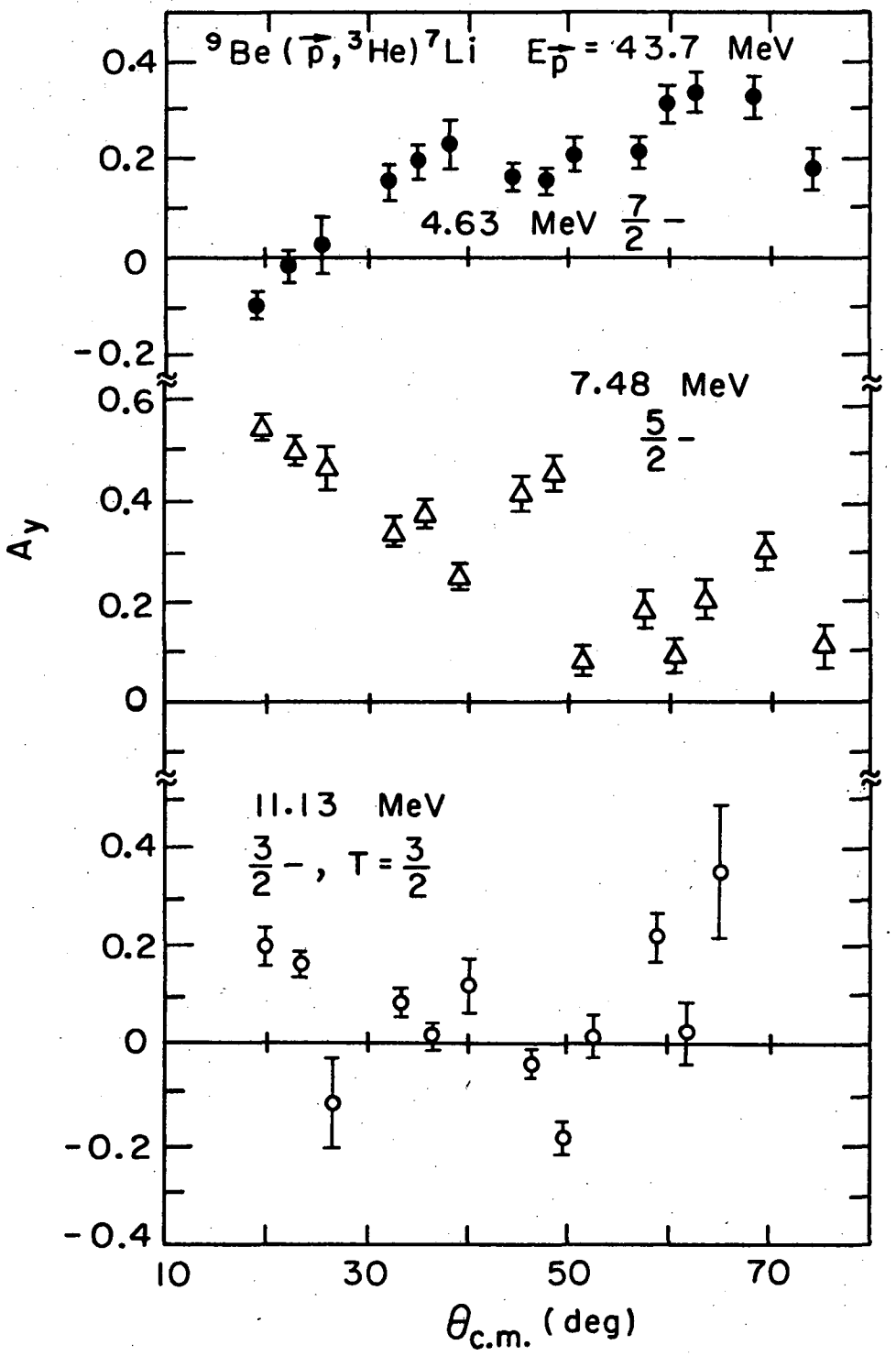


Fig. 50. Analyzing power data for three of the ($\vec{p}$, $^3$He) transitions shown in Figs. 47 and 48.

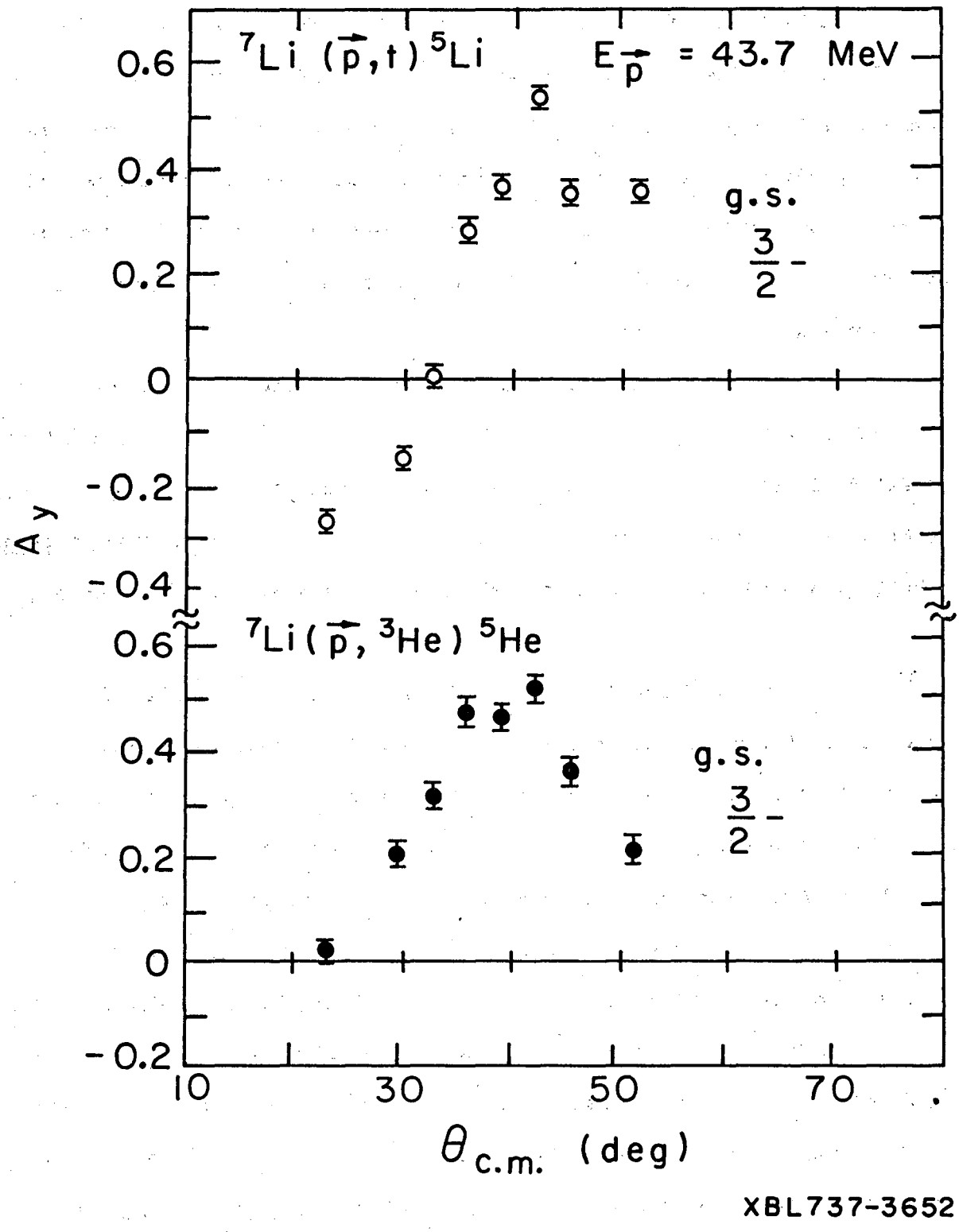


Fig. 51. Analyzing powers for the ground state transitions in $^7$Li$(\vec{p},t)^5$Li and $^7$Li$(\vec{p},\ ^3$He$)^5$He.

rough interpolation for $A_y$ of the $\sim$ 0.4 MeV first excited states, shown by the dashed line, and by also using the absolute $d\sigma/d\Omega$ obtained from the literature (Cer 66), it was possible to estimate a correction to the unresolved ground state points to remove the effect of the 0.4 MeV states (see Appendix). These estimated corrections are shown at the bottom of Figs. 45 and 49 by the squares. No error bars have been assigned since the uncertainty is dominated by the interpolated $A_y$ for the first excited state which is only an estimate.

The T = 3/2 analog transitions to mass-7 (Figs. 46 and 50) agree reasonably well in $A_y$, as well as showing the clear L = 0 characteristics (Dét 65) in the $(d\sigma/d\Omega)$ (Figs. 44 and 48). Little further physical interpretation of these data on $^9$Be seems possible without a more sophisticated theoretical approach and a more elaborate understanding of the simpler transitions discussed earlier.

Previous efforts (McG 68) have been unable to establish the existence of T = 3/2 states in $^5$Li and $^5$He. One objective of these present experiments was to see if an asymmetry could be detected in the appropriate region of continuum well above the ground state ($\gtrsim$ 16 MeV) which might indicate the presence of such a high isospin state.

In our method of measurement, the analyzing power was overdetermined permitting the use of a procedure whereby instrumental asymmetry, if any, can be eliminated as discussed in Chapter II. If it is established that the instrumental asymmetry is negligible as was the case in our experiments, the analyzing power can be evaluated from the data in either of two ways. First, the data from opposite sides of the beam axis, using only one spin orientation of the beam can be used; or, data from one detector

telescope, using both beam spin orientations can be used. To analyze the continuum for asymmetry, the data for $^{7}Li(\vec{p},t)$ and $(\vec{p}, {}^{3}He)$ were examined, using the second method, as a function of channel number or excitation energy in mass-5. In this way, two determinations of the asymmetry in the spectrum were obtained for each angle, one from each side of the beam axis. The analysis showed no asymmetry in the region of interest which was statistically inconsistent with zero, and this search for new high isospin states below $\sim$ 20 MeV excitation, therefore, yielded negative results.

## B. A Heavy Target: $^{208}Pb(\vec{p},t)^{206}Pb$

The results of part A above and those of others (Nel 70a, Nel 70b) suggest that the simple DWBA as applied in these calculations is not generally very satisfactory in accounting for the analyzing powers, in light nuclei at medium energies, even for many cases where the cross section is reasonably well predicted. The only work reported on a target heavier than $^{28}Si$ are some recent results obtained on $^{176}Yb(\vec{p},t)^{174}Yb$ at $E_{\vec{p}}$ = 16 MeV (Igo 73). In that report, the cross section and the analyzing power were rather well explained by a coupled channel Born approximation (CCBA) calculation. Because of the large target deformation, the simple DWBA is not adequate, (though results consistent with the $A_y$ data were obtained) because of the appreciable presence of two-step modes in the reaction mechanism (Asc 70). The agreement of the CCBA with the data on $^{176}Yb$ does not provide a conclusive test of the theory since the experimental points are few, with large error bars.

Our interest in a heavy target lay in examining some non-collective nucleus on which the simple DWBA has successfully described the differential cross-sections, and to see whether similar agreement can be obtained for the analyzing powers. We have therefore investigated the $^{208}Pb(\vec{p},t)^{206}Pb$ reaction at 40 MeV, for which good DWBA fits to the $d\sigma/d\Omega$ have been obtained in studies using unpolarized beams (Gle 67, Rey 67, Smi 68, Smi 70).

In Fig. 52, a representative spectrum from our data is shown in which the analyzed transitions are indicated by the $J^{\pi}$ of the final state. The differential cross sections and corresponding analyzing power results are presented in Figs. 53 and 54, respectively. The differential cross sections have been normalized as described earlier (Chapter II) and agree well with previous measurements. Some noteworthy features of the corresponding analyzing powers are the following. The $0^+$ ground state ($L = 0$) transition shows the most dramatic analyzing power behavior, extending to 0.85 at 25° c.m. For transitions with $L > 0$ the analyzing power is substantially smaller, decreasing in amplitude with increasing L, and the phases for the $0^+$, $2^+$, $4^+$, and $6^+$ transitions alternate as $(-1)^{L/2}$.

The analyzing power for the ground state transition bears a very clear approximate derivative relationship to the differential cross section, i.e. $|A_y(\theta)| \propto d/d\theta(d\sigma/d\Omega)$. Such a relationship appears to hold also for the excited states though it is less striking probably because the diffraction pattern is much less pronounced. Rodberg (Rod 59) has shown that such a relationship can be derived for elastic scattering from the properties of the optical model if a spin dependent distortion is included, such as a spin-orbit potential of the form $V_{SO}(r)\vec{\sigma}\cdot\vec{\ell}$. Others have shown

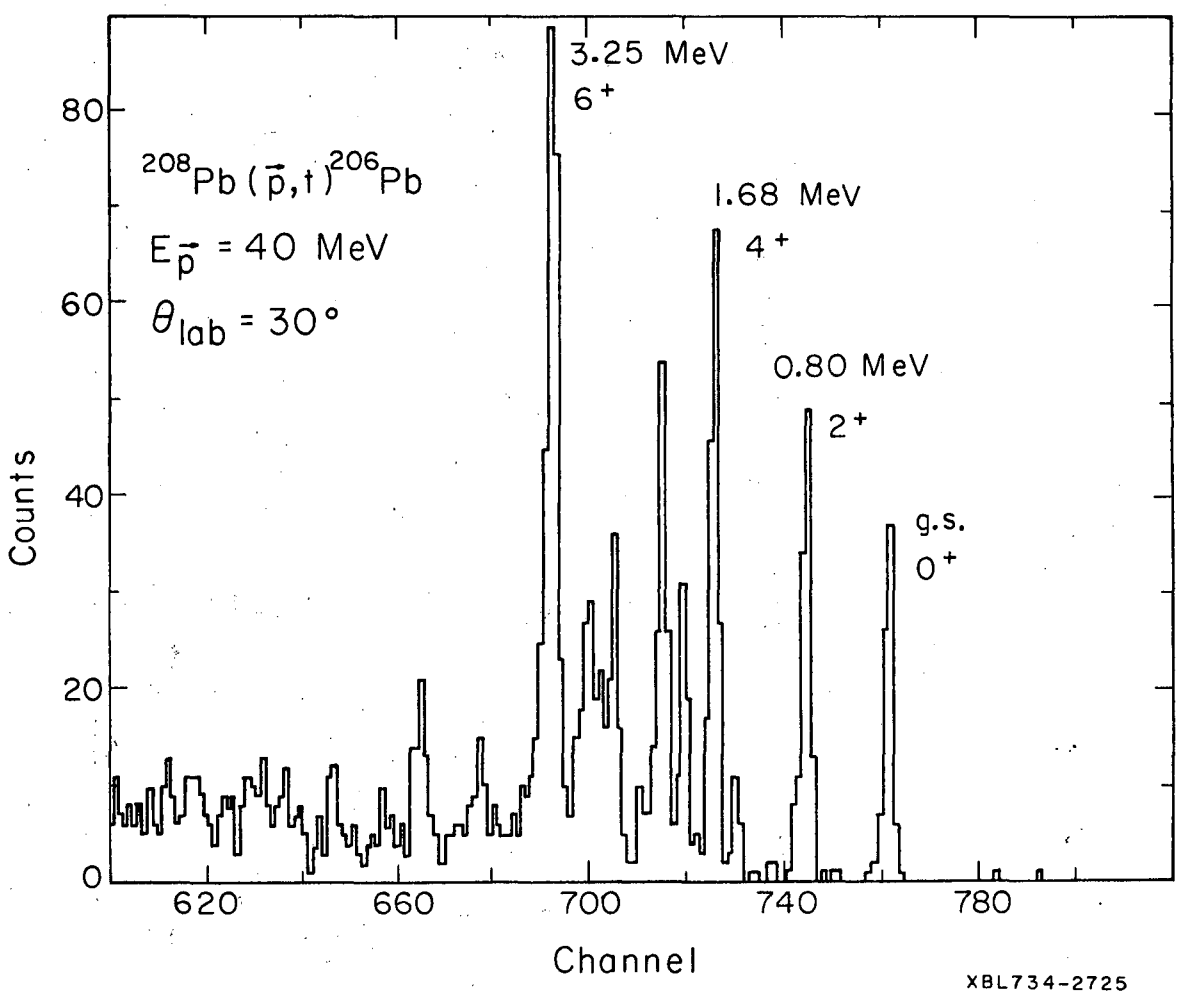


Fig. 52. Representative triton energy spectrum for $^{208}Pb(\vec{p},t)^{206}Pb$.

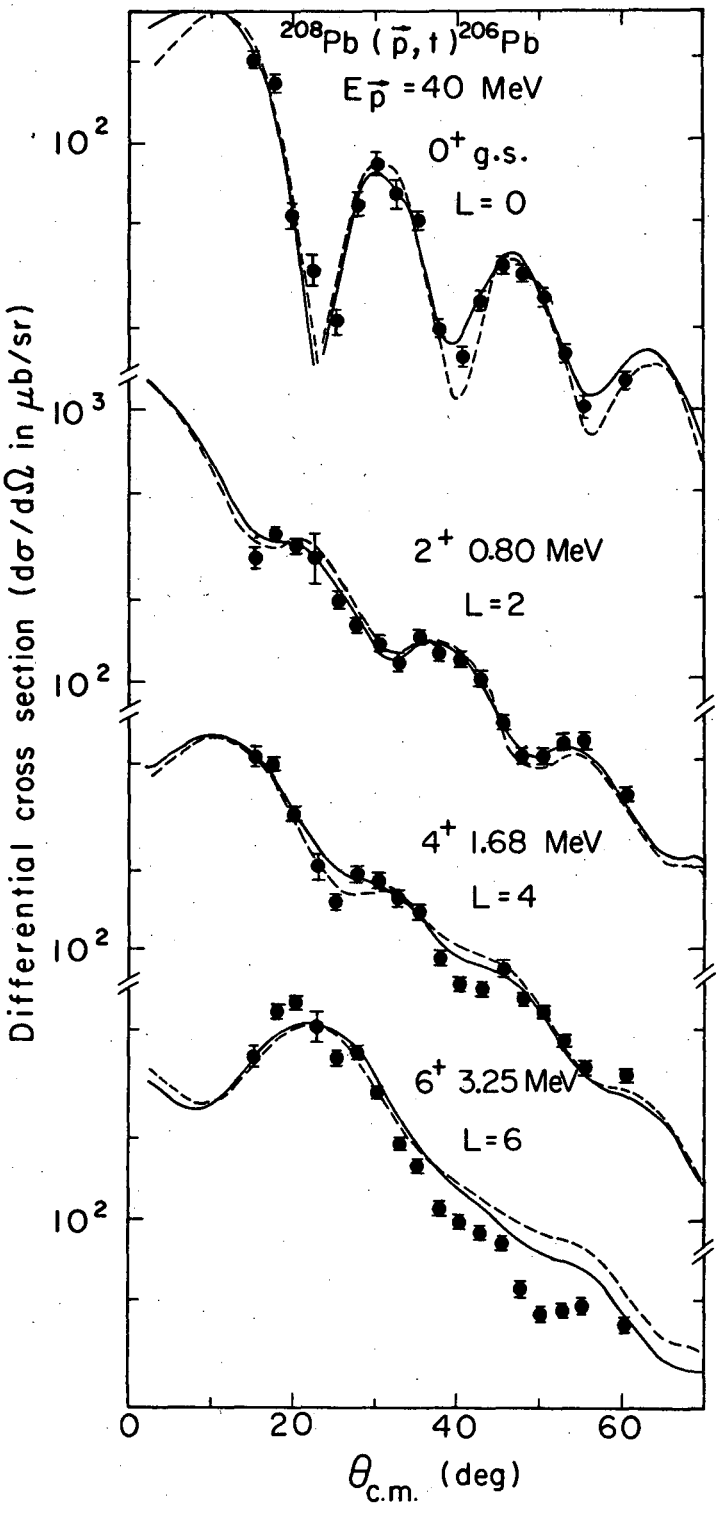


Fig. 53. Differential cross sections for transitions to states labeled in Fig. 52. The curves are separately normalized DWBA calculations obtained using two different proton optical potentials as discussed in the text. See also Fig. 54.

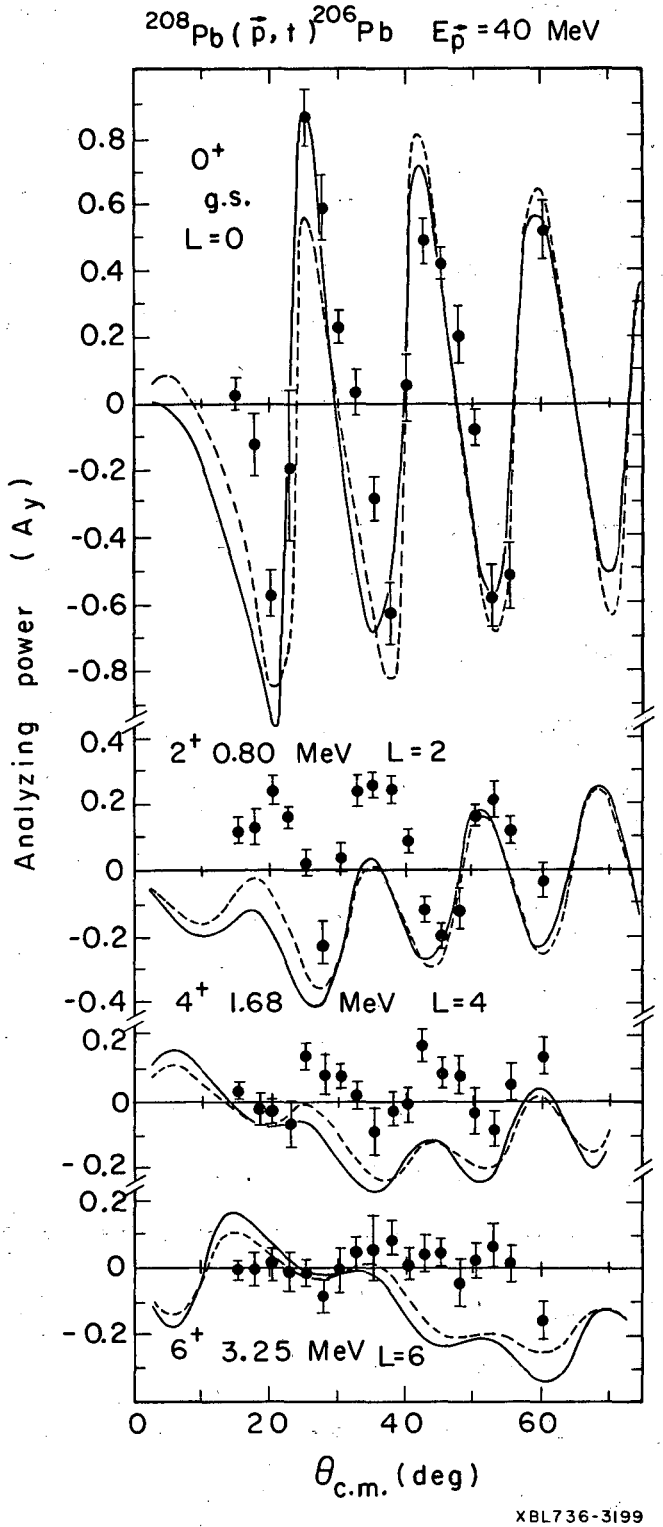


Fig. 54. Analyzing powers for the corresponding distributions of Fig. 53. The curves are DWBA fits as described in the text.

(Bie 61) that such a relationship may apply more generally than just to elastic scattering; they considered the case of single nucleon stripping. For this simple picture to hold, the strength of the spin-orbit coupling in the initial and final distorted waves must be small compared with the strength of the central well, and must be independent of $\ell$ in the summation over partial waves. It is interesting to note that this derivative relationship remains qualitatively valid for these particular $(\vec{p},t)$ transitions.

For processes such as these strong (p,t) transitions to low-lying positive parity states in $^{206}$Pb, for which the dominant shell-model configurations belong to a single oscillator shell, Glendenning (Gle 67, Gle 65) has shown that the shape (but not the magnitude) of the differential cross section angular distribution can be calculated without a detailed knowledge of the nuclear wave function. Referring to Eq. (9) in Chapter III, this means that one value of N dominates, and the sum over N vanishes. Since L,S,J are also all fixed for these (p,t) transitions, only the sums over the magnetic substates $M\mu_i\mu_f$ remain. $G_{NLSJT}$ does not depend on these so that the nuclear structure dependence is removed, except as a scaling factor which does not affect the shape of the distribution. The summations of $M\mu_i\mu_f$ generate the asymmetry in the cross section (see Eqs. (14) to (16)) giving rise to the analyzing power, and according to the simple DWBA (Bie 61), the analyzing power will depend on the shape rather than on the magnitude of the cross section. One expects, therefore, for these transitions that $A_y$ is also affected by the nuclear structure in only a minimal way.

DWBA calculations have been undertaken using structure factors from (Rey 67). With a fixed set of optical parameters the expected insensitivity of the analyzing power calculations to the wave function was confirmed for the transition to the ground state with structure amplitudes derived from several different wave functions (Rey 67, Bro 67). Having established this, the optical parameters themselves were studied. The dashed curves for the ground state transition in Figs. 53 and 54 show that parameters used in previous $^{208}$Pb(p,t) DWBA studies (see (b) and (d), Table II) produce an acceptable fit to the differential cross section, though a poorer fit to the experimental analyzing power. However, if the proton optical potential derived from the global prescription of Becchetti and Greenlees (Bec 69) is used, as shown by the solid curve, it produces a good cross section fit and also better accounts for the analyzing power, particularly in predicting the large asymmetry at 25° and the lesser maxima at more backward angles. Although a comparison of the quality of the results from the two optical potentials is inconclusive on the basis of $d\sigma/d\Omega$ alone, it appears that the latter potential is superior when the comparison is extended to include the $A_y$ predictions. Two triton potentials obtained from low energy ($\leqslant$ 20 MeV) elastic scattering (Fly 69, Bec 71) were tried, but the calculations gave fits to both $d\sigma/d\Omega$ and $A_y$ which were inferior to those shown.

In Figs. 53 and 54 calculations are also shown for the transitions to the $2^+$, $4^+$, and $6^+$ states. One can see that the fits to these differential cross sections are good for both proton optical potentials. Agreement for the analyzing powers is poor in detail, although the

predictions do oscillate in phase with the data. Calculations using the two triton potentials noted above failed, as in the ground state case, to bring any improvement to the excited state fits.

## V. SUMMARY AND CONCLUSIONS

This paper has reported angular distributions and analyzing powers measured for a large number of $(\vec{p},t)$ and $(\vec{p}, {}^3He)$ transitions between 1p-shell nuclei. Analysis of the relative differential cross section data agrees with previous results, in that angular distributions involving a unique transferred L-value, such as in many $(\vec{p},t)$ transitions, show a characteristic shape. Unfortunately the analyzing powers do not. The situation is even more complicated in $(\vec{p}, {}^3He)$ transitions which can be considerably more complex because of the greater flexibility in the transferred spin and isospin.

In order to provide theoretical perspective on these results, some of these data have been compared with zero-range DWBA calculations incorporating spin orbit terms in the optical potentials. Although these calculations generally neglected the difference in S = 0 and S = 1 transfer amplitudes which depends on the mixture of nuclear forces in the interaction, they nevertheless yielded rather good fits to nearly all the experimental differential cross sections, even those which are complex. The DWBA calculations predict that, for transitions involving a single L-transfer, the analyzing power should generally, but not always, also be characteristic of this L-value. However, the data indicate that, in fact, only in some of the particularly simple transitions, especially in the $(\vec{p},t)$ reaction, and in both reactions populating ground and T = 3/2 analog final states does the model give an acceptable account of the experimental results. In a large number of other transitions, many of which indicate no unusual complexity, the simple DWBA completely fails to predict the experimental analyzing powers. It is apparent that the

analyzing powers are sensitive to details which have only a minimal effect on the shape of the differential cross sections.

By way of contrast we have also looked at the $^{208}Pb(\vec{p},t)^{206}Pb$ reaction to four final states, obtaining rather good overall agreement between the theory and experiment. The ground state agreement is excellent for both cross sections and analyzing powers; for the excited states, the cross section fit is also of good quality and the phases and overall magnitudes of the analyzing powers are fairly well reproduced.

A determined effort has been made by a number of workers (e.g., Aus 64, Ros 71, Cha 73) to modify the DWBA formalism to eliminate the need for the zero-range approximation, and thereby to take account of finite-range effects in the interaction which are expected to be important if processes involving the nuclear interior are significant (Aus 64). Such circumstances may be more the case in the light nuclei and for transitions to excited states in the heavy nuclei. With respect to the analyzing powers, Nelson et al. (Nel 70b) have had some success in improving fits to the few cases they considered below mass-28 by including a finite range routine, but it is not obvious that the large changes needed to achieve good fits for some of the 1p-shell data presented here could be obtained in this way. However it would be very interesting to examine this approach with the more extensive experimental data now available.

There is no doubt that a major factor contributing to the difficulty of obtaining definitive information from these calculations is the choice of suitable optical potentials. For the light targets at these energies, the choice is not always obvious, especially for the mass-3 channel. In

lead, also, the availability of suitable elastic scattering data with which to establish a proper triton optical potential would remove some uncertainty in assessing, for example, the validity of the zero-range approximation. Given this lack of complete optical model information for the applicable elastic scattering processes, this source of uncertainty cannot be overcome.

By assuming a simple direct process in these calculations, the effects of multi-step or second-order processes have been neglected. The extent to which such factors affect the analyzing power in these cases is not known although efforts are underway to examine this point (Kun 73) for lead. The strength of the L-forbidden $(\vec{p},t)$ transition on the $^{13}C$ target is a good indication that the assumption of a one-step direct mechanism may be too simplistic in some circumstances.

If multiple-step processes were important, involving, for example, inelastic scattering in the proton channel, the correct treatment of the spin-orbit term in the optical potential might become a crucial element of the analysis. It has been shown (She 68, Ray 71, Sat 71) that deformation in this potential is important in the description of cross sections, analyzing powers, and spin-flip probabilities for $(\vec{p},p')$ reactions even for relatively spherical targets. In particular, the inclusion of the so-called "full Thomas" form of the potential appears to be necessary to obtain good fits to these data, and may yield strong effects in multi-step two-nucleon transfer mechanisms also.

Our results on the 1p-shell nuclei further demonstrate the inadequacy of the simple DWBA and indicate a clear need for further theoretical effort. These data may well provide a sensitive test of

new theoretical developments in the study of two nucleon transfer reactions in light nuclei. Although the present theory seems better able to account for the experimental data from the lead target, these results also may be of use in evaluating more refined calculations which consider such effects as second-order and finite-range processes.

ACKNOWLEDGMENTS

While I've been at Berkeley, many people have contributed directly or indirectly to the accomplishment of my degree work, all of whom I wish to thank. It is a pleasure to write this acknowledgment to the following, to whom I owe special thanks.

To Professor Joseph Cerny who, as my research advisor, has been a generous source of inspiration and encouragement.

To the other staff scientists Dr. B. G. Harvey, Dr. D. L. Hendrie, and Dr. H. E. Conzett for their interest and helpful discussions, and Dr. Conzett also for the use of much of his experimental equipment and for help with the polarized ion source.

To Dr. J. C. Hardy for his guidance during the early portion of this work.

To Dr. A. D. Bacher, Dr. G. R. Plattner, Dr. H. L. Harney, Dr. N. A. Jelley, Dr. R. A. Gough, Dr. D. G. Kovar, Dr. F. D. Becchetti, Dr. Y. Terrien, Mr. R. G. Sextro, Mr. K. H. Wilcox, Mr. G. J. Wozniak, Mr. R. B. Weisenmiller, Dr. J. D. Sherman, Dr. M. S. Zisman, Dr. J. E. Esterl, and Dr. G. W. Goth for help with the experiments and for numerous useful and enjoyable discussions both trivial and profound.

To Dr. C. C. Maples for help with the computers and for the use of several programs.

To the entire staff of Building 88 and the cyclotron whose professional assistance was invaluable in doing the experiments.

To Ann, who is my wife, for just that, and for typing the draft of this thesis.

I would also like to acknowledge a Postgraduate Scholarship granted by the National Research Council of Canada.

This work was performed under the auspices of the United States Atomic Energy Commission.

# APPENDIX

## RESULTANT ANALYZING POWER FROM TWO UNRESOLVED PEAKS

A simple relationship exists between the analyzing powers and cross sections of two transitions which yield unresolved peaks. The same relationship also applies to complex transitions of multiple J transfers as occur in $(\vec{p}, {}^3He)$, if the cross section and analyzing power for each J is calculated separately.

For an unpolarized beam, the cross section $\sigma_o(\theta)$ is independent of $\phi$ so that

$$\sigma_o(\theta) = \sigma_o(-\theta) \quad .$$

Also for a polarized beam

$$\sigma_{pol}(\theta) = \sigma_o(\theta)\ [1 + \vec{P}_{beam} \cdot \vec{A}(\theta)]$$

$$= \sigma_o(\theta)\ [1 - e] \text{ where } e = \vec{P} \cdot \vec{A}(\theta) \text{ is the asymmetry.}$$

Then

$$\sigma(-\theta) = \sigma_o(-\theta)\ [1 + e]$$

$$= \sigma_o(\theta)\ [1 + e] \quad .$$

The number of counts in the left and right detectors for a given peak are:

$$\#\text{ counts left} \equiv N_L = \Omega_L \sigma(-\theta)$$

$$\#\text{ counts right} \equiv N_R = \Omega_R \sigma(\theta)$$

Therefore, the analyzing power is

$$A = \frac{1}{P_{beam}} \left( \frac{\Omega_L \sigma(-\theta) - \Omega_R \sigma(\theta)}{\Omega_L \sigma(-\theta) + \Omega_R \sigma(\theta)} \right) ,$$

or, if $\Omega_L = \Omega_R$ ,

$$A \equiv \frac{1}{P_{beam}} \left( \frac{\sigma(-\theta) - \sigma(\theta)}{\sigma(-\theta) + \sigma(\theta)} \right) .$$

Now, for two components, 1 and 2,

$$\sigma(-\theta) = \sigma_1(-\theta) + \sigma_2(-\theta)$$

$$\sigma(\theta) = \sigma_1(\theta) + \sigma_2(\theta) ,$$

and

$$\sigma_1(\theta) = \sigma_{01}(\theta) \left[ 1 + P_{beam} \cdot \vec{A}_1(\theta) \right] , \text{ etc.}$$

Therefore,

$$A = \frac{1}{P_{beam}} \left\{ \frac{\sigma_1(-\theta) + \sigma_2(-\theta) - \sigma_1(\theta) - \sigma_2(\theta)}{\sigma_1(-\theta) + \sigma_2(-\theta) + \sigma_1(\theta) + \sigma_2(\theta)} \right\}$$

$$= \frac{1}{P_{beam}} \left\{ \frac{\sigma_{01}(\theta)(1 + e_1) + \sigma_{02}(1 + e_2) - \sigma_{01}(1 - e_1) - \sigma_{02}(1 - e_2)}{\sigma_{01}(\theta)(1 + e_1) + \sigma_{02}(1 + e_2) + \sigma_{01}(1 - e_1) + \sigma_{02}(1 - e_2)} \right\}$$

$$= \frac{1}{P_{beam}} \left\{ \frac{\sigma_{01} e_1 + \sigma_{02} e_2}{\sigma_{01} + \sigma_{02}} \right\} ,$$

but $e_i = \vec{P}_{beam} \cdot \vec{A}_i$. Therefore,

$$A = \frac{\sigma_{01} A_1 + \sigma_{02} A_2}{\sigma_{01} + \sigma_{02}} .$$

In simple terms the resultant analyzing power is just the expected result: the average of the analyzing powers of the two components, weighted by their respective cross sections.

## FOOTNOTES AND REFERENCES

[1]See reference Hae 67. In short, the field of a sextupole is given by $B = B_m(\frac{r}{r_m})^2$ where B and r are the magnetic field and the radial distance from the axis, respectively. Subscript m denotes the value at the pole tip. The radial force then is

$$F \equiv -\text{grad}\ (\mu \cdot B), \text{ where } \mu \equiv \text{magnetic moment}$$

$$= -\mu\ \text{grad}\ B$$

$$= -2\mu \frac{B_m}{r_m^2} r$$

i.e. $F \propto r$.

[2]Our nomenclature and definitions follow the Madison Convention (Bar 71, p. xxv).

[3]DWUCK was written by P. D. Kunz, University of Colorado, Boulder, Colorado, (Oct. 1967 version). Modifications to include the harmonic oscillator two-nucleon form factor were made by J. C. Hardy. Other changes to include the coherent and incoherent summations for multiple transfers were made by J. C. Hardy, H. L. Harney and myself.

[4]Structure amplitudes corresponding to a pure jj-configuration were taken from reference (Fle 71).

Ajz 68 F. Ajzenberg-Selove and T. Lauritsen, Nucl. Phys. A114, 1 (1968).

Ajz 70 F. Ajzenberg-Selove, Nucl. Phys. A152, 1 (1970).

Asc 70 R. J. Ascuitto and N. K. Glendenning, Phys. Rev. C2, 1260 (1970).

Aus 64 N. Austern, R. M. Drisko, E. C. Halbert, and G. R. Satchler, Phys. Rev. 133, B3 (1964).

Bac 72 A. D. Bacher, G. R. Plattner, H. E. Conzett, D. J. Clark, H. Grunder, and W. F. Tivol, Phys. Rev. C5, 1147 (1972).

Bar 67 H. H. Barschall, Am. J. Phys. 35, 119 (1967).

Bar 71 Polarization Phenomena in Nuclear Reactions, Proc. Third Int'l. Symposium, Madison 1970, ed. H. H. Barschall and W. Haeberli, (University of Wisconsin, Madison, 1971).

Bec 69 F. D. Becchetti, Jr., and G. W. Greenlees, Phys. Rev. 182, 1190 (1969).

Bec 71 F. D. Becchetti, Jr., and G. W. Greenlees, p. 682 in (Bar 71).

Bie 61 L. C. Biedenharn and G. R. Satchler, Helv. Phys. Acta, Suppl. 6, 372 (1961).

Bro 67 R. A. Broglia and C. Riedel, Nucl. Phys. A92, 145 (1967).

Cer 64a J. Cerny and R. H. Pehl, Phys. Rev. Letters 12, 619 (1964).

Cer 64b J. Cerny and R. H. Pehl, Symposium on Nucl. Spectroscopy with Direct Reactions, Argonne Nat'l. Lab. Report ANL-6848 (1964), p. 208.

Cer 66 J. Cerny, C. Détraz, and R. H. Pehl, Phys. Rev. 152, 950 (1966).

Cha 73 L. A. Charlton, Phys. Rev. C8, 146 (1973).

Cla 69 D. J. Clark, A. U. Luccio, F. Resmini, and H. Meiner, Fifth Int'l. Cyclotron Conf., Oxford, England, ed. R. W. McIlroy, (Butterworth and Co. Ltd., London 1971), p. 610.

Coh 65 S. Cohen and D. Kurath, Nucl. Phys. 73, 1 (1965).

Coh 70 S. Cohen and D. Kurath, Nucl. Phys. A141, 145 (1970).

Con 66 H. E. Conzett and B. G. Harvey, Nucleonics 24, 48 (1966).

Cos 68 S. W. Cosper, R. L. McGrath, J. Cerny, C. C. Maples, G. W. Goth, and D. G. Fleming, Phys. Rev. 176, 1113 (1968).

Dav 66 A. S. Davydov, Quantum Mechanics, (NEO Press, Ann Arbor, 1966) translated by I. V. Schensted from the original Russian (Gov't Publishing House for Physical and Mathematical Literature (Fizmatigiz), Moscow, 1963).

Dét 65 C. Détraz, J. Cerny, and R. H. Pehl, Phys. Rev. Letters 14, 708 (1965).

Fes 58 H. Feshbach, Ann. Rev. Nucl. Sci. 8, 49 (1958).

Fle 67 D. G. Fleming, Ph.D. Thesis, University of California, Berkeley, 1967 (unpublished).

Fle 68a D. G. Fleming, J. Cerny, and N. K. Glendenning, Phys. Rev. 165, 1153 (1968).

Fle 68b D. G. Fleming, J. Cerny, C. C. Maples, and N. K. Glendenning, Phys. Rev. 166, 1012 (1968).

Fle 71 D. G. Fleming, J. C. Hardy, and J. Cerny, Nucl. Phys. A162, 2255 (1971).

Fly 69 E. R. Flynn, D. D. Armstrong, J. G. Beery, and A. G. Blair, Phys. Rev. 182, 1113 (1969).

Fri 67 M. P. Fricke, E. E. Gross, B. M. Morton, and A. Zucker, Phys. Rev. 156, 1207 (1967).

Gla 69 C. Glashausser and J. Thirion, Adv. Nucl. Phys. 2, 79 (1969).

Gla 74 C. Glashausser, in Nuclear Spectroscopy and Reactions, ed. by J. Cerny (Academic Press, New York, in press).

Gle 63 N. K. Glendenning, Ann. Rev. Nucl. Sci. 13, 191 (1963).

Gle 65 N. K. Glendenning, Phys. Rev. 137, B102 (1965).

Gle 67 N. K. Glendenning, Phys. Rev. 156, 1344 (1967).

Gle 68 N. K. Glendenning, University of California Lawrence Berkeley Laboratory Reports UCRL-18268 and UCRL-18269 (unpublished).

Gle 73 N. K. Glendenning, private communication. The dependence of the structure factor on the oscillator parameter is contained entirely in the overlap, denoted by $\Omega_n$, of the center-of-mass motion of the transferred pair in the target and in the exit mass-3 particle. See Gle 65.

Gol 60 L. J. B. Goldfarb and R. C. Johnson, Nucl. Phys. 18, 353 (1960).

Gou 64 F. S. Goulding, D. A. Landis, J. Cerny, R. H. Pehl, Nucl. Instr. Methods 31, 1 (1964).

Gou 65 F. S. Goulding, Semiconductor Detectors for Nuclear Spectroscopy, University of California Lawrence Berkeley Laboratory Report UCRL-16231, 1965 (unpublished).

Hae 67 W. Haeberli, Ann. Rev. Nucl. Sci. 17, 373 (1967).

Hae 71 W. Haeberli, in Bar 71, p. 235.

Hae 74 W. Haeberli, in Nuclear Spectroscopy and Reactions, ed. by J. Cerny, (Academic Press, New York, in press).

Har 70a J. C. Hardy, H. Brunnader, and J. Cerny, Phys. Rev. C1, 651 (1970).

Har 70b J. C. Hardy, A. D. Bacher, G. R. Plattner, J. A. Macdonald, and R. G. Sextro, Phys. Rev. Letters 25, 298 (1970).

Hod 71 P. E. Hodgson, Nuclear Reactions and Nuclear Structure, (Oxford University Press, London, 1971).

Igo 73 G. Igo, J. C. S. Chai, R. F. Casten, T. Udagawa, and T. Tamura, Nucl. Phys. A207, 289 (1973).

Kah 71 S. Kahana and D. Kurath, Phys. Rev. C3, 543 (1971).

Kun 73 P. D. Kunz, private communication.

Lau 66 T. Lauritsen and F. Ajzenberg-Selove, Nucl. Phys. 78, 1 (1966).

Luc 69 A. U. Luccio, D. J. Clark, D. Elo, P. Frazier, H. Meiner, D. Morris, and M. Renkas, University of California Lawrence Berkeley Laboratory Report UCRL-18607 (1969).

McE 70 W. S. McEver, T. B. Clegg, J. M. Joyce, and E. J. Ludwig, Phys. Rev. Letters 24, 1123 (1970).

McG 68 R. L. McGrath, J. Cerny, and S. W. Cosper, Phys. Rev. 165, 1126 (1968).

Nel 70a J. M. Nelson, N. S. Chant, and P. S. Fisher, Phys. Letters 31B, 445 (1970).

Nel 70b J. M. Nelson, N. S. Chant, and P. S. Fisher, Nucl. Phys. A156, 406 (1970).

Pla 68 G. R. Plattner, T. B. Clegg, L. G. Keller, Nucl. Phys. A111, 481 (1968).

Per 72 C. M. Perey and F. G. Perey, Nucl. Data Tables 10, 539 (1972).

Ray 71 J. Raynal, Centre d'Etudes Nucleaires de Saclay Report D. Ph/t No71/1 (1971), (unpublished).

Rey 67 G. M. Reynolds, J. R. Maxwell, and N. M. Hintz, Phys. Rev. 153, 1283 (1967).

Rod 59 L. S. Rodberg, Nucl. Phys. 15, 72 (1959).

Rom 65 P. Roman, Advanced Quantum Theory, (Addison-Wesley Co., Inc., Reading, 1965).

Ros 67 L. Rosen, Science 157, 1127 (1967).

Ros 71 E. Rost and P. D. Kunz, Nucl. Phys. A162, 376 (1971).

Sat 64 G. R. Satchler, Nucl. Phys. 55, 1 (1964).

Sat 71 G. R. Satchler, in Bar 71, p. 155.

She 68 H. Sherif and J. S. Blair, Phys. Letters 26B, 489 (1968).

Smi 68 S. M. Smith, C. Moazed, A. M. Bernstein, and P. G. Roos, Phys. Rev. 169, 951 (1968).

Smi 70 S. M. Smith, P. S. Roos, A. M. Bernstein, and C. Moazed, Nucl. Phys. A158, 497 (1970).

Tob 61 W. Tobocman, Theory of Direct Nuclear Reactions, (Oxford University Press, Oxford, 1961).

Tow 69 I. S. Towner and J. C. Hardy, Advan. Phys. 18, 401 (1969).

Tru 58 W. W. True and K. W. Ford, Phys. Rev. 109, 1675 (1958).

Tru 63 W. W. True, Phys. Rev. 130, 1530 (1963).

Wol 56 L. Wolfenstein, Ann. Rev. Nucl. Sci. 6, 43 (1956).

*TECHNICAL INFORMATION DIVISION*
*LAWRENCE BERKELEY LABORATORY*
*UNIVERSITY OF CALIFORNIA*
*BERKELEY, CALIFORNIA 94720*